Structures and Mechanisms in Elastoinertial Turbulence

By

Ashwin Shekar

A dissertation submitted in partial fulfillment of the

requirements for the degree of

Doctor of Philosophy

(Chemical Engineering)

at the

UNIVERSITY OF WISCONSIN – MADISON

2021

Date of final oral examination: March 15, 2021

The dissertation is approved by the following members of the Final Oral Committee:

Michael D. Graham, Professor, Chemical Engineering

Daniel J. Klingenberg, Professor, Chemical Engineering

Reid C. Van Lehn, Assistant Professor, Chemical Engineering

Jean-Luc Thiffeault, Professor, Mathematics

To my family

For all their love and support

Acknowledgments

I would like to express my deepest gratitude towards Prof. Michael D. Graham for giving me the opportunity to be a part of this invaluable learning experience. His guidance over the years has helped me grow, not just as a researcher, but as a person too . I look forward to our continued interactions.

I would also like to thank the rest of my thesis committee: Prof. Klingenberg, for teaching me graduate transport phenomena which has helped me in my research; Prof. Van Lehn, who also served on my 4th-year talk committee and for being so approachable; and Prof. Thiffeault, who taught one of my favorite courses in grad school. I am grateful to all committee members for helping me schedule my defense. Their insightful comments and questions help me look at my research from a broader context.

My research on elastoinertial turbulence was done in collaboration with Prof. Beverley McKeon and Ryan McMullen. Their critical insights from linear analyses have been invaluable. I have learnt a lot from our interactions which has opened my eyes to new ways of thinking. I am thankful to Ryan for always being approachable and a joy to collaborate with.

The Graham group has been a nurturing environment to constantly learn and

grow. I am grateful to Sung-Ning Wang (Sandy), Anubhav Kushwaha, Rafael Henríquez Rivera, Sarit Dutta and Jae Sung Park for being amazing mentors as I began my research. Over the years, I have enjoyed countless thought-provoking conversations with Xiao Zhang, Frank Nguyen, Alec Linot, Daniel Floryan, Kevin Zeng, RJ Hommel, Eric Yu and Carlos Perez among others. I look forward to staying in touch.

I have made some amazing friends over the years that has made Madison, Wisconsin feel like a second home. I am grateful to Prashant Kumar who has been like a brother to me. I will miss our afternoon coffee breaks and engaging discussions about life. I could not have gone through grad school without the pick-up football sessions, through which I have made some close friendships - Mario Rosales, Daniel Clark, Eduardo Moura, Barin Dedeleroglu, Brendon Konon and Joshua Martens among others. Special mentions to Sophia Jain, Mario, Dan and Edu for our close companionship over the years. I owe thanks to many other friends, including Aashrith Saraswathibhatla, Raunak Bardia, Saurabh Bhandari, Ranjeet Kumar, Apoorva Sampat and Sandy Chen for going through the PhD journey together.

Last but not the least, I would like to thank my parents, Shekar and Uma, for their constant love and support, without which, none of this would have been possible. My brother, Ajay, for always looking out for me - you are truly the best brother I could ask for.

Abstract

Energy dissipation due to wall-bounded turbulence accounts for nearly 25% of the energy used in the transportation of fluids. Adding small amounts of long chain polymer molecules can have tremendous mitigating effects on turbulence and has become standard practice in the industry. Despite its wide range of applications, a complete fundamental understanding of this technology remains an outstanding problem. Perhaps the most intriguing aspect is the existence of an upper limit of drag reduction termed the Maximum Drag Reduction (MDR) asymptote. The existence of such a state has puzzled scientists for over five decades until recent advances in experimental and computational techniques that have helped unearth clues to answer this mystery. Recent studies at MDR have identified a very different regime of turbulence getting excited with viscoelasticity, dubbed elastoinertial turbulence (EIT). In the present work, we use direct numerical simulations (DNS) of dilute polymer solutions modeled using the FENE-P model, to gain a deeper understanding of mechanisms underlying EIT. Close to its inception, we show that EIT at low Reynolds number displays localized polymer stretch fluctuations. These are very similar to structures arising from linear analyses (Tollmien-Schlichting (TS) modes), i.e., critical layer structures localized where the mean fluid velocity equals the wave speed. To build on this evi-

dence connecting TS mechanisms and EIT, we then detail the existence of a family of attractors whose structure closely resembles the linear TS mode, and nonlinearly self-sustained by viscoelasticity. The existence of such a state indicates the presence of a nonlinear mechanism for TS structure. Finally, we show how this attractor is connected to EIT and uncover the underlying process responsible for generating the structures seen at EIT. We then test the robustness of these observations into different parameter regimes where we continue to observe TS-like structures underlying the dynamics of EIT. These results suggest that, in the parameter range considered here, the transition leading to EIT is mediated by nonlinear amplification and self-sustenance of perturbations that excite the TS mode.

Contents

List of Figures

Chapter 1

Summary

The addition of minute quantities of long chain polymer molecules has tremendous effects on wall-bounded turbulence. The most dramatic and well known effect being the reduction of friction factor by levels unmatched by additive-free turbulence control-schemes. The rheological drag reduction phenomena was first discovered by Toms in the 1940's and is commonly referred to as "Toms effect" [Toms, 1949, 1977]. Since then, this capability has found its use in various applications that seek energy efficiency - transportation of oil, fracking and district heating & cooling systems to name a few [Fink, 2015, King *et al.*, 2012].

Despite its widespread applications, a complete fundamental understanding of polymer drag reduction remains an outstanding challenge - one that has motivated decades of research. Perhaps the biggest mystery on the forefront of researchers minds is the upper limit on the degree of drag reduction - a common theme across additive drag reduction technologies. One would naively expect a complete eradication of turbulence by continuously adding polymers and thereby achieve complete

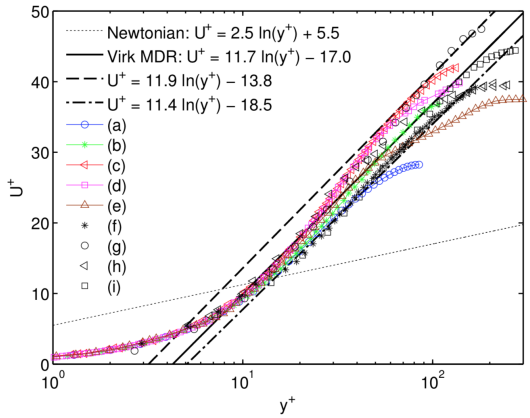

Figure 1.1: Mean velocity profiles at MDR. The curves with connected symbols correspond to computational studies ((a) - (e)); the curves with disconnected symbols are from experiments ((f) - (i)). (a) Channel, $Re_\tau = 85$ [Wang *et al.*, 2014b]. (b) Channel, $Re_\tau = 131$ [Dallas *et al.*, 2010]. (c) Channel, $Re_\tau = 100$ [Li *et al.*, 2006a]. (d) Channel, $Re_\tau = 120$ [Dubief *et al.*, 2005]. (e) Boundary layer, $Re_\tau = 425$ [Tamano *et al.*, 2011]. (f) Boundary layer, $Re_\tau = 179$ [Hou *et al.*, 2008]. (g) Pipe, $Re_\tau = 182$ [Ptasinski *et al.*, 2001]. (h) Rectangular duct, $Re_\tau = 253$ [Escudier *et al.*, 2009]. (i) Channel, $Re_\tau = 282$ [Warholic *et al.*, 1999]. Reproduced with permission from Graham [2014].

relaminarization. Fundamental answers to this mystery can potentially unlock flow control schemes that achieve this holy grail of complete relaminarization and also motivate the design of additive-free control schemes that imitate the effects of polymer molecules.

This upper limit on polymer drag reduction was first characterized by P.S. Virk in 1970 [Virk *et al.*, 1970]. By comparing results across various experimental studies, he observed a collapse of the friction factor to a near-universal scaling independent of the polymer concentration, molecular weight and species. This puzzling ultimate state was termed the Maximum Drag Reduction (MDR) asymptote and its existence has been an open question ever since.

Shown in figure 1.1 are the mean velocity profiles across various experimental and computational studies of MDR, encompassing different polymer solutions flowing through different geometries. All profiles nearly collapse on top of each other and show good agreement with the Virk log-law profile (black-solid) empirically obtained by

fitting experimental data in Virk *et al.* [1970]. However, the profiles are more strictly bounded within the 95% confidence interval about the Virk profile (black-dashed) and gives us a sense of this near-universality.

Most of the effects of polymer molecules are seen in the near-wall buffer region of wall bounded Newtonian turbulence [Graham, 2014]. This is the region close to the wall in a turbulent flow where a major fraction of the turbulence production and energy dissipation occurs [Jiménez, 2013]. Experiments and direct numerical simulations (DNS) have revealed the presence of "coherent structures" that continuously draw and dissipate energy from the mean flow [Jiménez, 2018]. Some important examples of coherent structures include quasistreamwise and hairpin vortices. From a context of flow control, understanding how these coherent structures self-sustain is an important topic still under investigation.

Important insights into the turbulent structure, especially near solid surfaces or at low Reynolds number, have been gained in recent years by looking at turbulence through the lens of nonlinear dynamical systems theory, which relates observed dynamics to underlying state space structure. In all of the canonical wall-bounded shear flow geometries (pipe flow, channel flow, plane shear (Couette) flow), families of nonlinear traveling wave solutions to the Navier-Stokes equations (NSE) that govern fluid motion have been discovered [Waleffe, 1998, 2001, 2003, Hof *et al.*, 2004, Eckhardt *et al.*, 2007, 2008, Wedin and Kerswell, 2004]. These solutions are often denoted "exact coherent states" (ECS).

In chapter 4, we describe nonlinear traveling wave solutions to the Navier–Stokes equations in the channel flow geometry – exact coherent states (ECS) – that display a hairpin-like vortex structure. The role of hairpin vortices in turbulent flows has

been an important topic in the study of turbulent structure.

Various experimental and computational investigations have focussed on the effect of viscoelasticity on this near-wall structure to try and elucidate mechanisms underlying MDR. We highlight results by Ptasinski and co-workers [Ptasinski *et al.*, 2001, 2003] to briefly go over some key features of polymer drag reduced turbulent flows.

On varying the polymer concentration, Ptasinski *et al.* [2001] experimentally observe an initial increase in the root mean square (rms) streamwise velocity fluctuations followed by a decrease on approaching MDR. The other fluctuating velocity components displayed a monotonic decrease with increasing concentration - a clear indication of weakening near-wall turbulent structures. The peak of the streamwise velocity fluctuation also moved away from the wall indicating a thickening of the buffer layer. Later on, Stone *et al.* [2002, 2004], Li and Graham [2007] captured many of these features by studying the effect of viscoelasticity on a family exact coherent states (ECS) that displayed a quasistreamwise vortex structure.

On reaching MDR, Ptasinski *et al.* [2001] observe a drastic reduction in the Reynolds shear stress - a key indicator of Newtonian turbulence production. In a follow up paper [Ptasinski *et al.*, 2003], the authors computationally corroborated their experimental findings. With access to the velocity and polymer stress fields, they also observed an increased role for polymer molecules at MDR with the polymer stress making up a significant fraction of the total stress budget. This was in agreement with Dubief *et al.* [2005] who showed that polymers inject energy in the near wall region to sustain turbulence at MDR. Taken together, these observations point at new self-sustaining mechanisms coming into play at MDR - one driven by polymer molecules rather than the near-wall vortices that drive Newtonian turbulence.

More recent experiments and simulations [Samanta *et al.*, 2013, Dubief *et al.*, 2013, Sid *et al.*, 2018] suggest that turbulence at MDR has structure very different from Newtonian, denoting it as elastoinertial turbulence (EIT). Remarkably, EIT was shown to obey a friction factor scaling that approached the MDR scaling and negligible Reynolds shear stress - a common trait of past MDR studies [Warholic *et al.*, 1999, Ptasinski *et al.*, 2001]. This pointed to the possibility that MDR was a characteristic of EIT rather than a modified version of Newtonian turbulence.

These observations draw a clear link between MDR and EIT in the parameter regimes under consideration. This has ignited a new thrust in the field to uncover the underlying mechanisms sustaining EIT - a direction that can potentially unearth new insights into polymer-flow interactions that underpin the mystery of MDR.

Building on ideas from chapter 4, in chapter 5 we report computations and analysis that unearth a prominent coherent motion in EIT and thereby elucidate mechanisms underlying EIT. We show that EIT at low Reynolds number (Re) has highly localized polymer stress fluctuations. Surprisingly, these strongly resemble the linear Tollmien-Schlichting (TS) mode which was the slowest decaying mode from linear stability analysis. The TS mode plays a very limited role in Newtonian turbulence but becomes highly amplified in the presence of viscoelasticity. This strong amplification implies that even very weak disturbances may be sufficient to trigger the nonlinear effects necessary to sustain EIT.

Inspired by the success of dynamical systems theory in the context of Newtonian turbulence, we turn to self-sustained nonlinear TS attractors and their connections to EIT in chapter 6. We identify two disconnected branches of attractors based on the TS mode - one with Newtonian origins and a second branch nonlinearly self-sustained

by viscoelasticity. We find evidence that this viscoelastic TS branch is connected to EIT, therefore suggesting a role for TS mechanisms at EIT.

In chapter 7, we describe the evolution of this viscoelastic TS branch in parameter space and expand on its connections to the Newtonian TS attractor and EIT. We detail how viscoelasticity attenuates this attractor and excites a new process responsible for generating multilayered sheets of polymer stretch - a hallmark of EIT. This process gets more pronounced with viscoelasticity before eventually giving rise to EIT.

The dissertation is organized as follows. In chapter 2, we cover the main experimental observations of transition to turbulence in dilute polymer solutions which motivate our computational investigations. The model and numerical methods for direct numerical simulations (DNS) are provided in chapter 3. Chapter 4 details our findings of a hairpin-like ECS in Newtonian channel flow and give a sense of the coherent structures in Newtonian turbulence. In chapter 5, we describe the evolution of structures and statistics at low Re - from Newtonian turbulence to EIT with a focus on uncovering mechanisms underlying EIT. We build on this understanding in chapters 6 and 7 and sketch the underlying dynamical scenario. In chapter 8, we describe the structure of EIT in other parameter regimes - very low Re and small box size - tying back to the understanding established in previous chapters. Finally, concluding remarks and avenues for future work are provided in chapter 9.

Chapter 2

Background

The first observations of polymers driving instabilities in dilute polymeric solutions were made in the 70's by Forame *et al.* [1972], Zakin *et al.* [1977]. For fixed polymer solutions and increasing Reynolds number, Re (dimensionless flow rate), both pipe flow experiments observed deviations of the friction factor from Poiseuille's law at Re where the Newtonian flow stayed laminar. Accompanying this transition was a flattening of the velocity profile and an increased turbulent intensity with values somewhere between the laminar and fully turbulent profile. On further increasing Re, this so-called "early turbulence" continuously gave way to a drag-reduced turbulent state.

Fast track 40 years, key insights into these observations were obtained by Samanta *et al.* [2013] who experimentally examined the flow of polymer solutions through pipes at various concentrations. For sufficiently viscoelastic solutions which corresponded to polymer concentrations in the order of 500ppm, the authors observed a direct transition of the unperturbed laminar state to a self-sustained chaotic flow state. This

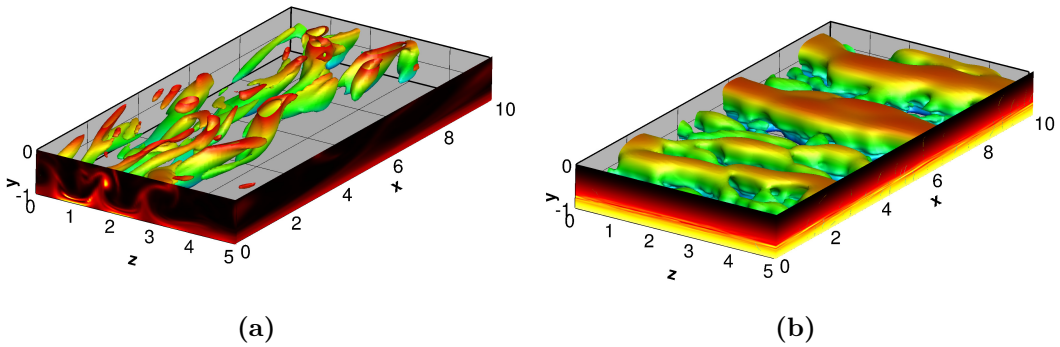

Figure 2.1: Flow structures observed in (a) drag-reduced Newtonian turbulence and (b) elastoinertial turbulence at $Re = 1500$. Shown are isosurfaces of vortex strength, Q = 0.075 for (a) and 0.00014 for (b). Structures are color coded based on distance from the wall - blue near the wall and red near the channel centerline. On the vertical planes are color contours of polymer stretch. Lower half of the channel geometry is shown for clarity.

flow state persisted down to $Re = 800$, well below the $Re \approx 2000$ value at which Newtonian turbulence can be sustained in pipes. This qualitatively different chaotic flow state was dubbed elastoinertial turbulence (EIT). The authors further inferred insights into the nature of this polymer-driven chaotic flow state using computations. The viscoelastic fluid was modeled using the FENE-P constitutive equation - a common approach to model dilute polymer solutions. At parameter values similar to the experiments, the authors showed that EIT displayed tilted sheets of polymer stretch with weak spanwise-oriented flow structures that filled the computational domain - a sharp contrast to the quasistreamwise vortex structure that make up inertia-driven Newtonian turbulence.

Shown in figure 2.1 are representative snapshots of (a) drag-reduced Newtonian turbulence and (b) elastoinertial turbulence at low transitional $Re = 1500$ obtained from channel flow simulations of dilute polymeric solutions. For drag-reduced Newtonian turbulence, we see streamwise (x) aligned quasistreamwise vortices and plumes

of polymer stretch due to them. As described in Samanta *et al.* [2013], EIT displays much weaker spanwise (z) oriented flow structures and sheets of polymer stretch.

Chandra *et al.* [2018] further investigated the viscoelastic effects on the laminar-turbulent transition in the flow through microtubules. For the Newtonian flow, the authors observed a natural transition i.e. without explicit external forcing at the well known value, $Re = 2000$. Consistent with Samanta *et al.* [2013], on increasing polymer concentration, they first noticed an initial delay in transition with an increase in the transition Re to 2500. On further increasing the concentration, this transition Re decreased with an early transition to EIT down to $Re = 800$.

While most experimental studies of viscoelastic transition have been carried out in pipes, Srinivas and Kumaran [2017] demonstrated a qualitative similarity in the transition scenario in soft-walled microchannels. For polymer concentrations beyond a threshold value, they observed a significant decrease in the transition Re down to a value of 35. To put into context, Newtonian transition was seen at $Re \approx 300$.

The experimental investigations highlighted so far demonstrate a robustness in the early transition of dilute polymer solutions with sufficient levels of viscoelasticity. The flow regime accompanying this transition, aptly termed elastoinertial turbulence (EIT), displays a marked difference in structures and statistics in comparison to Newtonian turbulence. These observations hint at new polymer-driven self-sustaining mechanisms coming into existence to sustain this chaotic flow state with a friction factor scaling remarkably close to the MDR scaling [Samanta *et al.*, 2013]. However, a deeper understanding of the mechanisms underlying EIT is still lacking and is an active area of research.

Key insights into these mechanisms were obtained from pipe flow experiments by

Choueiri *et al.* [2018] . At low transitional $Re = 3150$ and varying polymer concentration in a quasi-static manner, the authors observed a complete relaminarization of Newtonian turbulence in a narrow window of concentrations followed by a "reentrant transition" to EIT characterized by "weak, elongated streaks" of streamwise velocity fluctuation. Accompanying this reentrant transition was an increase in the friction factor from the laminar to MDR value for the chosen parameter set. These observations bring to light two distinct self-sustenance mechanisms in dilute polymer solutions - one that is suppressed by viscoelasticity (Newtonian turbulence) and one that is promoted (elastoinertial turbulence). At higher transitional $Re = 5200, 10000$, the authors observed the more traditional route from Newtonian turbulence to MDR with a monotonic drop in friction factor. Even at these higher Re, the flow state at MDR was EIT with weak, elongated velocity streaks.

The observations covered so far can be summarized in figure 2.2. It must be emphasized that this diagram is highly schematic with boundaries between different regimes generally not horizontal or vertical. An experimental path with increasing flow rate corresponds to oblique lines of constant elasticity number El. For the Newtonian case, $El = 0$ and an experimental path on increasing Re transitions to Newtonian turbulence with 3D quasistreamwise vortices. For pipe flow, this transition happens at $Re \approx 2000$ and ≈ 1000 for channel flow. As pointed out in Samanta *et al.* [2013], Chandra *et al.* [2018], there is a delay in transition to Newtonian-type (NT) turbulence towards higher Re on increasing viscoelasticity and this scenario is sketched here using a blue-dashed lines. More recently, this phenomena was captured by studying the effect of viscoelasticity on 3D ECS by Li and Graham [2007] who observed that these structures are weakened to the point that the ECS no longer self-

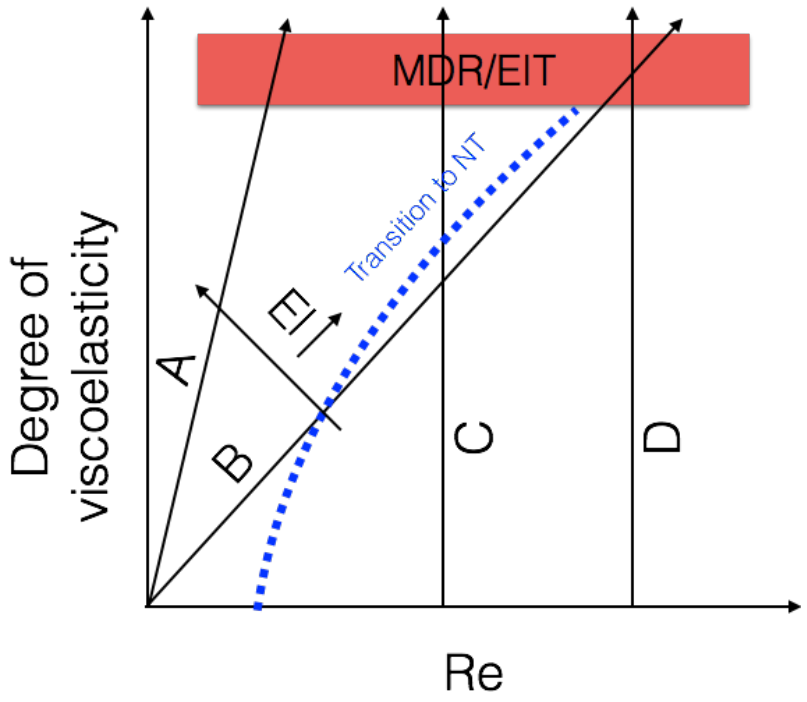

Figure 2.2: Parameter space of turbulence in dilute polymer solution summarizing experimental observations of viscoelastic transition. Here, 'NT' stands for Newtonian-type turbulence characterized by 3D quasistreamwise vortices. Boundaries are fuzzy and not necessarily horizontal or vertical.

sustain and lose existence. These observation tie back to other studies of polymer drag reduction (see Ptasinski *et al.* [2001], Escudier *et al.* [2009] for example) which report decreasing velocity fluctuations and Reynolds shear stress on increasing viscoelasticity which point to a weakening of the near-wall Newtonian turbulent structure. Path B corresponds to such studies, where transition to Newtonian-type turbulence is first observed before reaching MDR/EIT on further increasing flow rate. At sufficiently high El, illustrated by path A, the laminar flow can directly transition to EIT with an MDR friction factor at significantly lower Re reflecting the experimental results by Forame *et al.* [1972], Zakin *et al.* [1977], Samanta *et al.* [2013]. Other studies such as Choueiri *et al.* [2018] are done at constant Re. Path C corresponds to their results at $Re = 3150$, where they observe a relaminarzation of NT (above the blue-dashed

line) followed a reentrant transition to EIT at higher viscoelasticity. At higher Re, path D here, a continuous pathway from Newtonian turbulence to EIT is observed. In the present work, we use direct numerical simulations (DNS) to address these observations and gain a deeper understanding of mechanisms underlying EIT.

Chapter 3

Models and numerical methods for direct numerical simulations

This chapter describes the computational models and methods used for direct numerical simulations (DNS) of dilute polymer solutions. We first go over the coarse-grained modeling of polymer molecules in section 3.1 before diving into the details of the DNS in section 3.2.

3.1 Coarse-graining from molecular picture

Most applications of interest involves the flow of long chain polymer molecules dissolved in a "good solvent" where the monomers prefer the solvent over monomer-monomer interactions. At equilibrium, the life of a polymer molecule is dictated by a balance between an entropic preference to have an "ideal" conformation and

This chapter includes content from: Graham, M. D. and Shekar, A. (2021). Instabilities, nonlinear dynamics and turbulence in complex fluids. To be submitted to Journal of Fluid Mechanics - Perspectives.

an energetic preference to minimize monomer-monomer interactions in a good solvent [Rubinstein and Colby, 2003]. Polymer molecules thus end up displaying a self-avoiding "random-walk" configuration. The simplest micromechanical model of polymer molecules that captures the key thermodynamic features of dilute polymer solutions is the bead-spring dumbbell model which models the polymer molecules as two spherical beads connected by a spring. Many of the principles underlying the coarse-grained modeling of polymer dynamics can be found in [Bird *et al.*, 1987, Rubinstein and Colby, 2003, Doi and Edwards, 1986, Larson, 1999, Öttinger, 1996, de Gennes, 1979, Strobl, 1996]. The modeling framework is described in detail in Bird *et al.* [1987], Graham [2018a]. Below, we briefly go over the details.

The most widely used form of the dumbbell model simply takes the beads to be spheres, each with Stokes friction coefficient ζ, at positions $\boldsymbol{R}_1(t)$ and $\boldsymbol{R}_2(t)$. Neglecting inertia, the force balance on bead 1 has three components: the drag force

$$\boldsymbol{F}_{\text{drag},1} = -\zeta\left(\frac{d\boldsymbol{R}_1}{dt} - \boldsymbol{v}(\boldsymbol{R}_1)\right), \tag{3.1}$$

where $\boldsymbol{v}(\boldsymbol{R}_1)$ is the fluid velocity at the position of the bead; the spring force

$$\boldsymbol{F}_{\text{spring},1} = H\boldsymbol{Q}, \tag{3.2}$$

where $H = 3k_BT/L_KL = 3k_BT/R_0^2$ and $\boldsymbol{Q} = \boldsymbol{R}_2 - \boldsymbol{R}_1$ is the *end-to-end vector* between the beads; and a fluctuating random force $\boldsymbol{F}_{\text{fluc},1}(t)$ that arises from the collisions of the randomly moving solvent molecules with the bead. This is the force

that leads to Brownian motion. It satisfies

$$\langle \boldsymbol{F}_{\text{fluc},1}(t)\rangle = \boldsymbol{0}, \qquad \langle \boldsymbol{F}_{\text{fluc},1}(t)\boldsymbol{F}_{\text{fluc},1}(t')\rangle = 2k_BT\zeta\boldsymbol{\delta}\delta(t-t'), \tag{3.3}$$

where $\langle\ \rangle$ denotes ensemble average. Analogous expressions exist for bead 2. The forces on each bead sum to zero, and additionally $\boldsymbol{F}_{\text{spring},2} = -\boldsymbol{F}_{\text{spring},1}$, leading to evolution equations

$$\frac{d\boldsymbol{R}_1}{dt} = \boldsymbol{v}(\boldsymbol{R}_1) + \frac{1}{\zeta}\boldsymbol{F}_{\text{spring},1} + \frac{1}{\zeta}\boldsymbol{F}_{\text{fluc},1}, \tag{3.4}$$

$$\frac{d\boldsymbol{R}_2}{dt} = \boldsymbol{v}(\boldsymbol{R}_2) - \frac{1}{\zeta}\boldsymbol{F}_{\text{spring},1} + \frac{1}{\zeta}\boldsymbol{F}_{\text{fluc},2}. \tag{3.5}$$

The random forces $\boldsymbol{F}_{\text{fluc},1}$ and $\boldsymbol{F}_{\text{fluc},2}$ are independent.

It is generally more useful to consider the evolution of the end-to-end vector $\boldsymbol{Q}$ and center of mass $\boldsymbol{R}_\text{c} = (\boldsymbol{R}_1 + \boldsymbol{R}_2)/2$: these evolve as

$$\frac{d\boldsymbol{Q}}{dt} = (\boldsymbol{v}(\boldsymbol{R}_2) - \boldsymbol{v}(\boldsymbol{R}_1)) - \frac{2}{\zeta}\boldsymbol{F}_{\text{spring}} + \frac{1}{\zeta}\boldsymbol{F}_{\text{fluc},Q}, \tag{3.6}$$

$$\frac{d\boldsymbol{R}_\text{c}}{dt} = \frac{1}{2}\left(\boldsymbol{v}(\boldsymbol{R}_1) + \boldsymbol{v}(\boldsymbol{R}_2)\right) + \frac{1}{2\zeta}\boldsymbol{F}_{\text{fluc},R}. \tag{3.7}$$

Here $\boldsymbol{F}_{\text{fluc},Q}$ and $\boldsymbol{F}_{\text{fluc},R}$ are independent zero-mean random variables that satisfy

$$\langle \boldsymbol{F}_{\text{fluc},Q}(t)\boldsymbol{F}_{\text{fluc},Q}(t')\rangle = \boldsymbol{F}_{\text{fluc},R}(t)\boldsymbol{F}_{\text{fluc},R}(t')\rangle = 4k_BT\zeta\boldsymbol{\delta}\delta(t-t'). \tag{3.8}$$

Polymer molecules are generally very small compared to the length scales of a

flow, in which case we can linearize the velocity field around $\boldsymbol{R}_c$ to yield

$$\frac{d\boldsymbol{Q}}{dt} = \boldsymbol{\nabla v}^T \cdot \boldsymbol{Q} - \frac{2}{\zeta}\boldsymbol{F}_{\text{spring}} + \frac{1}{\zeta}\boldsymbol{F}_{\text{fluc},Q}, \tag{3.9}$$

$$\frac{d\boldsymbol{R}_{\text{c}}}{dt} = \boldsymbol{v} + \frac{1}{2\zeta}\boldsymbol{F}_{\text{fluc},R}, \tag{3.10}$$

where $\boldsymbol{v}$ and $\boldsymbol{\nabla v}$ are evaluated at $\boldsymbol{R}_{\text{c}}$. The evolution of the center of mass is simple to understand: the polymer is carried with the fluid motion while diffusing with a diffusivity $D_{\text{p}} = k_B T/2\zeta$. In many applications, the Peclet number associated with this diffusivity is very large and polymer center of mass diffusion is negligible. Effects of nonuniform polymer concentration effects will not be further discussed in this work. In the absence of diffusion, the time derivative in (3.9) can be taken to be the substantial derivative; this equation describes the *Lagrangian* evolution of $\boldsymbol{Q}$. If we use the Hooke's law expression for $\boldsymbol{F}_{\text{spring}}$, then

$$\frac{d\boldsymbol{Q}}{dt} = \boldsymbol{\nabla v}^T \cdot \boldsymbol{Q} - \frac{2H}{\zeta}\boldsymbol{Q} + \frac{1}{\zeta}\boldsymbol{F}_{\text{fluc},Q}. \tag{3.11}$$

At equilibrium, the spring and Brownian forces balance to give that $\langle \boldsymbol{Q} \cdot \boldsymbol{Q} \rangle = 3k_B T/H = R_0^2 = L_K L$.

The Hookean spring model is fine near equilibrium, but does not account for the fact that the polymer subchain connecting each bead has finite length so the spring force must diverge as $(\boldsymbol{Q} \cdot \boldsymbol{Q})^{1/2} \equiv Q \to L$. The most widely used spring model, is the simple "Warner" or FENE (Finitely Extensible Nonlinearly Elastic) spring force [Bird *et al.*, 1987]:

$$\boldsymbol{F}_{\text{spring}} = \frac{H\boldsymbol{Q}}{1 - Q^2/L^2}. \tag{3.12}$$

For $Q \ll L$ this reduces as it should to a Hookean spring model.

With this model of the polymer dynamics in hand, we turn to the consideration of the polymer contribution to the stress in the fluid. The polymer number density n will be taken to be constant and the polymer molecules much smaller than the scales of the flow. In this case we can treat ensemble averages as the same as volume averages over scales large compared to the molecules, but small compared to the flow scales. There are two contributions to the stress $\boldsymbol{\sigma}_{\mathrm{p}}$ in the fluid arising from the presence of the polymers [Bird *et al.*, 1987, Graham, 2018b]. The first is comes from the momentum flux due to the thermal motion of the two beads, which each have average kinetic energy $3k_BT/2$. The resulting "kinetic" contribution to the stress is

$$\boldsymbol{\sigma}_{\mathrm{kin}} = -2nk_BT\boldsymbol{\delta}, \tag{3.13}$$

where $\boldsymbol{\delta}$ is the identity. The second arises from the force dipoles exerted by the polymer molecules on the fluid, just as in a suspension of rigid particles [Batchelor, 1970]. Since a dumbbell is basically already just a force dipole, the form of this contribution to the stress has simple form

$$\boldsymbol{\sigma}_{\mathrm{dipole}} = n\langle \boldsymbol{Q}\boldsymbol{F}_{\mathrm{spring}} \rangle. \tag{3.14}$$

The total polymer contribution to the stress is then

$$\boldsymbol{\sigma}_{\mathrm{p}} = \boldsymbol{\sigma}_{\mathrm{kin}} + \boldsymbol{\sigma}_{\mathrm{dipole}}. \tag{3.15}$$

At equilibrium, $\boldsymbol{\sigma}_{\mathrm{dipole}} = nk_BT\boldsymbol{\delta}$. This is easy to derive for the Hookean dumbbell

model, where

$$\boldsymbol{\sigma}_{\text{dipole}} = nH\langle \boldsymbol{QQ} \rangle, \tag{3.16}$$

and at equilibrium $\langle \boldsymbol{QQ} \rangle = k_B T / H\boldsymbol{\delta}$. Thus at equilibrium, the polymer contribution to the stress is

$$\boldsymbol{\sigma}_{\text{p,eq}} = -nk_B T\boldsymbol{\delta}. \tag{3.17}$$

This is simply the osmotic stress present in any dilute suspension of Brownian particles. The deviation of the stress from this equilibrium value, which we denote $\boldsymbol{\tau}_p$, is

$$\boldsymbol{\tau}_p = \boldsymbol{\sigma}_{\text{p}} - \boldsymbol{\sigma}_{\text{p,eq}} = n\langle \boldsymbol{QF}_{\text{spring}} \rangle - nk_B T\boldsymbol{\delta}. \tag{3.18}$$

The total stress $\boldsymbol{\sigma}$ in the solution is

$$\boldsymbol{\sigma} = -(p + nk_B T)\boldsymbol{\delta} + 2\eta_{\text{s}}\mathbf{E} + \boldsymbol{\tau}_{\text{p}}, \tag{3.19}$$

where $\mathbf{E}$ is the rate of strain tensor and η_{s} the solvent viscosity. For the Hookean dumbbell $\boldsymbol{F}_{\text{spring}} = H\boldsymbol{Q}$, we can define a dimensionless *conformation tensor*

$$\boldsymbol{\alpha} = \frac{H}{k_B T}\langle \boldsymbol{QQ} \rangle, \tag{3.20}$$

and a *shear modulus* $G = nk_B T$. Now (3.18) can be written

$$\boldsymbol{\tau}_{\text{p}} = G\left(\boldsymbol{\alpha} - \boldsymbol{\delta}\right). \tag{3.21}$$

Using (3.11), an evolution equation for $\boldsymbol{\alpha}$ can be found:

$$\frac{D\boldsymbol{\alpha}}{Dt} = \boldsymbol{\nabla v}^T \cdot \boldsymbol{\alpha} + \boldsymbol{\alpha} \cdot \boldsymbol{\nabla v} - \frac{1}{\lambda}\boldsymbol{\tau}_\mathrm{p}. \tag{3.22}$$

Above we introduced the FENE spring law (3.12) to account for the finite length of real polymer molecules. To derive a closed form expression for the polymer contribution to the stress tensor, it is necessary to use an approximate version of (3.12), where Q^2 is replaced by its ensemble average:

$$\boldsymbol{F}_\mathrm{spring} = \frac{H\boldsymbol{Q}}{1 - \langle Q^2 \rangle / L^2}. \tag{3.23}$$

This is called the *Peterlin approximation* and (3.23) the FENE-P spring model [Bird *et al.*, 1987]. With this spring law we can write (3.18) as

$$\boldsymbol{\tau}_\mathrm{p} = G\left(\frac{\boldsymbol{\alpha}}{1 - \mathrm{Tr}\,\boldsymbol{\alpha}/b} - \boldsymbol{\delta}\right), \tag{3.24}$$

where $b = L^2 H / k_B T = 3N_K \gg 1$. To put into context, for a commonly used drag reducing agent, polyethylene oxide (PEO), the value of b works out to be 6400 for a molecular weight of 0.25 million and 100,000 for a molecular weight of 4 million. These values encompass a range of molecular weights used in polymer drag reduction experiments [Virk *et al.*, 1970].

The above equation, along with (3.22) and (3.19) describe the evolution of stress for the FENE-P model. In addition to preventing polymer molecules from stretching indefinitely, FENE-P also displays shear-thinning, in qualitative agreement with experimental observations. The FENE-P model is widely used in simulations of polymer

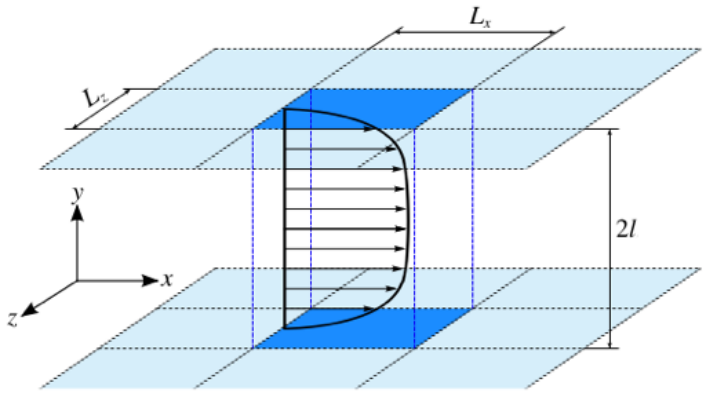

Figure 3.1: Schematic of the computational domain used for direct numerical simulations.

solution fluid dynamics, including the computational studies described below.

3.2 Direct numerical simulations

We consider incompressible, pressure-driven channel flow with constant mass flux. Figure 3.1 shows a schematic of the computational domain of interest. The x, y and z axes are aligned with the streamwise (overall flow), wall-normal and spanwise directions, respectively. Lengths are scaled by the half channel height l so the dimensionless channel height $L_y = 2$. The domain is periodic in x and z with periods L_x and L_z. Velocity $\boldsymbol{v}$ is scaled with the Newtonian laminar centerline velocity U; time t with l/U, and pressure p with ρU^2, where ρ is the fluid density. The polymer stress tensor $\boldsymbol{\tau}_p$ is related to the polymer conformation tensor $\boldsymbol{\alpha}$ (second moment of the probability distribution for the polymer end-to-end vector) through the FENE-P constitutive relation, which models each polymer molecule as a pair of beads connected by a nonlinear spring with maximum extensibility b.

The Navier-Stokes equations which govern fluid flow are coupled with the FENE-P equations forming the governing equations listed below:

$$\frac{\partial \boldsymbol{v}}{\partial t} + \boldsymbol{v} \cdot \boldsymbol{\nabla} \boldsymbol{v} = -\boldsymbol{\nabla} p + \frac{\beta}{Re} \nabla^2 \boldsymbol{v} + \frac{(1-\beta)}{Re\, Wi} \left(\boldsymbol{\nabla} \cdot \boldsymbol{\tau}_{\mathrm{p}} \right), \tag{3.25}$$

$$\boldsymbol{\nabla} \cdot \boldsymbol{v} = 0, \tag{3.26}$$

$$\boldsymbol{\tau}_p = \frac{\boldsymbol{\alpha}}{1 - \frac{\mathrm{tr}(\boldsymbol{\alpha})}{b}} - \boldsymbol{I}, \tag{3.27}$$

$$\frac{\partial \boldsymbol{\alpha}}{\partial t} + \boldsymbol{v} \cdot \boldsymbol{\nabla} \boldsymbol{\alpha} - \boldsymbol{\alpha} \cdot \boldsymbol{\nabla} \boldsymbol{v} - (\boldsymbol{\alpha} \cdot \boldsymbol{\nabla} \boldsymbol{v})^{\mathrm{T}} = \frac{-1}{Wi} \boldsymbol{\tau}_p. \tag{3.28}$$

Here Reynold number $Re = \rho U l/(\eta_{\mathrm{s}} + \eta_{\mathrm{p}})$, where η_s and η_p are the solvent and polymer contributions to the zero-shear rate viscosity. The viscosity ratio $\beta = \eta_{\mathrm{s}}/(\eta_{\mathrm{s}} + \eta_{\mathrm{p}})$; polymer concentration is proportional to $1 - \beta$. $\beta = 1$ corresponds to the Newtonian limit with no polymer contribution. The Weissenberg number $Wi = \lambda U/l$, where λ is the polymer relaxation time, measures the ratio between the relaxation time for the polymer and the shear time scale for the flow.

For chapter 4, computations are performed using the open source code `ChannelFlow`, which performs direct simulations as well as computing exact coherent states for Newtonian channel flow by Newton-Raphson iteration. Please refer to Gibson [2012] for additional details.

For results described in other chapters, a finite difference scheme and a fractional time step method are adopted for integrating the Navier-Stokes equation. Second-order Adams-Bashforth and Crank-Nicolson methods are used for convection and diffusion terms, respectively. The FENE-P equation is discretized using a high resolution central difference scheme which guarantees the positive definiteness of $\boldsymbol{\alpha}$ without the need for any artificial diffusivity (AD)[Kurganov and Tadmor, 2000, Vaithianathan *et al.*, 2006, Dallas *et al.*, 2010].

Past computational studies have relied on adding AD into the FENE-P equation for numerical stability purposes. This has a smearing effect on sharp gradients, leading to an underestimation of polymer stress. This is especially important in the EIT regime where sheets of polymer stretch with sharp gradients are the dominant structures. In fact, too much AD can lead to relaminarization of EIT [Sid *et al.*, 2018]. A detailed description on the numerical algorithm used in this study can be found in Wang [2017].

Chapter 4

Exact coherent states with hairpin-like vortex structure in channel flow[a]

4.1 Introduction

Turbulent flows are organized into a hierarchy of patterns called "coherent structures" that persistent through space and time. These coherent structures continually draw and dissipate energy from the mean flow and are responsible for the higher friction losses associated with turbulent flows. In wall bounded turbulence - the focus of our work, the primary culprits which are observed in the near-wall region include quasistreamwise and hairpin vortices. From the context of flow control, gaining an understanding how these coherent motions self-sustain can influence flow control

[a]This chapter includes content from: Shekar, A., and Graham, M. D. (2018). Exact coherent states with hairpin-like vortex structure in channel flow. Journal of Fluid Mechanics 849, 76-89.

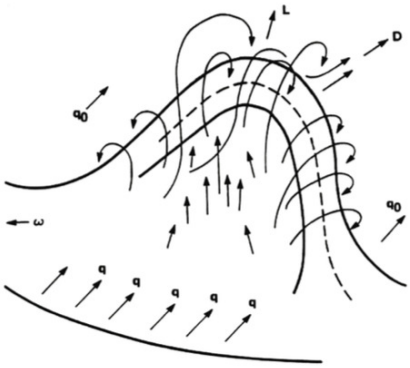

(a)

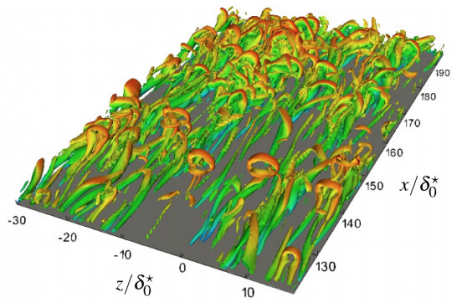

(b)

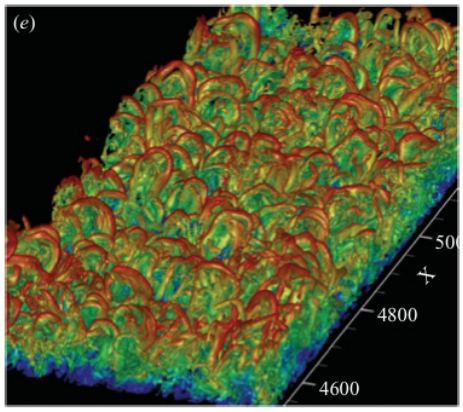

(c)

Figure 4.1: (a) Theodorsen's conceptualized picture of a hairpin [Theodorsen, 1952]. (b) Isosurfaces of λ_2-criterion showing hairpin-like structures during transition in boundary layers[Eitel-Amor *et al.*, 2015].(c) Isosurfaces of vortex strength Q illustrating hairpin vortices in direct simulation results for a turbulent boundary layer[Wu and Moin, 2009]. Figures (b) and (c) reproduced with permission from Eitel-Amor *et al.* [2015] and Wu and Moin [2009] respectively.

strategies that target these sustenance mechanisms. In this chapter, we use ideas from dynamical systems theory to gain insights into the behavior of hairpin vortices - an important coherent structure in wall bounded turbulence.

Ever since the observations of Theodorsen [1952] (Figure 4.1a), the role of *hairpin* or *horseshoe* vortices in turbulent shear flows has been an important topic in the study of turbulent structure [Robinson, 1991, Adrian, 2007, Smits *et al.*, 2011]. In

a wall-bounded flow, hairpin vortices are concentrated regions of vorticity whose shape is described by their name, with the "legs" of the hairpin comprising counter-rotating quasistreamwise vortices tilted upward away from the wall and joined by a "head" of primarily spanwise vorticity far from the wall where the mean velocity gradient (and thus mean spanwise vorticity) are small. Hairpin vortices have been observed in many contexts; for example, Figure 4.1b shows results from a simulation of transition, illustrating hairpin-like vortices with heads near the edge of the boundary layer. Duguet *et al.* [2012], in a study of transitional boundary layer flow, observe formation of hairpins just above the region where adjacent streamwise streaks "pinch" together, and the robustness of this process led the authors to suggest that it is a quasi-equilibrium feature of the flow. Figure 4.1c, from the boundary layer direct numerical simulation of Wu and Moin [2009] at transitional Reynolds numbers, shows isosurfaces of vortex strength that exhibit a "forest" of vortices with clear hairpin structure. Schlatter *et al.* [2014] also studied the presence of hairpins in boundary layers at transitional Reynolds numbers using interesting vortex eduction techniques. In fully developed turbulence, hairpin vortex structures and packets thereof are closely related to the formation of very large-scale uniform momentum zones Adrian [2007]. Additionally, vortices of hairpin or related shape play a central role in the attached eddy hypothesis [Townsend, 1961, Perry and Chong, 1982, Woodcock and Marusic, 2015], an important model for the statistical structure of wall turbulence. The present work describes a traveling wave solution to the Navier–Stokes equations in minimal channel flow that displays hairpin-like vortices, demonstrating that such structures exist as autonomous, self-sustaining patterns.

Important insights into turbulent structure, especially near solid surfaces or at low

Reynolds number, have been gained in recent years by looking at turbulence through the lens of nonlinear dynamical systems theory, which relates observed dynamics to underlying state space structure. In all of the canonical wall-bounded shear flow geometries (pipe flow, channel flow, plane shear (Couette) flow), families of nonlinear traveling wave solutions to the Navier-Stokes equations (NSE) that govern fluid motion have been discovered [Waleffe, 1998, 2001, 2003, Wang *et al.*, 2007, Hof *et al.*, 2004, Eckhardt *et al.*, 2007, 2008, Duguet *et al.*, 2008b, Wedin and Kerswell, 2004]. They have also been found in the asymptotic suction boundary layer flow [Khapko *et al.*, 2013]. These solutions are often denoted "exact coherent states" (ECS). Related, but more complex states have been found as well, that are not pure traveling waves but rather "relative periodic orbits" that are time-periodic modulo a phase shift in one of the translation-invariant spatial directions [Duguet *et al.*, 2008a]. (A traveling wave is a relative equilibrium – a state that is time-invariant modulo phase shift in the downstream direction.) In minimal domains at Reynolds numbers near transition the turbulent dynamics have been found to be organized, at least in part, around these traveling wave and relative periodic orbit solutions (see, e.g. Gibson *et al.* [2008], Kawahara *et al.* [2012], Park and Graham [2015]). The present work exclusively considers traveling wave exact coherent states.

The basic scenario for appearance of these states is that as Re increases, they emerge in pairs with finite amplitude at so-called saddle-node bifurcations. The solution with the higher drag is called an "upper branch" (UB) solution while the other is a "lower branch" (LB). The lowest Reynolds number at which these solutions appear is slightly below the value where transition is observed in experiments. For channel flow, our focus here, transition occurs at a Reynolds number Re based on the

laminar centerline velocity of about 1000, while various families of ECS come into existence once $Re \gtrsim 660$ [Park and Graham, 2015, Wall and Nagata, 2016]. Other coherent states can arise through secondary bifurcations off of the states that appear in this way.

The spatial structure of the heretofore-discovered ECS is pairs of counter-rotating streamwise vortices, with the corresponding low-and high-speed streaks associated with the advection of the mean shear by the vortices. Letting x, y and z be the mean flow, wall-normal and spanwise directions, respectively, and L_x and L_z the spatial periods of the flow in x and z, respectively, traveling wave velocity fields $\boldsymbol{u}(x,y,z,t) = \boldsymbol{u}(x-ct,y,z)$ with wavespeed c have generally been sought in one of two invariant subspaces with respect to symmetry in the $x-z$ plane. If u, v and w are the velocity components in x, y, and z, solutions have been sought that satisfy either a simple reflection symmetry across $z = L_z/2$,

$$\begin{bmatrix} u & v & w \end{bmatrix} (x,y,z-L_z/2,t) = \begin{bmatrix} u & v & -w \end{bmatrix} (x,y,-(z-L_z/2),t) \tag{4.1}$$

or a "shift and reflect" symmetry, where

$$\begin{bmatrix} u & v & w \end{bmatrix} (x,y,z-L_z/2,t) = \begin{bmatrix} u & v & -w \end{bmatrix} (x+L_x/2,y,-(z-L_z/2),t). \tag{4.2}$$

The latter case leads to sinuous vortex structures, while the former leads to varicose or potentially sinucose ones [Waleffe, 1997]. (We address this distinction below.) The former symmetry is also that of an ideal hairpin vortex. In the case of channel flow, reflection symmetry across the centerplane of the channel $y = 0$ is also often imposed,

in which case

$$\begin{bmatrix} u & v & w \end{bmatrix}(x,y,z) = \begin{bmatrix} u & -v & w \end{bmatrix}(x,-y,z). \tag{4.3}$$

Finally, a symmetry that has not received much prior attention, but which turns out to be central to the present work, is the "xz-shift" symmetry condition

$$\begin{bmatrix} u & v & w \end{bmatrix}(x,y,z) = \begin{bmatrix} u & v & w \end{bmatrix}(x+L_x/2,y,z+L_z/2). \tag{4.4}$$

Traveling wave exact coherent states have been computed in the channel flow geometry by a number of authors [Waleffe, 2001, 2003, Nagata and Deguchi, 2013, Park and Graham, 2015, Zammert and Eckhardt, 2016, Rawat *et al.*, 2016, Wall and Nagata, 2016, Neelavara *et al.*, 2017]. None of these have reported a hairpin vortex structure. In the plane Couette flow case, Itano and Generalis [Itano and Generalis, 2009] reported an ECS that they described as a hairpin vortex state. (Gibson *et al.* [2009] also found the same solution family.) Indeed, vortex lines for this state do display a hairpin shape, but in their case the loop or "head" of the hairpin is near the wall, where the shear rate is highest. Thus the local vorticity is dominated by the mean shear, which is of course locally oriented in the z-direction. In contrast, hairpin vortices in turbulent flows (e.g. as in Figure 4.1c) have a head that is a localized region of z-oriented vorticity in a background of zero or very weak shear as arises near the centerline in channel flow or the outer edge of a boundary layer. Furthermore, inferring existence of hairpin vortices from vortex lines can be problematic: *any* vortex line that crosses a plane of reflection symmetry must do so normally: for example, even a pair of quasistreamwise vortices that satisfies (4.1) will display hairpin-shaped vortex lines. More generally, Robinson [1991] points out that "hairpin-shaped vorticity lines

are common in any turbulent shear flow, whether or not hairpin-shaped vortices are present". Figure 4 of Robinson [1991] illustrates this point. In our analysis below, we will infer hairpin-like vortex structure from vortex strength Q and direct examination of velocity and vorticity fields.

As noted above, ECS play a role in organizing the state space dynamics of turbulent flows. In shear flows whose laminar state is linearly stable (pipe flow, plane Couette flow, channel flow at low Reynolds number), an important role in organizing state space is also played by the boundary between initial conditions that laminarize and those that become turbulent. At long times, trajectories on this boundary approach *edge states* [Skufca *et al.*, 2006]. In boundary layer flow, Cherubini *et al.* [2011] showed the presence of two different edge states, one dominated by streamwise vortex structures and one by transient localized hairpins. The study of Duguet *et al.* [2012] described above also focuses on edge states and indicates that hairpin-vortex-like structures can be found on the laminar-turbulent boundary.

The present work, which focuses on the channel flow geometry, reports for the first time a family of traveling wave exact coherent states that displays a hairpin-like vortex structure. Below we describe the bifurcation diagram for this family, its connection to some previously known states, its structure, and initial evidence indicating its relationship to fully turbulent mean profiles.

4.2 Formulation

We consider incompressible Newtonian flow in the plane Poiseuille (channel) geometry, driven with a constant volumetric flux. The x, y and z coordinates are aligned

with the streamwise, wall-normal, and spanwise directions, respectively. Periodic boundary conditions are imposed in the x and z directions with fundamental periods L_x and L_z, and no-slip conditions are imposed at the walls $y = \pm h$, where $h = L_y/2$ is the half-channel height. Using the half-height h of the channel and the laminar centerline velocity U_c as the characteristic length and velocity scales, respectively, the nondimensionalized Navier-Stokes equations are then given as

$$\frac{\partial \boldsymbol{u}}{\partial t} + \boldsymbol{u} \cdot \nabla \boldsymbol{u} = -\nabla p + \frac{1}{Re} \nabla^2 \boldsymbol{u}, \quad \nabla \cdot \boldsymbol{u} = 0. \tag{4.5}$$

Here, we define the laminar equivalent Reynolds number for the given volumetric flux as $Re_c = U_c h/\nu$, where ν is the kinematic viscosity of the fluid. We fix the bulk velocity (volumetric flux) U_b at the laminar value $2U_c/3$, so the Reynolds number Re_b based on bulk velocity is given by $Re_b = 2Re/3$. Characteristic inner scales are the friction velocity $u_\tau = (\bar{\tau}_w/\rho)^{1/2}$ and the near-wall length scale or wall unit $\delta_\nu = \nu/u_\tau$, where ρ is the fluid density and $\bar{\tau}_w$ is the time- and area-averaged wall shear stress. As usual, quantities nondimensionalized by these inner scales are denoted with a superscript "+". The friction Reynolds number is then defined as $Re_\tau = u_\tau h/\nu = h/\delta_\nu$.

Computations are performed using the open source code `ChannelFlow`, which performs direct simulations as well as computing exact coherent states by Newton-Raphson iteration [Gibson, 2012]. In this study, we focus on the domain $L_x \times L_y \times L_z = \pi \times 2 \times \pi/2$, the same box size as used in our prior ECS study [Park and Graham, 2015]. Fourier-Chebyshev-Fourier spectral spatial discretization is applied to all variables, using meshes with $N_x \times N_y \times N_z$ collocation points (in x, y, and z). A typical resolution

used is $(N_x, N_y, N_z) = (48, 81, 48)$, which we have verified is sufficient for converged solutions in the Reynolds number range examined here.

The exact coherent states computed and studied here all satisfy reflection symmetry across $z = L_z/2$, as given by (4.1), as well as across the centerplane of the channel $y = 0$, as given by (4.3). The solutions of central interest here additionally satisfy the xz-shift symmetry given by (4.4). There are of course other channel flow ECS that do not obey these symmetries (e.g. Waleffe [2001, 2003], Nagata and Deguchi [2013], Gibson and Brand [2014], Neelavara *et al.* [2017]). All turbulent trajectories reported here are computed without imposing any symmetries on the flow field.

4.3 Results and discussion

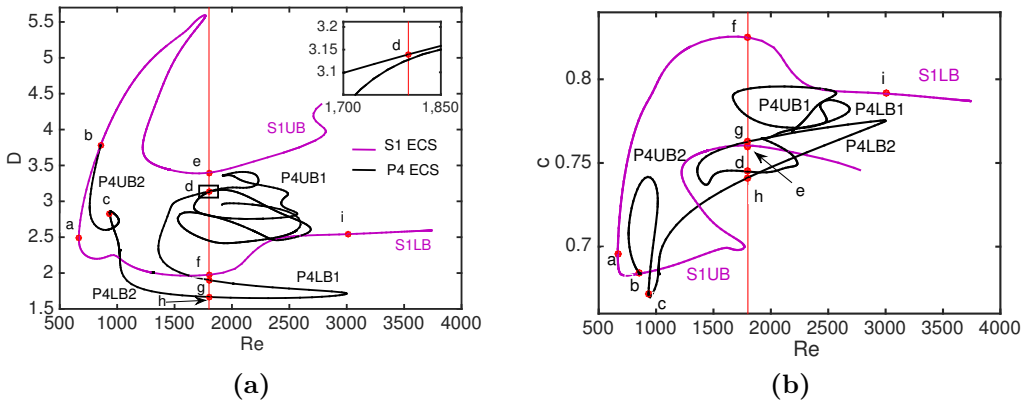

Figure 4.2: Bifurcation diagram in terms of (a) dissipation rate D *vs.* Re and (b) wave speed c *vs.* Re. Inset in (a) is a zoom-in of the box close to point **d**.

Figure 4.2 is the bifurcation diagram for the ECS solutions that we have computed in this study, shown in terms of dissipation rate D and streamwise wavespeed c *vs.* Re. Two solution families are shown. The one of primary interest is shown in

purple; it arises in a saddle-node bifurcation at $Re = 666$ (point **a** in Figure 4.2). This solution family satisfies both the z-reflection symmetry (4.1) and the xz-shift symmetry (4.4) and will be denoted S1. ECS with this set of symmetries have been reported in channel flow by Wall and Nagata [2016] (their MS-S, MS-A and TW2 families), but in general have received little attention in the literature. The vortex structure of this state at the bifurcation point is illustrated in Figure 4.3a, which shows a surface of vortex strength, $Q = \frac{1}{2}(\|\mathbf{\Omega}\|^2 - \|\mathbf{\Gamma}\|^2)$ in the bottom half of the channel ($y < 0$), where $\mathbf{\Omega}$ and $\mathbf{\Gamma}$ are the local vorticity and strain rate, respectively and $||\cdot||$ denotes Frobenius norm. This structure consists of two pairs of staggered counterrotating streamwise vortices that are mirror symmetric across $z = L_z/2$. By (4.3), a $y-$reflection-symmetric vortex structure arises in the top half of the channel ($y > 0$). Figure 4.3b shows the streamwise velocity at $y^+ = 20$, clearly illustrating the high degree of symmetry of the flow field and the "sinucose" nature of the flow pattern – there is a z-reflection-symmetric pair of sinuous low-speed streaks (dark). Observe that the low speed streaks (dark) "pinch" together at $x \approx 0.75$. As mentioned above, Duguet *et al.* [2012] observe in their study of edge states in boundary layer transition the formation of transient hairpins above pinches. We return to this point below.

On the upper (high dissipation) branch of S1, which we denote S1UB, a pitchfork bifurcation occurs at $Re = 855$ (point **b** in Figure 4.2). The bifurcating solutions lack the xz-shift symmetry, as shown by the streak structure for a solution on this branch at $Re = 935$ on Figure 4.4a (point **c** on the bifurcation diagram). This solution family is the P4 family reported by Park and Graham [2015]; indeed the way we found S1 was by continuation of P4. As Re increases along the P4 solution branch, the two mirror symmetric low-speed streaks merge into one; the structure evolves

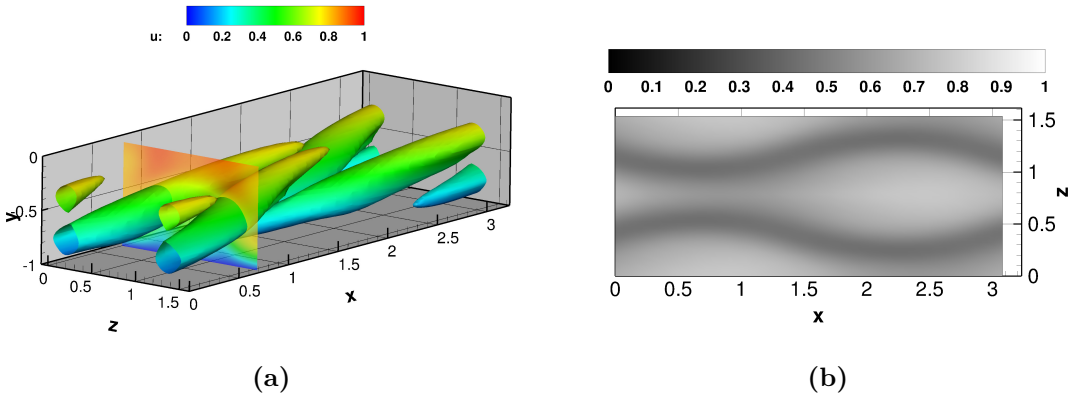

(a) **(b)**

Figure 4.3: (a) Vortical structure of the S1 solution at the saddle node bifurcation at $Re = 666$ (point **a** in figure 4.2). Isosurface of $Q = 0.05$ is shown with colors indicating distance from wall – blue near wall, red near center. A color contour plot of streamwise velocity at $x = 0.75$ is also shown. (b) Streamwise velocity u at $y^+ = 20$.

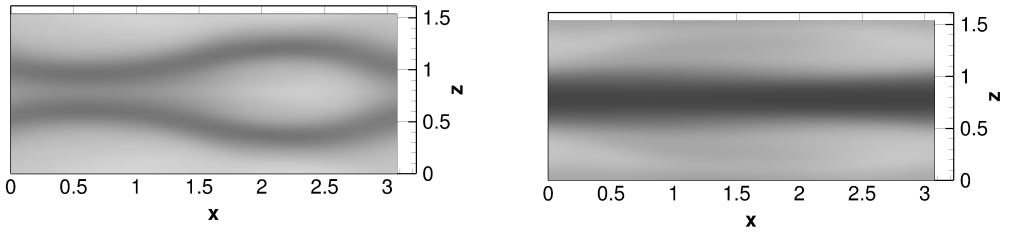

(a) **(b)**

Figure 4.4: Streamwise velocity at $y^+ = 20$ on P4: (a) near the pitchfork at $Re = 935$ (point **c** in Figure 4.2), (b) at $Re = 1800$ (point **d**).

from sinucose to varicose. Figure 4.4b shows this varicose structure at point **d** on the bifurcation diagram. Upon continuation to higher Re, P4 turns back on itself several times in saddle-node bifurcations resulting in a rather tangled bifurcation diagram.

Now we return our attention to S1. The upper branch (higher dissipation) solution displays an initial sharp increase in D with distance from the bifurcation point and the structure that emerges on this branch is very interesting and important. Recall the vortical structure of S1 at its inception, as shown in Figure 4.3a. This is a

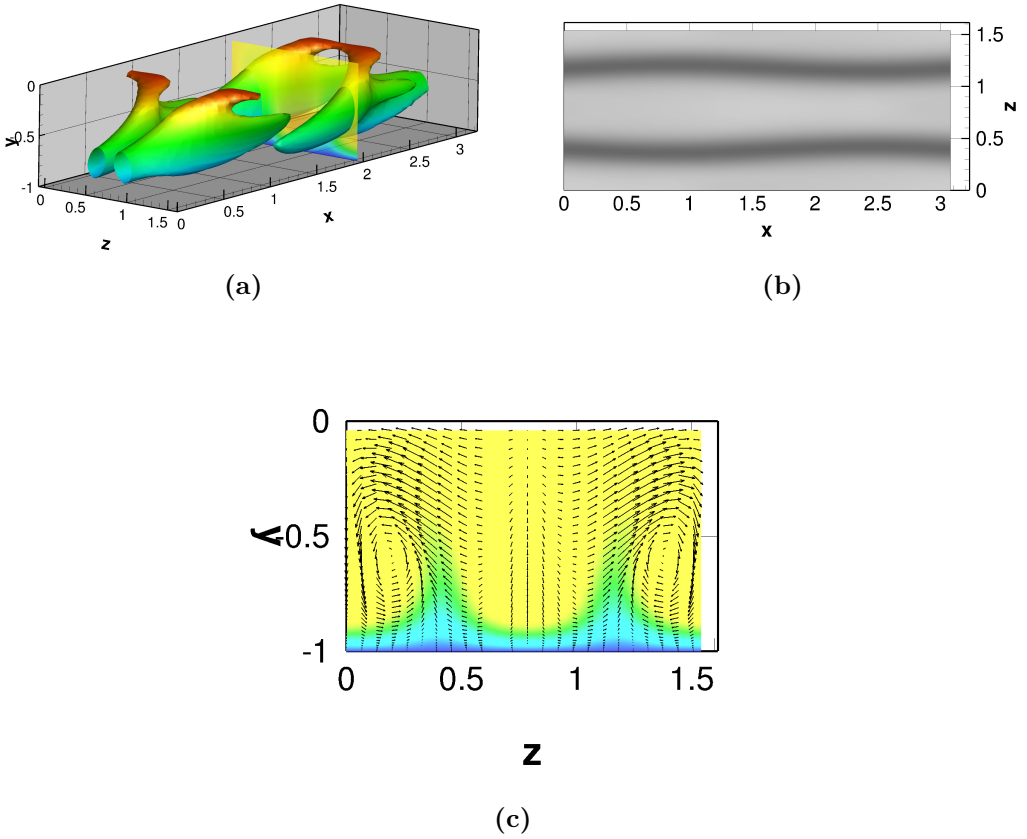

Figure 4.5: (a) Structure on S1UB at $Re = 1800$ (point **e**). Isosurface of $Q = 0.072$ with slice of u at $x = 2$ is shown. The maximum value of Q on the z midplane is $Q = 0.096$.(b) Streamwise velocity at $y^+ = 20$. (c) Streamwise velocity u at position shown in (a) at $x = 2$ with arrows of in-plane velocity vectors.

counter-rotating streamwise vortex structure, as expected for near-wall turbulence. By contrast, Figure 4.5a shows the vortical structure of S1UB at $Re = 1800$ (point **e** on the bifurcation diagram). By this point, the structure has evolved to become a self-sustaining combination of streamwise vortex structure (blue and and green) near the wall and *hairpin-like* heads (red) near the centerplane. It is a microcosm of near-wall turbulence, where streamwise vortices dominate the structure close to the wall, with hairpins becoming dominant further away [Wu and Moin, 2009]. Here the heads

seem to be pulling ahead of the legs a bit, perhaps because of forward motion induced by the presence of a mirror-image hairpin head on the other side of the centerplane $y = 0$. Consistent with the observations of Duguet *et al.* [2012], the hairpins appear above pinches in the streak structure, the most apparent of which is at $x \approx 2.5$. The pinch here is less pronounced than that observed in Figure 4.3b. By symmetry, there are also pinches at $x \approx 1$ between the low speed streaks in the domain shown and those in the spanwise neighboring domains. Correspondingly, there are hairpin-like structures above these pinches. Half of each of these can be seen in Figure 4.5a. Overall, this ECS displays a staggered array of these structures.

From Figure 4.5b, we can estimate the width of the hairpin-like structure as the spacing between the streaks in the pinch region, which is about 1 in outer units. Similarly, from Figure 4.6a we can estimate the distance of the vortex head from the wall in the same units as 0.9. At $Re = 1800$, the friction Reynolds number $Re_\tau \approx 95$. As this quantity gives the scaling between outer and inner units, we see that the vortex structure here has spanwise and wall-normal dimensions of about 95 and 86 wall units, respectively. For comparison, Adrian [2007] describes a "mature" hairpin vortex packet as having similar size, with both width and height of about 100 wall units.

Further indication of the hairpin-like structure displayed by this ECS is illustrated in Figure 4.6a, which shows the velocity field and z-vorticity on the symmetry plane $z = L_z/2$ in a reference frame moving with the transverse vortex core. Toward the upper right of the plot the localized vortical motion corresponding to the hairpin head is clearly seen. It should be emphasized that this motion occurs just below the centerplane of the channel, where the mean shear and thus the mean z-vorticity

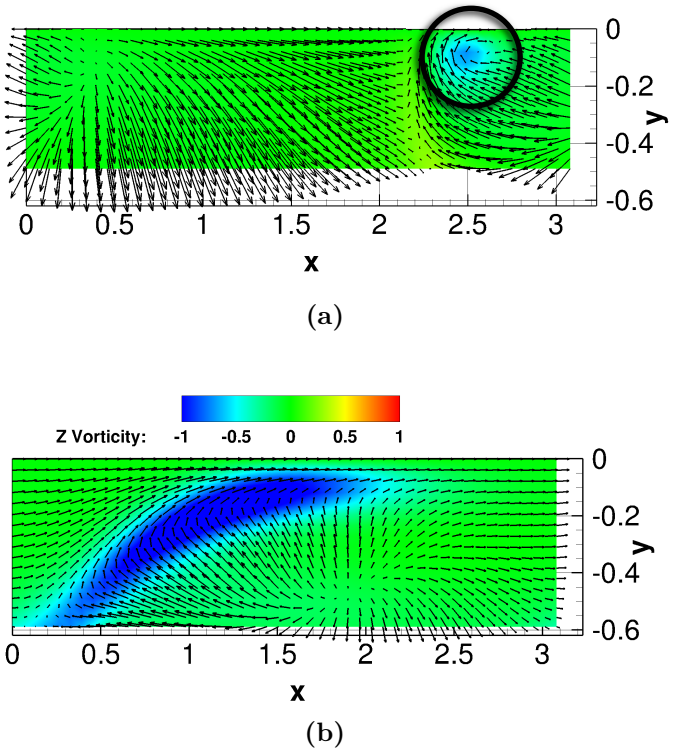

Figure 4.6: Contour of z-vorticity on the z-midplane with arrows indicating the velocity field in a frame moving at (a) $v_x = 0.76$ for S1UB at $Re = 1800$ and (b) $v_x = 0.74$ for S1 at the saddle-node bifurcation point $Re = 666$. In these plots the region between $y = -0.6$ and $y = 0$ (the centerplane) is shown.

vanish. This is in sharp contrast to the putative hairpin states described by Itano and Generalis [2009]; as noted above, those structures were only identified as hairpins based on the shape of the vortex lines, and additionally the hairpin shape of these lines was observed near the boundaries where there is a strong mean shear. In contrast, at $Re = 1800$, S1UB displays a clear localized region of cross-stream vorticity in a nearly shear-free mean flow that is connected to streamwise vortex motions closer to the wall. To our knowledge this is the first observation of a persistent hairpin-like vortex structure in an exact coherent state. Finally, Fig. 4.6b shows the same quantities plotted for the structure at $Re = 666$, i. e. right at the saddle-node bifurcation point. Consistent with the Q structure shown in Fig. 4.3a, no localization of z-vorticity is

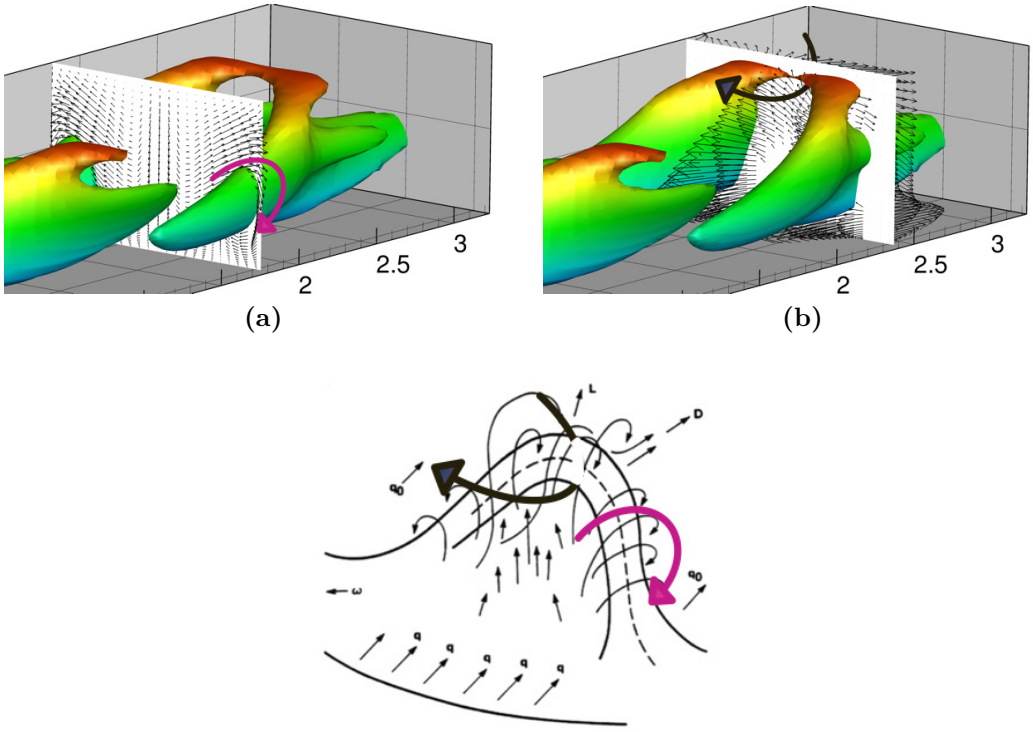

Figure 4.7: (a) In-plane velocity fluctuations on the legs of the vortex structure at $x = 1.82$ of S1UB, $Re = 1800$, (b) Out of plane velocity fluctuations on the head of the vortex structure at $x = 2.43$ of S1UB, $Re = 1800$ and (c) Theodorsen's picture of a hairpin vortex.

seen.

Completing our presentation of the structure of S1UB at $Re = 1800$, Figures 4.7a and 4.7b show the sense of rotation of the legs and head of the hairpin-like structure, respectively. Additionally, a strong Q2 ejection event ($u' < 0, v' > 0$) can be seen behind and below the vortex head. For comparison, Figure 4.7c shows again the Theodorsen picture; arrows have been added to all of these figures to indicate that S1UB does indeed display the same qualitative vortex structure as the original Theodorsen hairpin.

In addition to the vortex head and leg structure and the Q2 event behind the head just described, Adrian [2007] asserts, based on conditional averaging of the structure associated with Q2 events, that there are two additional ingredients to the signature of a hairpin vortex, a stagnation point separating Q2 and Q4 regions, corresponding to an inclined shear layer behind the hairpin head, and a low-speed streak well behind the vortex. These features are absent from the S1 ECS. Regarding the inclined shear layer and Q2/Q4 stagnation point, this is probably precluded by the reflection symmetry of the channel geometry and the proximity of the vortex heads to the centerplane. Regarding the trailing low speed streak, this is precluded by the symmetries (4.1) and (4.4), which yield a staggered arrangement of hairpin-like vortices. It should also be emphasized that the ECS structures described here are not conditionally-averaged – it is not obvious that instantaneous hairpin-like structures in flow will display all the features of a conditionally-averaged one. Nevertheless, it would be interesting to learn whether ECS exist that have aligned rather than staggered hairpin-like structures – these are likely to bear more similarity to the hairpins described by Adrian than is found here.

Nevertheless, as noted above, the scale of the S1 ECS vortex structure is similar to that reported by Adrian [2007]. Furthermore, it is consistent with observations of hairpins in the transition context as exemplified by the observations of Duguet *et al.* [2012], where hairpins arise above the pinch region between two low speed streaks. Perhaps the S1 ECS is more related and relevant to hairpins observed in transition than to those observed in fully turbulent boundary layers.

In prior observations, hairpin vortices have been observed as transient, spatiotemporally evolving structures. In contrast, the hairpin-like ECS structure observed in

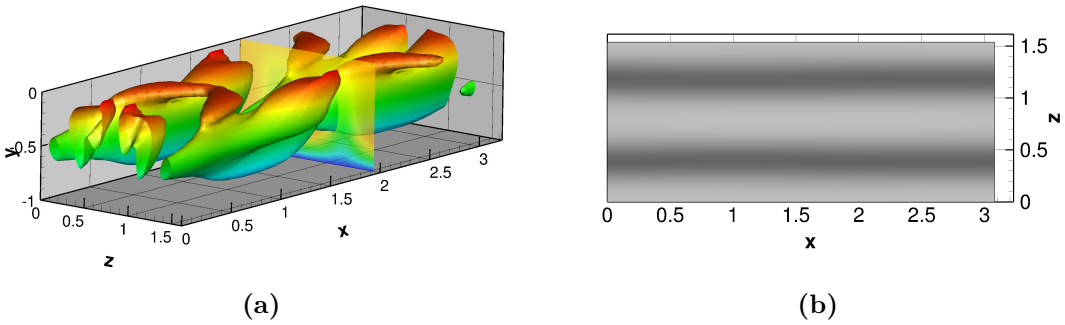

(a) **(b)**

Figure 4.8: (a) Vortical structure of S1LB at $Re = 3000$ (point **i**). Isosurface of $Q = 0.014$ is shown. (b) Streamwise velocity v_x at $y^+ = 20$.

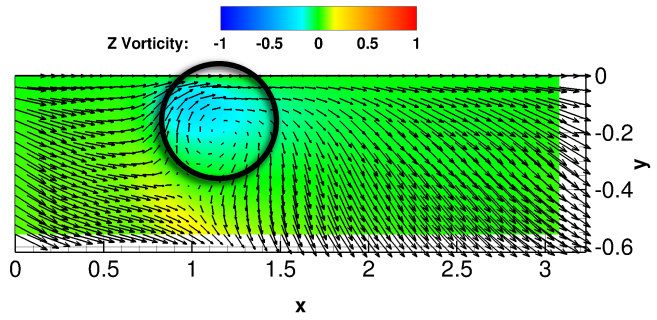

Figure 4.9: Contour of z-vorticity on the z-midplane with arrows indicating the velocity field in a frame moving at $v_x = 0.775$ for S1LB at $Re = 3000$. In this plot the region between $y = -0.6$ and $y = 0$ (the centerplane) is shown.

Figure 4.5 is, in a traveling reference frame, an equilibrium structure. We believe that the reason it was possible to find such a structure is the channel geometry and the corresponding centerplane symmetry; this keeps the hairpin from continually drifting away from the wall as occurs in a boundary layer – the channel geometry has allowed us to "trap" the hairpin structure, confining it to a finite distance from the wall and allowing it to propagate as a traveling wave. An interesting topic of future work would be to seek ECS with streamwise aligned, rather than staggered, hairpin-like vortices.

The above discussion has focused on the evolution of S1 from the bifurcation point

in the direction of increasing dissipation. For completeness, we show in Figures 4.8 and 4.9 the structure that evolves along the lower branch solution S1LB. Characteristic of lower branch solutions, the overall vortex and streak structure becomes much weaker with distance from the saddle-node bifurcation point, and while a z-oriented vortex structure also emerges on this branch, it is very weak, and not well-defined until higher Re than on the upper branch. This is why we have illustrated the structure at $Re = 3000$ rather than the value of 1800 that we used for the upper branch. Observe that that the Q value chosen for Fig. 4.8a is 0.014, much smaller than the value 0.072 used to visualize the upper branch (Figure 4.5a) and the waviness of the streaks shown in Fig. 4.8b is very weak – they are very nearly streamwise invariant.

An important issue is the relationship between ECS and turbulent dynamics. Figure 4.10 shows profiles of area-averaged mean velocity and Reynolds shear stress at $Re = 1800$ for the states indicated with red dots on Figure 4.2; these include solutions from both the P4 and S1 families. Also shown are profiles from turbulent trajectories obtained via direct numerical simulation (DNS) for the same domain and Reynolds number. Both S1UB and P4UB1 have mean velocity profiles that are fairly close to that of the turbulence, though the latter has inflectional kinks that are absent in S1UB. In inner units, the Reynolds shear stress for S1UB is in quantitative agreement with the turbulent result near the wall and yields very nearly the same peak position $y^+ \approx 25$. For $y^+ \gtrsim 20$, S1UB has slightly higher Reynolds shear stress than the turbulence. In outer units, the quantitative resemblance is not as strong, but is still reasonably good. In any case, S1UB more closely resembles the turbulence than do any of the other ECS reported here.

Another illustration of the relationship between ECS and turbulence is given in

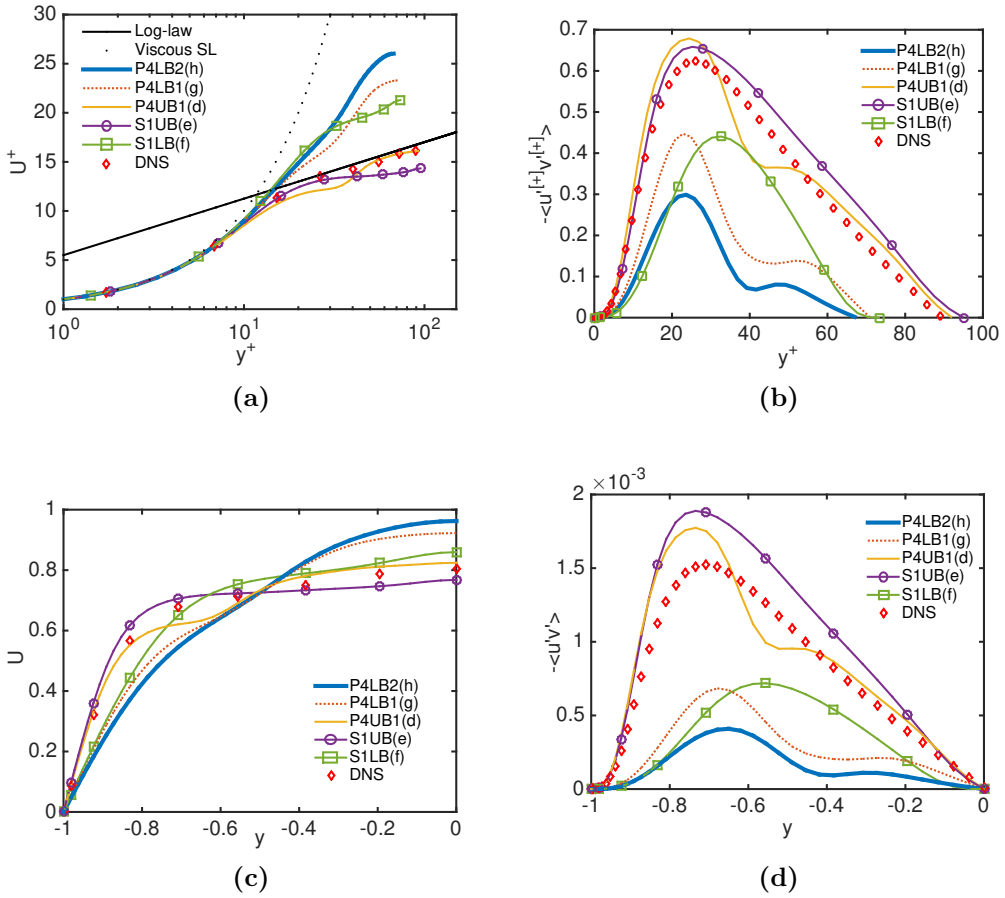

Figure 4.10: Mean profiles for ECS and turbulent flow (DNS) at $Re = 1800$: (a) Mean velocity in inner units, (b) Reynolds shear stress in inner units, (c) Mean velocity in outer units and (d) Reynolds shear stress in outer units. For the ECS, the parenthesized letter in the legend indicates the corresponding point on Figure 4.2.

Figure 4.11, which shows projections of ECS and trajectories onto selected variables: area-averaged wall shear rate, dissipation rate D and disturbance kinetic energy $KE = \frac{1}{2}||\boldsymbol{u} - \boldsymbol{u}_{\text{laminar}}||^2$. In this projection, all of the ECS plotted appear to be embedded in the same region of state space as the turbulent attractor. Also shown in yellow in Figure 4.11 is a trajectory starting from S1LB plus a random perturbation. It starts to approach P4LB2 before bursting towards the turbulent core. This observation points at a possible heteroclinic connection between the S1LB and P4LB2 and

at a role that hairpins may play in the transition to turbulence.

Finally, while hairpin structures are not prominent in DNS under the conditions considered here, they do arise occasionally, as seen in the simulation snapshot shown in Figure 4.11c.

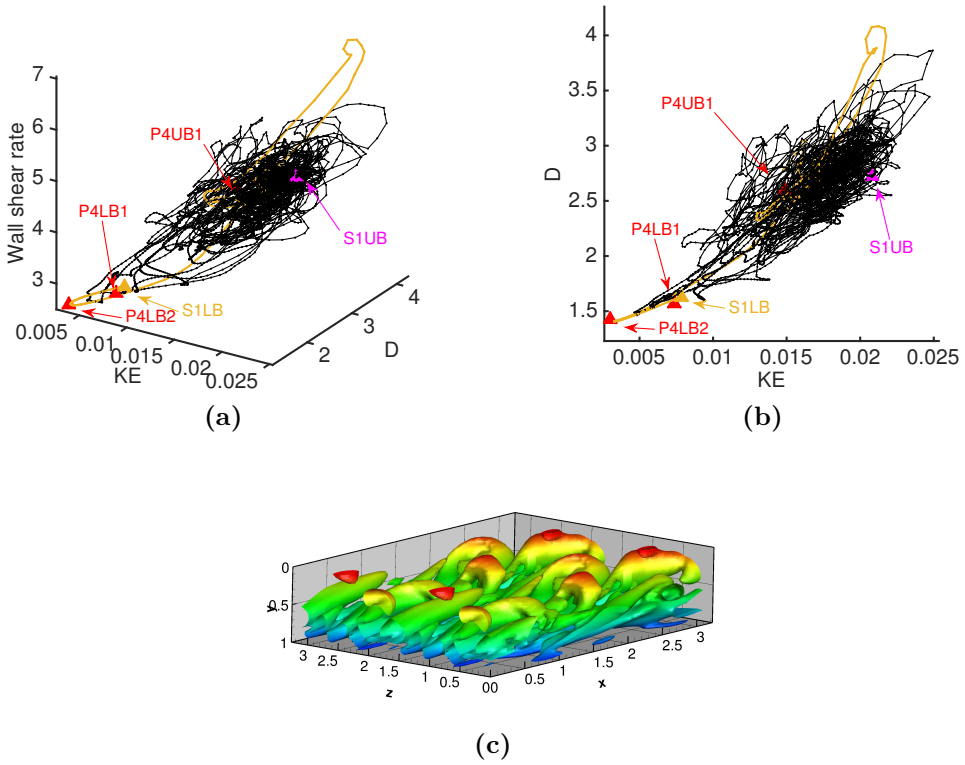

Figure 4.11: (a) State space visualization of DNS trajectories at $Re = 1800$, projected onto three dimensions: disturbance kinetic energy(KE), energy dissipation rate(D) and wall shear rate. The labelled symbols are computed ECS and the black lines are the DNS trajectories at $Re = 1800$. (b) 2D projection of (a). Also shown is a trajectory starting from S1LB (yellow). (c) Isosurface of $Q = 0.072$ at an instant during DNS at $Re = 1800$. Shown is the top half of the domain, rotated to be consistent with other figures. For clarity, two periods in z are shown.

4.4 Conclusion

Prior studies have created a catalogue of nonturbulent recurrent solutions to the Navier–Stokes equations – exact coherent states – that capture key features of near-wall turbulence, including streamwise vortices [Waleffe, 2001], bursts [Toh and Itano, 2003] and localized spots [Brand and Gibson, 2014] or puffs [Chantry *et al.*, 2014]. The present work adds an important entry to this catalogue. Hairpin vortices have long been observed within turbulent flows in various contexts, from boundary layer transition to fully-developed flows. Both the upper and lower branches of the S1 solution family reported here for the minimal channel flow geometry display a clear hairpin-like structure, with a spanwise-oriented head connected to quasistreamwise-oriented legs. Additionally, in the Reynolds number regime studied, the upper branch state has mean velocity and Reynolds shear-stress profiles that are quantitatively similar to the turbulent profiles in a channel of the same (minimal) dimensions.

The present results are of course obtained for a system that is highly constrained by symmetry and periodicity conditions. Nevertheless, the observations described here further strengthen the growing body of work connecting turbulent dynamics to simpler underlying state-space structures. By understanding the latter, we are increasingly gaining insight into the former.

Chapter 5

Critical layer structures and mechanisms in elastoinertial turbulence[a]

5.1 Introduction

As detailed in chapter 4, the dynamics of Newtonian turbulence is organized around coherent motions that are captured in ECS. In this chapter, we translate these ideas to identify prominent coherent motions in elastoinertial turbulence (EIT) by understanding the nature of transition to EIT close to the point where it first comes into existence. By doing so, we are able to gain a deeper understanding into the underlying mechanisms of EIT.

[a]This chapter includes content from: Shekar, A., McMullen, R. M., Wang, S-N., McKeon, B. J., and Graham, M. D. (2019). Critical-layer structures and mechanisms in elastoinertial turbulence. Phys. Rev. Lett. 122, 124503.

In Newtonian channel or pipe flow, transition to turbulence occurs by a so-called subcritical or "bypass" transition mechanism as flow rate, measured nondimensionally by Reynolds number, Re, increases: turbulence is initiated by finite-amplitude perturbations to the laminar flow profile, while the laminar flow remains linearly stable. This bypass transition to Newtonian turbulence has been attributed to the appearance of 3D ECS at finite amplitude. While channel flow exhibits a two-dimensional linear instability leading to so-called Tollmien-Schlichting (TS) waves, the critical Reynolds number $Re = 5772$ is much higher than that observed for transition, so these are not traditionally viewed as playing an important role in Newtonian transition.

For flowing polymer solutions under some conditions (low concentration, short polymer relaxation times), transition to turbulence occurs via the usual bypass transition. With further increase in Re, drag reduction sets in, and the flow eventually approaches the so-called maximum drag reduction (MDR) asymptote, an upper bound on the degree of drag reduction that is insensitive to the details of the fluid.

Under other conditions, flow transitions directly from laminar flow into the MDR regime, and can do so at a Reynolds number where the flow would remain laminar if Newtonian [Forame *et al.*, 1972, Hoyt, 1977, Choueiri *et al.*, 2018, Chandra *et al.*, 2018]. Recent experiments and simulations [Samanta *et al.*, 2013, Dubief *et al.*, 2013, Sid *et al.*, 2018] suggest that turbulence in this regime has structure very different from Newtonian, denoting it as "elastoinertial turbulence" (EIT). Choueiri *et al.* [Choueiri *et al.*, 2018] experimentally observed that at transitional Reynolds numbers and increasing polymer concentration, turbulence is first suppressed, leading to relaminarization, and then reinitiated with an EIT structure and a level of drag corresponding to MDR. Therefore, there are actually two distinct types of turbulence in

polymer solutions, one that is suppressed by viscoelasticity, and one that is promoted.

Here, we report computations and analysis that elucidate the mechanisms underlying EIT. We show that EIT at low *Re* has highly localized polymer stress fluctuations. Surprisingly, these strongly resemble linear Tollmien-Schlichting modes as well as the most strongly amplified fluctuations from the laminar state. Furthermore, the kinematics of self-sustained nonlinear TS waves generate sheetlike structures in the stress field similar to those observed in EIT. The resemblance of structures at EIT to these Newtonian phenomena may shed light on the observed near-universality of the MDR regime with regard to polymer properties.

5.2 Formulation

We consider pressure-driven channel flow with constant mass flux. The x, y and z axes are aligned with the streamwise (overall flow), wall-normal and spanwise directions, respectively. Lengths are scaled by the half channel height l so the dimensionless channel height $L_y = 2$. The domain is periodic in x and z with periods L_x and L_z. Velocity $\boldsymbol{v}$ is scaled with the Newtonian laminar centerline velocity U; time t with l/U, and pressure p with ρU^2, where ρ is the fluid density. The polymer stress tensor $\boldsymbol{\tau}_p$ is related to the polymer conformation tensor $\boldsymbol{\alpha}$ (second moment of the probability distribution for the polymer end-to-end vector) through the FENE-P constitutive relation, which models each polymer molecule as a pair of beads connected by a nonlinear spring with maximum extensibility b. We solve the momentum, continuity

and FENE-P equations:

$$\frac{\partial \boldsymbol{v}}{\partial t} + \boldsymbol{v}\cdot\boldsymbol{\nabla}\boldsymbol{v} = -\boldsymbol{\nabla}p + \frac{\beta}{Re}\nabla^2\boldsymbol{v} + \frac{(1-\beta)}{ReWi}\left(\boldsymbol{\nabla}\cdot\boldsymbol{\tau}_{\mathrm{p}}\right), \tag{5.1}$$

$$\boldsymbol{\nabla}\cdot\boldsymbol{v} = 0, \tag{5.2}$$

$$\boldsymbol{\tau}_p = \frac{\boldsymbol{\alpha}}{1-\frac{\mathrm{tr}(\boldsymbol{\alpha})}{b}} - \boldsymbol{I}, \tag{5.3}$$

$$\frac{\partial \boldsymbol{\alpha}}{\partial t} + \boldsymbol{v}\cdot\boldsymbol{\nabla}\boldsymbol{\alpha} - \boldsymbol{\alpha}\cdot\boldsymbol{\nabla}\boldsymbol{v} - (\boldsymbol{\alpha}\cdot\boldsymbol{\nabla}\boldsymbol{v})^{\mathrm{T}} = \frac{-1}{Wi}\boldsymbol{\tau}_p. \tag{5.4}$$

Here $Re = \rho U l/(\eta_{\mathrm{s}} + \eta_{\mathrm{p}})$, where η_s and η_p are the solvent and polymer contributions to the zero-shear rate viscosity. The viscosity ratio $\beta = \eta_{\mathrm{s}}/(\eta_{\mathrm{s}} + \eta_{\mathrm{p}})$; polymer concentration is proportional to $1-\beta$. We fix $\beta = 0.97$ and $b = 6400$. The Weissenberg number $Wi = \lambda U/l$, where λ is the polymer relaxation time, measures the ratio between the relaxation time for the polymer and the shear time scale for the flow. Below we report values of friction factor $f = \frac{2\tau_w}{\rho U^2}$, where τ_w is time- and area -averaged wall shear stress. This is a nondimensional measure of pressure drop or drag. Its value in laminar flow is denoted f_{lam}.

For the nonlinear direct numerical simulations (DNS) described below, a finite difference scheme and a fractional time step method are adopted for integrating the Navier-Stokes equation. Second-order Adams-Bashforth and Crank-Nicolson methods are used for convection and diffusion terms, respectively. The FENE-P equation is discretized using a high resolution central difference scheme [Kurganov and Tadmor, 2000, Vaithianathan *et al.*, 2006, Dallas *et al.*, 2010]. No artificial diffusion is applied. For the three-dimensional (3D) simulations, $(L_x, L_y, L_z) = (10, 2, 5)$; these were chosen to match Samanta *et al.* [2013]. Typical resolution for the 3D runs at EIT is $(N_x, N_y, N_z) = (189, 150, 189)$. For the 2D runs at $Re = 3000$, $N_y = 302$ is used. For

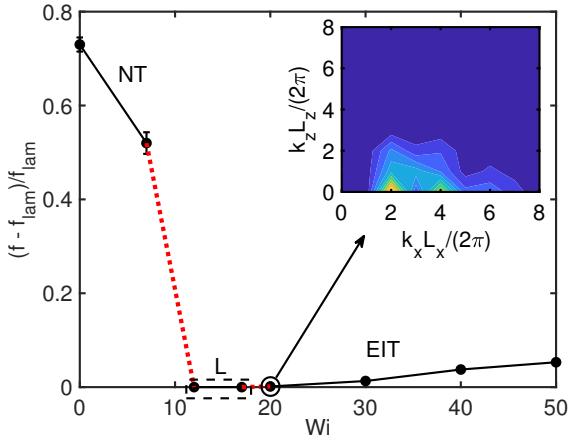

Figure 5.1: Scaled friction factor vs. Wi at $Re = 1500$. Abbreviations 'NT', 'L' and 'EIT' stand for Newtonian-like turbulence, laminar and elastoinertial turbulence, respectively. In most cases, the error bars are smaller than the symbols. Red dotted lines indicate the intervals of Wi in which the NT solution loses existence and the EIT solution comes into existence, respectively, as Wi increases. Inset shows the spatial spectrum of the wall normal velocity at $y = 0$ for $Wi = 20$. Here, x- and z-wavenumbers k_x and k_z are reported in scaled form, as $k_x L_x/2\pi$ and $k_z L_z/2\pi$. For inset, low is blue, high is yellow.

the linear analyses, Eqs. 5.2-5.4, linearized around the laminar solution and Fourier-transformed in x z, and t, are discretized in y with a Chebyshev pseudospectral method. Typically, about 200 Chebyshev polynomials are sufficient for the resolvent calculations, whereas as many as 400 are required for the TS eigenmode. The norm used in the resolvent calculations is the sum of the kinetic energy and a measure of the conformation tensor perturbation magnitude that is consistent with the non-Euclidean geometry of positive-definite tensors [Hameduddin *et al.*, 2019].

5.3 Results and discussion

Nonlinear simulation results: Fig. 5.1 illustrates 3D DNS results for scaled friction factor $(f - f_{\text{lam}})/f_{\text{lam}}$ vs. Weissenberg number Wi at $Re = 1500$. At low but increasing Wi, the flow is turbulent, with f decreasing, indicating that the drag is reduced from the Newtonian value. In this regime, which we denote NT, the turbu-

lence displays a streamwise vortex structure typical of Newtonian turbulence. With a further increase in Wi, however, $f - f_{\text{lam}}$ drops to zero – the flow relaminarizes, as the NT regime loses existence. (At this Re and all Wi considered here, the laminar state is linearly stable.) At still higher Wi, the flow, if seeded with a sufficiently energetic initial condition, becomes turbulent again, with a very low value of $f - f_{\text{lam}}$ (consistent with experimental observations of Choueiri *et al.* [2018] in pipe flow) and a very different structure: i.e. a new kind of turbulence comes into existence. In this regime the flow structure corresponds to EIT as described by Samanta *et al.* [2013], Sid *et al.* [2018]; we further analyze this structure below. In short, as Wi increases from zero, the self-sustaining mechanism of Newtonian turbulence is weakened by viscoelasticity, resulting in loss of existence of the NT state. As Wi increases further, a new nonlinear self-sustaining (i.e. bypass transition) mechanism comes into play, resulting in EIT.

We now focus on the flow structure in the EIT regime. The inset in Fig. 5.1 shows a spatial spectrum of the wall normal velocity at $y = 0$ (the channel centerplane), i.e., $|v(k_x, 0, k_z)|$. The centerplane is chosen because it yields the cleanest spectra. In the EIT regime, there is very strong spectral content when $k_z = 0$, indicating the importance of 2D mechanisms in the dynamics. Indeed, Sid *et al.* [2018] reports that EIT can arise in 2D simulations. Figure 5.2a shows a slice at $z = 2.5$ of the fluctuating wall normal velocity, v', and fluctuating xx-component of the polymer conformation tensor, α'_{xx}. Observe that α'_{xx} is strongly localized near $y = \pm 0.7 - 0.8$. While tilted sheets of polymer stretch fluctuations have already been noted as characteristic of EIT [Samanta *et al.*, 2013], the strong localization has not been previously observed, perhaps because prior results have been at higher Re and Wi,

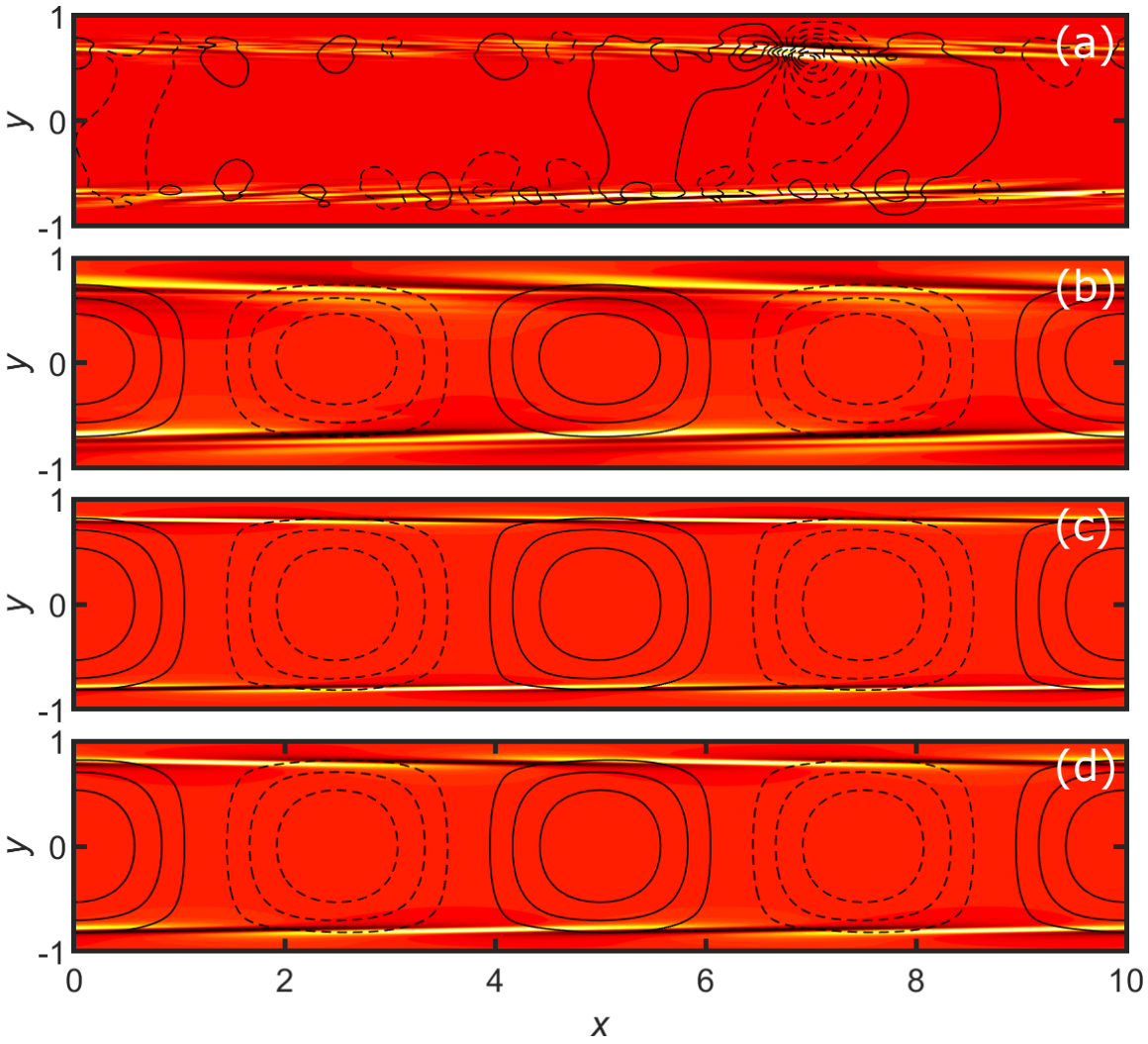

Figure 5.2: (a) Snapshot of v' (line contours) and α'_{xx} (filled contours) from 3D nonlinear DNS at $Re = 1500$, $Wi = 20$, where $'$ denotes fluctuations. (b) Phase-matched average $(k_x L_x/2\pi, k_z L_z/2\pi) = (2, 0)$ structures from 3D DNS. (c) Structure of the TS mode at $Re = 1500$, $Wi = 20$, and the same wavenumbers as in (b). (d) Structure of the most strongly amplified resolvent mode at $Re = 1500$, $Wi = 20$, the same wavenumbers as in (b), and $c = 0.37$. In all plots, contour levels are symmetric about zero. For v' dashed - negative, solid - positive. For α'_{xx} black - negative, red - zero and yellow - positive.

i.e. further from the point at which EIT comes into existence. Fig. 5.2b shows the dominant $(k_x L_x/2\pi, k_z L_z/2\pi) = (2, 0)$ component of the $Wi = 20$ results, phase-matched and averaged over many snapshots. Results for higher k_x are very similar, exhibiting strong localization of stress fluctuations in the same narrow bands, as well as velocity fluctuations that span the channel height.

Linear analyses: To shed light on the origin of the highly localized large stress fluctuations, we now consider the evolution of infinitesimal perturbations to the laminar state with given wavenumbers k_x, k_z. Two approaches are used. The first is classical linear stability analysis, in which solutions of the form $\phi(y) \exp[i(k_x x + k_z z - k_x c t)]$ are sought, resulting in an eigenvalue problem for the complex wavespeed c. If any $c_i > 0$, then the laminar state is linearly unstable – infinitesimal perturbations will grow exponentially. If all $c_i < 0$, the flow is linearly stable. The second approach is to determine the linear response of the laminar flow to external forcing with given real frequency ω using the resolvent operator (frequency-space transfer function) of the linearized equations [Schmid, 2007, McKeon and Sharma, 2010b]. In both analyses, the concept of *critical layers*, i.e., wall-normal positions where the fluid velocity equals the wavespeed of an eigenmode or resolvent mode, is important. While some recent studies suggest the importance of critical layer mechanisms in viscoelastic shear flows [Page and Zaki, 2015, Lee and Zaki, 2017, Haward *et al.*, 2018, Hameduddin *et al.*, 2019], they do not make as direct a connection to EIT as we illustrate here.

Figure 5.3a shows the result of linear stability analysis (the eigenvalues c) for $Wi = 20$, $k_x L_x/2\pi = 2$, $k_z = 0$, the wavenumber corresponding to the dominant structures observed in the nonlinear simulations. All eigenvalues have $c_i < 0$ – the

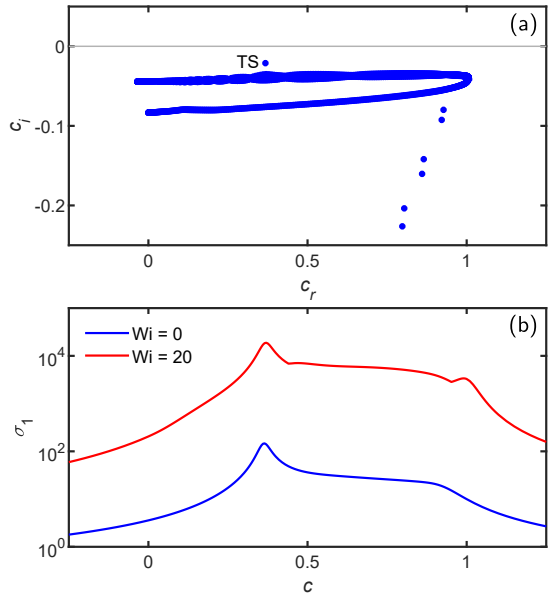

Figure 5.3: Eigenvalue spectrum for $(k_x L_x/2\pi, k_z L_z/2\pi) = (2, 0)$ with $Wi = 20$ and $Re = 1500$. The eigenvalue labeled 'TS' corresponds to the TS mode. (b) Leading singular value of the resolvent operator for $Wi = 0$ and $Wi = 20$, plotted on a logarithmic scale.

laminar flow is linearly stable.

Of note is the mode labeled 'TS', the viscoelastic continuation of the classical Tollmien-Schlichting mode [Drazin and Reid, 2004]. Viscoelasticity has only a weak effect on the TS eigenvalue, which changes from $c = 0.362 - 0.019i$ to $c = 0.368 - 0.022i$ between $Wi = 0$ and $Wi = 20$ [Zhang *et al.*, 2013]. Despite the small change in c, the conformation tensor disturbance depends very strongly on Wi; the peak value of α'_{xx} grows from zero at $Wi = 0$ to $\sim 10^5$ times the peak value of u' at $Wi = 20$.

The structure of this eigenmode is shown for $Wi = 20$ in Fig. 5.2c. In the Newtonian case, the disturbance velocity field is a train of spanwise-oriented vortices that span the entire channel; this structure is only weakly modified even at high Wi. The polymer stress disturbance behaves very differently: at $Wi = 20$ it consists of highly inclined sheets that are extremely localized around the critical layers

$y = \pm 0.79$ for the TS wavespeed of $c_r \approx 0.37$. Comparison with Figs. 5.2a and 5.2b shows a strong similarity between the eigenmode and the tilted sheetlike structures that are the hallmark of EIT, with the resemblance between the TS mode and the $(k_x L_x/2\pi, k_z L_z/2\pi) = (2, 0)$ structure from the DNS in Fig. 5.2b being particularly striking. Specifically, note that for the TS mode, Fig. 5.2c, v' and α'_{xx} are even and odd, respectively, with respect to $y = 0$, while in Fig. 5.2b and the corresponding results at higher wavenumbers, these symmetries hold to a good approximation.

Despite the fact that the TS mode ultimately decays, the non-normal character of the linearized Navier-Stokes operator can lead to significant disturbance growth at short times or significant amplification of harmonic-in-time disturbances [Schmid, 2007]. Thus it is therefore possible for small disturbances to be sufficiently amplified that nonlinear effects become significant. We now quantify this amplification by computing the largest singular value σ_1 of the resolvent operator. Figure 5.3b shows results for $Wi = 0$ and $Wi = 20$ in the same range of (real) wavespeeds $c = \omega/k_x$ depicted in Figure 5.3a. The amplification increases dramatically with Wi, with the values at $Wi = 20$ being $\sim 10^2$ times those for $Wi = 0$; this is consistent with the drastic increase in the conformation tensor disturbance amplitude already discussed for the TS mode. In both cases, the maximum amplification occurs for $c \approx 0.37$, which coincides with the wavespeed for the TS mode, indicating that the most-amplified disturbance is closely linked to the TS wave. Figure 5.2d shows the leading resolvent mode, which is indeed almost identical to the TS eigenmode in Figure 5.2c. This result provides additional strong evidence that the structures observed in EIT are closely related to those in viscoelasticity-modified TS waves.

It was recently shown that viscoelastic pipe flow of an Oldroyd-B fluid ($b \to \infty$)

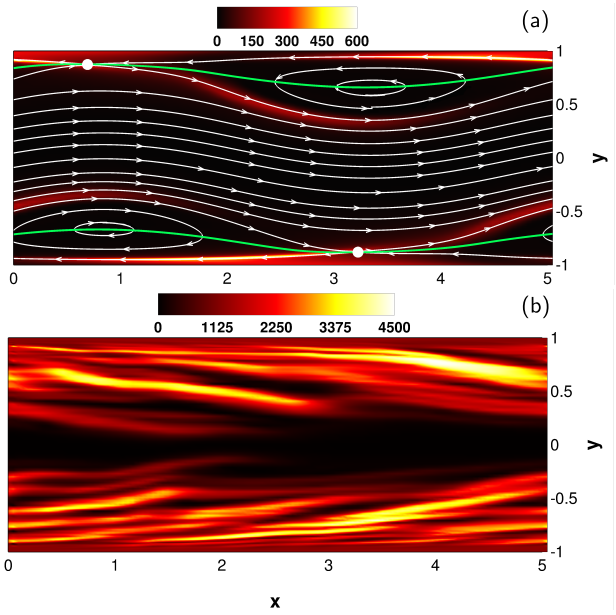

Figure 5.4: (a) Structure of nonlinear self-sustaining TS wave at $Re = 3000$, $Wi = 3$. White streamlines, shown in a reference frame moving with the wavespeed $c = 0.39$, are superimposed on color contours of α_{xx}. Green lines indicate the instantaneous critical layer positions, and white dots indicate the locations of hyperbolic stagnation points. (b) Snapshot of α_{xx} contours from 2D EIT at $Re = 3000$, $Wi = 15$.

can be linearly unstable to center-localized modes with wavespeed $c_r \approx 1$ [Garg *et al.*, 2018]. We estimate that for the present parameter values, this mode only becomes relevant for very high Wi. Furthermore, center-localized structures are not observed in the simulations of EIT, so we do not consider them relevant here.

Self-sustained viscoelastic Tollmien-Schlichting waves: Here we elaborate on the potential connection between TS-like structure and EIT, presenting results for nonlinear viscoelastic TS waves, i.e. self-sustained traveling wave solutions of the full nonlinear governing equations, illustrating the role of the critical layer kinematics in generating localized sheetlike regions of high polymer stretching like those observed in EIT.

The strong peak in the EIT spectrum seen in Figure 5.1 corresponds to a wave-

length of 5, so here we report computations of nonlinear TS wave in a 2D domain with this length. The upper branch of this solution family is linearly stable in 2D at $Re = 3000$ [Jiménez, 1990, Mellibovsky and Meseguer, 2015, Herbert, 1979] and easily captured with DNS using the linear TS mode as the initial condition. In Newtonian flow, the solution family exists at this wavelength down to $Re \approx 2800$. We continue the Newtonian solution at $Re = 3000$ to the parameters of interest ($\beta = 0.97$ and $b = 6400$) at $Wi = 0.1$, then increase Wi to study the effect of viscoelasticity. Hameduddin et al. [Hameduddin *et al.*, 2019] have computed nonlinear viscoelastic TS waves in the regime $Re > 5772$ and noted the role the critical layer plays in polymer stretching at high Wi, but have not reported the observations described below.

On increasing Wi, the self-sustained nonlinear viscoelastic TS wave at $Re = 3000$ develops sheets of high polymer stretch resembling near wall structures seen at EIT. Figure 6.1 illustrates this point with a plot of α_{xx} at $Wi = 3$. The source of this stretching is closely tied to the critical layer structure of the TS wave velocity field. Critical layers have long been-known to exhibit a so-called Kelvin cat's-eye streamline structure [Drazin and Reid, 2004] – indeed, the velocity fields for the flows shown in Figures 5.2c and 5.2d display this feature. With regard to viscoelasticity, the cat's-eye structure is important because it contains hyperbolic stagnation points: polymers are strongly stretched as they approach such points and leave along their unstable manifolds. This phenomenon is clearly seen in Figure 6.1a; shown in white are streamlines in the reference frame traveling with the speed of the wave $c = 0.39$, and in green is the instantaneous critical layer position, i.e. where $v_x = c$. A hyperbolic stagnation point (white dot) exists at $x = 3.22, y = -0.87$. The high polymer stretching follows the streamlines along the unstable directions associated

with this point, giving rise to an arched sheetlike structure. By symmetry, identical structures exist in the top half of the channel. For comparison, Figure 6.1b shows α_{xx} for 2D EIT at $Re = 3000$, $Wi = 15$. This takes the form of tilted sheets of high polymer stretch starting out at locations close to the walls, and in fact reasonably close to the positions $y = \pm 0.87$ of the stagnation points in the nonlinear TS wave at $Wi = 3$. This similarity in structures suggests a role for TS wave-like critical layer mechanisms at EIT. Indeed, these results suggest that the nonlinear TS wave solution branch may be directly connected in parameter space to EIT. We do not find this to be the case at $Re = 3000$; the TS branch loses existence above $Wi \approx 4$ and the EIT branch loses existence below $Wi \approx 13$. Nevertheless, when using the EIT result at $Wi = 13$ as the initial condition for a simulation at $Wi = 12$, EIT persists transiently for hundreds of time units and the last remaining structure observed as the flow decays to laminar closely resembles Figs. 2b-d.

5.4 Conclusion

Elastoinertial turbulence at low Re has strongly localized stress fluctuations, suggesting the importance of critical layer mechanisms in its origin. These fluctuations strongly resemble the most slowly decaying structures from linear stability analysis, as well as the most strongly amplified disturbances as determined by resolvent analysis of the linearized equations. Furthermore, the Kelvin cat's eye kinematics found in the critical layer region of self-sustained nonlinear TS waves generate sheetlike structures in the stress field that resemble those observed in EIT. Taken together, these results suggest that, at least in the parameter range considered here, the bypass

transition leading to EIT is mediated by nonlinear amplification and self-sustenance of perturbations that generate TS-wave-like flow structures.

Chapter 6

Self-sustained elastoinertial Tollmien–Schlichting waves[a]

6.1 Introduction

In the last chapter, we described observations of a reentrant transition to EIT in simulations of channel flow with increasing Weissenberg number, Wi, the ratio between the polymer relaxation time scale and the shear time scale. Further, we saw that close to its inception, EIT exhibits localized polymer stress fluctuations that bear strong resemblance to critical layer structures predicted by linear analyses, i.e., sheet-like fluctuations localized at wall-normal locations where the disturbance wavespeed equals the base flow velocity. In particular, they demonstrated that the fluctuation structure corresponding to the dominant spectral content strongly resembles the vis-

[a]This chapter includes content from: Shekar, A., McMullen, R. M., McKeon, B. J., and Graham, M. D. (2020). Self-sustained elastoinertial Tollmien–Schlichting waves. Journal of Fluid Mechanics 897, A3.

coelastic extension of the linear Tollmien-Schlichting (TS) wave. This is perhaps a surprising result, as the flow in the parameter regime considered is linearly stable, and in Newtonian turbulence, the TS mode plays a very limited role. Some light is shed on this issue through resolvent analysis, i.e., determination of the response of the linearized dynamics to harmonic-in-time disturbances, which shows that the linear TS mode becomes highly amplified in the presence of viscoelasticity. This strong amplification implies that even very weak disturbances may be sufficient to trigger the nonlinear effects necessary to sustain EIT.

We note that similar structures have been observed by other researchers in different contexts. Page and Zaki [2015] analyzed the evolution of vortical perturbations in 2D viscoelastic simple shear flow. Their analysis reveals a viscoelastic analogue of the Newtonian Orr mechanism. This "reverse-Orr" mechanism generates tilted sheets of polymer stress fluctuations resembling those seen at EIT and thus may play some role in this phenomenon.

Because prior work on elastoinertial turbulence reveals structures similar to those seen in the linear Tollmien-Schliching mode, the present work focuses on Tollmien-Schlichting waves, but in the fully nonlinear context of self-sustained solutions in the channel flow geometry. (In the parameter regime here, the laminar flow is always linearly stable.) After introducing the formulation and computational methods, we show how the Newtonian nonlinear TS wave branch is modified by viscoelasticity, resulting in its disappearance as Wi increases. At still higher Wi, however, we demonstrate the onset of a new, viscoelasticity-driven, nonlinear solution branch that strongly resembles the linear Tollmien-Schlichting mode, and illustrate how it is related to the TS mode of linear theory and to elastoinertial turbulence.

6.2 Formulation

This study focuses on two-dimensional pressure-driven channel flow with constant mass flux. The x and y axes are aligned with the streamwise and wall-normal directions, respectively. Lengths are scaled by the half channel height l, so the dimensionless channel height $L_y = 2$. The domain is periodic in x with length L_x. Velocity $\boldsymbol{v}$ is scaled with the Newtonian laminar centerline velocity U; time t with l/U, and pressure p with ρU^2, where ρ is the fluid density. The polymer stress tensor $\boldsymbol{\tau}_p$ is related to the polymer conformation tensor $\boldsymbol{\alpha}$ through the FENE-P constitutive relation, which models each polymer molecule as a pair of beads connected by a nonlinear spring with maximum extensibility b.

We solve the momentum, continuity and FENE-P equations:

$$\frac{\partial \boldsymbol{v}}{\partial t} + \boldsymbol{v}\cdot\boldsymbol{\nabla}\boldsymbol{v} = -\boldsymbol{\nabla}p + \frac{\beta}{Re}\nabla^2\boldsymbol{v} + \frac{(1-\beta)}{Re\,Wi}\left(\boldsymbol{\nabla}\cdot\boldsymbol{\tau}_{\mathrm{p}}\right), \tag{6.1}$$

$$\boldsymbol{\nabla}\cdot\boldsymbol{v} = 0, \tag{6.2}$$

$$\boldsymbol{\tau}_p = \frac{\boldsymbol{\alpha}}{1-\frac{\mathrm{tr}(\boldsymbol{\alpha})}{b}} - \boldsymbol{I}, \tag{6.3}$$

$$\frac{\partial \boldsymbol{\alpha}}{\partial t} + \boldsymbol{v}\cdot\boldsymbol{\nabla}\boldsymbol{\alpha} - \boldsymbol{\alpha}\cdot\boldsymbol{\nabla}\boldsymbol{v} - (\boldsymbol{\alpha}\cdot\boldsymbol{\nabla}\boldsymbol{v})^{\mathrm{T}} = \frac{-1}{Wi}\boldsymbol{\tau}_p. \tag{6.4}$$

Here $Re = \rho U l/(\eta_{\mathrm{s}} + \eta_{\mathrm{p}})$, where η_s and η_p are the solvent and polymer contributions to the zero-shear rate viscosity. The viscosity ratio $\beta = \eta_{\mathrm{s}}/(\eta_{\mathrm{s}} + \eta_{\mathrm{p}})$. We fix $\beta = 0.97$ and $b = 6400$. Since $1-\beta$ is proportional to polymer concentration and b to the number of monomer units, this parameter set corresponds to a dilute solution of a high molecular weight polymer. The Weissenberg number $Wi = \lambda U/l$, where λ is the

polymer relaxation time.

For the nonlinear direct numerical simulations (DNS) described below, a finite difference scheme and a fractional time step method are adopted for integrating the Navier-Stokes equation. Second-order Adams-Bashforth and Crank-Nicolson methods are used for convection and diffusion terms, respectively. The FENE-P equation is discretized using a high resolution central difference scheme [Kurganov and Tadmor, 2000, Vaithianathan *et al.*, 2006, Dallas *et al.*, 2010] that guarantees positive definiteness of the polymer conformation tensor without the need for any artificial diffusion. In any case, the nonlinear solution branch on which we focus in this manuscript displays weak fluctuations far from the limit of positive definiteness even at the highest Wi of existence. A typical resolution for the following results is $(N_x, N_y) = (79, 402)$. This resolution used was based on mesh convergence results at $Wi = 45$. When the resolution was increased to $(N_x, N_y) = (131, 602)$, the mean polymer stretch deviations from the laminar base state change by less than 1 percent.

We also consider the linearized evolution of infinitesimal perturbations to the laminar state with given streamwise wavenumber k. Two approaches are used. The first is classical linear stability analysis, in which solutions of the form $\hat{\boldsymbol{\phi}}(y) \exp[ik(x - ct)]$ are sought, resulting in an eigenvalue problem for the complex wavespeed c at a given k. In the present study, $\hat{}$ always indicates deviation from the laminar state. If all $c_i < 0$, which is the case for all conditions considered in the present study, the flow is linearly stable. A linearized version of the DNS code was also developed using the numerical schemes described above. Results were validated against linear stability analysis and agreement to three significant digits was obtained for the value of c for the viscoelastic TS mode at the parameters of interest.

The second linear approach used here determines the linear response of the laminar flow to external forcing with given wavenumber k and frequency ω using the resolvent operator of the linearized equations [Schmid, 2007, McKeon and Sharma, 2010a]. The norm used in the resolvent calculations is

$$\|\hat{\boldsymbol{\phi}}\|_{\boldsymbol{A}}^2 = \int_{-1}^{1} \left[\hat{\boldsymbol{v}}^*\hat{\boldsymbol{v}} + \mathrm{tr}\Big(\boldsymbol{A}^{-1}\hat{\boldsymbol{\alpha}}^*\boldsymbol{A}^{-1}\hat{\boldsymbol{\alpha}}\Big)\right] \mathrm{d}y, \tag{6.5}$$

where $\boldsymbol{A}$ is the conformation tensor in the laminar state. The second term provides a measure of the conformation tensor perturbation magnitude that is motivated by the non-Euclidean geometry of positive-definite tensors [Hameduddin *et al.*, 2019]. For both the linear stability and resolvent analyses, the equations are discretized with a Chebyshev pseudospectral method using 401 Chebyshev polynomials. This number was arrived at by ensuring convergence of the TS eigenvalue.

6.3 Results and discussion

6.3.1 Origin of Newtonian and viscoelastic nonlinear Tollmien-Schlichting attractors

In Newtonian flow, a family of nonlinear Tollmien-Schlichting waves bifurcates subcritically from the laminar branch at $Re \approx 5772$ with $L_x \approx 2\pi/1.02 \approx 6.15$. The lower limit of the parameter regime for which this solution family exists is $Re \approx 2800, L_x \approx 2\pi/1.3 \approx 4.83$ [Jiménez, 1990]. Furthermore, in prior work on elastoinertial turbulence [Shekar *et al.*, 2019], as well as more recent simulations in long two-dimensional domains, a strong peak in the spatial spectrum is found at $L_x \approx 5$. Based on these

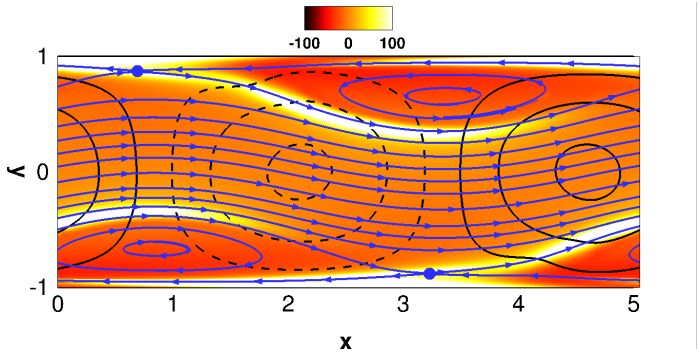

Figure 6.1: Structure of NNTSA at $Re = 3000$, $Wi = 3$. Streamlines (blue) in a reference frame moving at the wave speed $c = 0.39$ are superimposed on color contours of $\hat{\alpha}_{xx}$ where $\hat{}$ denotes deviations from the laminar state. Blue dots indicate the locations of hyperbolic stagnation points (in the traveling frame). Black contour lines of $\hat{v}$ are also shown. For $\hat{v}$, dashed = negative and solid = positive.

observations, all of the results presented in this study will be at $Re = 3000, L_x = 5$. (At $L_x = 5$, Newtonian channel flow is linearly stable at all Re.) In the Newtonian limit at these parameters, there are upper and lower branch solutions (which merge in a saddle-node bifurcation as Re is lowered); the upper branch traveling wave solution is linearly stable with respect to two-dimensional perturbations and is thus easily computed via DNS. We call this solution branch, including its viscoelastic extension, the Newtonian Nonlinear Tollmien-Schlichting attractor (NNTSA). (The word "attractor" is chosen rather than "wave" because, depending on parameters one can observe a pure traveling wave state or one with periodic or nonperiodic modulations.)

On increasing Wi, the self-sustained nonlinear viscoelastic TS wave at $Re = 3000$ develops sheets of high polymer stretch that start out from near the wall. These observations are evidence of the capability of nonlinear TS critical layer mechanisms in generating sheets of polymer stretch. Figure 6.1 illustrates this point with a snapshot of $\hat{\alpha}_{xx}$ on the NNTSA branch at $Wi = 3$. The sheets originate in the nonlinear Kelvin cat's eye kinematics of TS waves at finite amplitude, as detailed in Shekar *et al.* [2019]. The NNTSA continues to display wall normal velocity fluctuations that

extend across the channel centerline – a signature of TS kinematics. Some of the observations made in Shekar *et al.* [2019] are repeated here for completeness, as they form the background for the new results of the present study.

At the parameters chosen, the solution branch originating in the self-sustained Newtonian TS wave bifurcates to a periodic orbit at $Wi \approx 3.5$ (cf. Lee and Zaki [2017]) before turning back into a traveling wave and losing existence beyond $Wi = 3.875$, evidently in a saddle-node bifurcation yielding a lower branch TS wave solution that becomes the Newtonian solution as $Wi \to 0$. Consistent with a saddle-node bifurcation, if the solution at $Wi = 3.875$ is used as an initial condition for a simulation at slightly higher Wi, the flow laminarizes. This bifurcation scenario is shown on Fig. 6.2a in terms of average wall shear rate vs. Wi. The unstable lower branch (dashed blue) was found using edge tracking (Zammert and Eckhardt [2014]) between NNTSA and laminar solutions at a given Wi. A bisection technique was used to arrive at arbitrarily close initial conditions that are on either side of the edge. DNS trajectories starting from such points stay on the edge for a while before diverging to NNTSA and laminar.

As shown in Shekar *et al.* [2019], if Wi is large, sufficiently energetic initial conditions lead to 2D EIT. Fig. 6.2(a) also shows the mean wall shear rate for the EIT solution branch, which loses existence at finite amplitude when $Wi \lesssim 13$. The bifurcation underlying this transition is presumably also of saddle-node form.

The central observation of the present paper arises from considering what happens just below the onset of the EIT regime at $Wi \approx 13$. We do this by using a velocity and stress field from EIT at $Wi = 13$ as an initial condition for a run at $Wi = 12$. This initial condition persists as a slowly decaying form of EIT for hundreds of

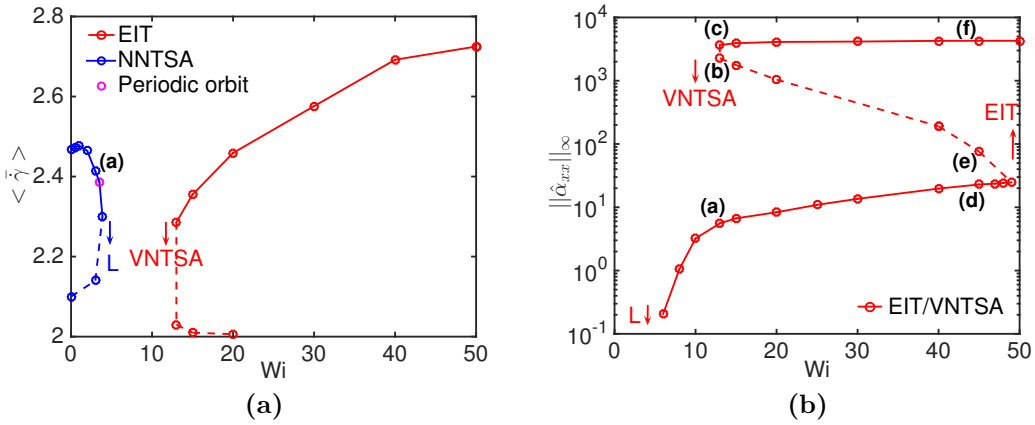

Figure 6.2: (a) Bifurcation diagram showing the evolution of the space and time-averaged wall shear rate with Wi for the 2D nonlinear NNTSA and EIT branches at $Re = 3000, L_x = 5$. Point (a) corresponds to the structure shown in Figure 6.1. Labels 'L' and 'VNTSA' indicate that initial conditions starting at the arrows evolve to laminar or VNTSA states, respectively. (b) Bifurcation diagram of the L_∞-norm of $\hat{\alpha}_{xx}$ with Wi for VNTSA and EIT. Points (a)-(f) correspond to structures shown later in Figure 6.6. The label 'EIT' indicates that initial conditions evolve to EIT. In both plots, dashed lines correspond to the unstable solution branches obtained from edge tracking.

time units, consistent with behavior just beyond a saddle-node bifurcation. As time increases further, the structure continues to decay, but does not ultimately reach the laminar state. Instead, it evolves to a nontrivial attractor state that is very nearly a traveling wave, and in particular strongly resembles the linear TS mode at these parameters. We call this new state the viscoelastic nonlinear Tollmien-Schlichting attractor (VNTSA).

6.3.2 Viscoelastic nonlinear Tollmien-Schlichting attractor

To elaborate on the relationship between the VNTSA and the linear TS mode, we describe results at $Re = 3000, Wi = 13, L_x = 5$, i.e. close to the point where the 2D EIT branch first comes into existence as shown in the bifurcation diagram (Figure 6.2a). EIT and the VNTSA are coexisting attractors at these parameter values. Figure 6.3 shows the evolution of the L_∞ norm of $\hat{\alpha}_{xx}$ starting from an

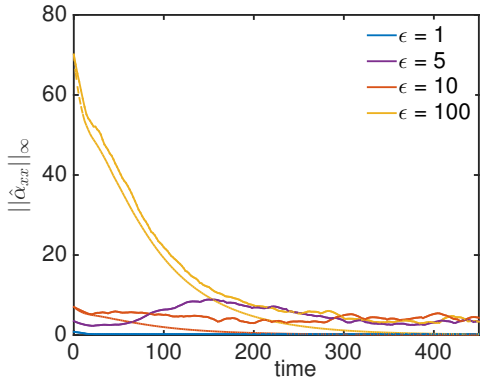

Figure 6.3: Time evolution of the L_∞-norm of $\hat{\alpha}_{xx}$ for $Re = 3000$, $Wi = 13$, $L_x = 5$, starting from an initial condition of laminar state + $\epsilon \times$ TS-mode. Dashed lines correspond to linearized runs starting from the same initial conditions for $\epsilon = 10$ and 100.

initial condition consisting of the laminar state plus some amplitude ϵ of the linear TS mode for this parameter set. This mode, with $\epsilon = 1$, is shown in Figure 6.4a. The structure of the velocity field is virtually unchanged from the Newtonian case and the polymer conformations are strongly localized to the critical layer positions $y = \pm 0.82$. Sufficiently small perturbations, e.g. $\epsilon = 1$, decay to the laminar state, as they must since that state is linearly stable. However, larger perturbations $\epsilon = 5, 10$ and 100, where nonlinear mechanisms play a role, $\hat{\alpha}_{xx}$ settles to a finite value corresponding to the VNTSA. The initial condition $\epsilon = 5$ that starts from below the VNTSA in $||\hat{\alpha}_{xx}||_\infty$ shows an initial growth phase before saturating onto the VNTSA, whereas $\epsilon = 10$ and 100 relax onto the VNTSA from above.

For comparison, the dashed lines on Figure 6.3 show the linearized evolution starting from the same initial conditions; these all decay to laminar, illustrating the role of nonlinearity in the transition to the VNTSA. This state is robust: initial perturbation amplitudes over a wide range will evolve to it. However, initial conditions with very large magnitudes (e.g. $\epsilon = 6000$) evolve to EIT: as noted above, both EIT and

VNTSA are attractors at the chosen parameters (as is the laminar state).

We have also used initial conditions of the laminar state plus velocity perturbations somewhat similar to the ones used by Page and Zaki [2015]. These perturbations satisfied incompressibility and were sinusoidal in nature with streamwise and wall normal periods equal to the domain size. When appropriate magnitudes are used, transient growth of polymer stress followed by a decay to the VNTSA is observed.

In 3D channel flow simulations of Oldroyd-B fluids at $Re = 3000$, $Wi = 4$ to 6, $\beta = 0.9$, Min *et al.* [2003] observe a transient (~ 500 time units) before an abrupt jump to the fully developed state. These observations were made starting from turbulent Newtonian initial conditions. In the present work, we used an average of about 2500 TU of data, and in some cases more than 5000 TU to calculate the statistics, and have observed no similar transition in any simulations of VNTSA in the parameter space considered here.

Figure 6.4b is a snapshot showing the typical fluctuation structure of the VNTSA at $Wi = 13$. The streamwise conformation $\hat{\alpha}_{xx}$ has tilted sheets highly localized near $y = \pm 0.82$ and contours of wall normal velocity $\hat{v}$ span the entire channel. This structure bears strong resemblance to the TS mode shown in Figure 6.4a. The VNTSA is thus a weakly nonlinear self-sustaining state whose primary structure is the viscoelastic TS mode. We elaborate in the following section on the linear TS mode and its connections to the VNTSA.

In the VNTSA state, the velocity fluctuations are very weak, and the mean wall shear rate displays a very small change from laminar. This can be understood on the grounds that changes of the mean wall shear rate correspond to fluctuations with $k_x = 0$, which arise only due to nonlinear interactions. Since the primary

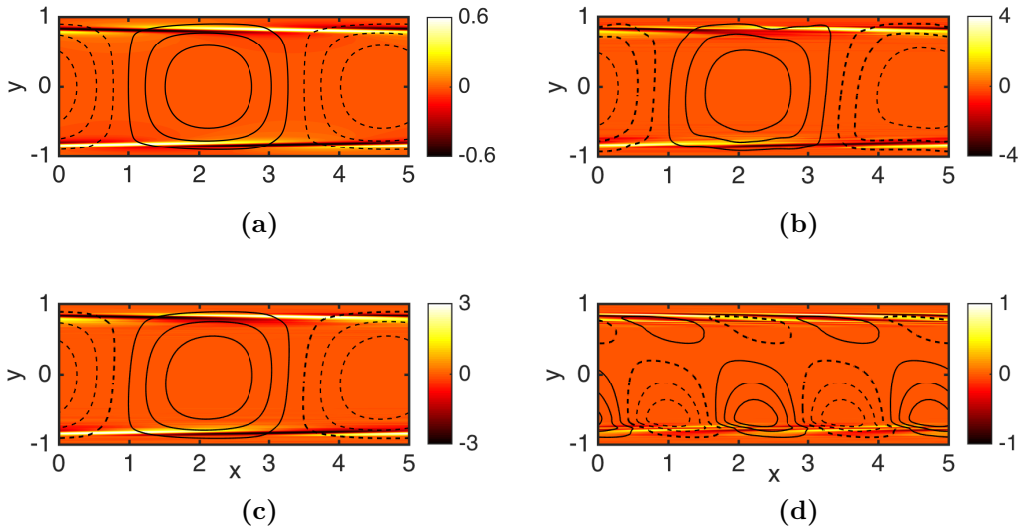

Figure 6.4: (a) Structure of the linear TS mode at $Re = 3000$, $Wi = 13$, $L_x = 5$. Magnitude of the eigenmode is arbitrary and values shown here correspond to $\epsilon = 1$. (b): Snapshot of the fluctuation structure of the VNTSA at $Re = 3000$, $Wi = 13$. (c) and (d): The $kL_x/2\pi = 1, 2$ components respectively, of the snapshot shown in (b). Shown are contour lines of $\hat{v}$ superimposed on color contours of $\hat{\alpha}_{xx}$.

velocity structure is very weak, the nonlinear effects will be even weaker. To illustrate nonlinear effects, Figures 6.4c and 6.4d, respectively, show the $kL_x/2\pi = 1, 2$, spatial Fourier components of the snapshot shown in 6.4b. Figure 6.4c closely resembles the TS mode, with a slight symmetry-breaking across the centerline $y = 0$. The structure at $kL_x/2\pi = 2$ also displays polymer stress fluctuations localized around the critical layer position, an observation that also holds for higher wavenumbers.

Having established the structure of the flow on the VNTSA branch, we now illustrate the bifurcation scenario of this solution branch by continuing in Wi. The VNTSA branch loses existence at finite amplitude (i.e. in a saddle-node bifurcation) for $Wi \lesssim 6$, as we have confirmed both by using the $Wi = 6$ solution as an initial condition for simulations at lower Wi and by running simulations starting from the laminar state perturbed by the TS mode with small ϵ. For $Wi < 6$ all these ini-

tial conditions decay to laminar. On increasing Wi, the VNTSA branch seems to lose existence beyond $Wi \approx 49$, and initial conditions that land on the VNTSA for $Wi = 49$ evolve to EIT at $Wi = 50$. Due to its weak nature in relation to EIT, the bifurcation scenario associated with the two solution branches is shown on Figure 6.2b in a log scale using the L_∞ norm of $\hat{\alpha}_{xx}$ as the amplitude measure. The EIT solutions in Figure 6.2a are depicted again in Figure 6.2b as the upper stable branch (solid red) with this measure.

Since the VNTSA and EIT are both stable states, we were also able to perform edge tracking to find unstable solutions intermediate between these two states. Five Wi values (13, 15, 20, 40 and 45) were studied. Repeated bisections were performed until trajectories stayed on the edge for an average of 300 TU. The red-dashed line on Figures 6.2a and b indicates solutions (all time-dependent) on this intermediate branch. The magnitude of fluctuations along this branch monotonically decreases on increasing Wi, displaying values close to EIT at $Wi = 13$ and values to close to VNTSA at $Wi = 45$. Furthermore, this branch also displays fluctuations that resemble the viscoelastic TS mode, as illustrated below. A more detailed link between VNTSA and EIT might be established through numerical continuations of underlying traveling wave solutions; this is a topic of future endeavors.

To complete this discussion, we note that the bifurcation scenario we observe implies the existence of an edge between the VNTSA and the laminar state, which could in principle also be found using edge tracking. However, the weak nature of the VNTSA implies that this edge would be even weaker, thus making this a challenging task.

Figure 6.5a shows the fluctuation structure of the VNTSA at $Wi = 8$, close to

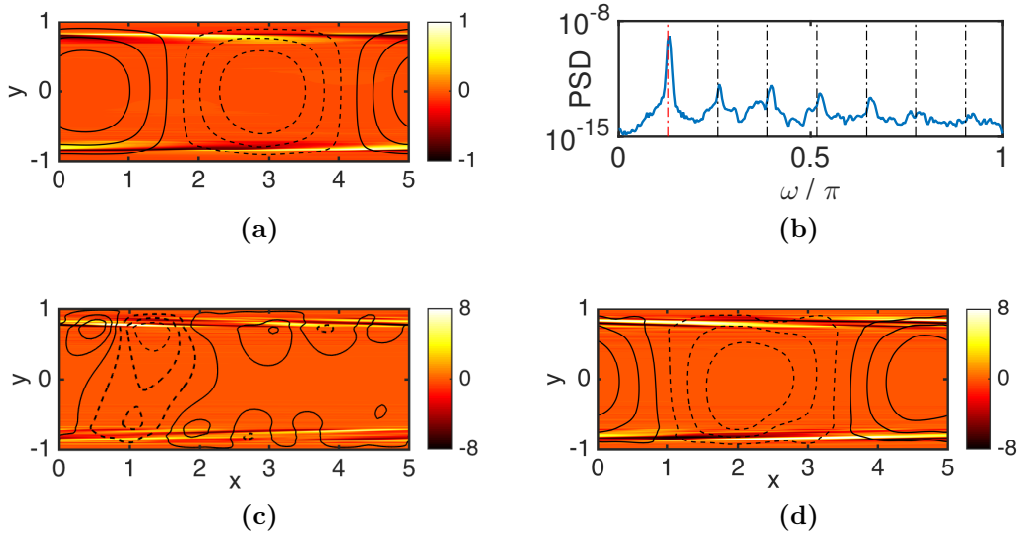

Figure 6.5: (a): Fluctuation structure of the VNTSA and (b) power spectral density (PSD) of v at position $(0, 0.825)$ at $Re = 3000$, $Wi = 8$. Frequencies corresponding to the TS mode (red-dashed) and its higher harmonics (black-dashed) are also shown. (c) and (d): snapshots of the VNTSA structure for $Re = 3000$, $Wi = 20$. Contour plots follow the same format as in Figure 6.4.

the point where it first comes into existence. The structure closely resembles the TS mode and does not change appreciably with time. The flow is almost a pure nonlinear traveling wave with some weak non-periodicity, as indicated in the power density plot of the wall normal velocity at position $(0, 0.825)$ shown in Figure 6.5b. The spectrum is mainly composed of the dominant TS mode frequency and its higher harmonics. The dynamics and structures get more complicated as Wi increases. Figure 6.5c shows a typical snapshot at $Wi = 20$, which clearly is more complex than a TS mode. However, at this Wi, the VNTSA still intermittently displays clear TS-like structures such as the snapshot in Figure 6.5d.

We now turn to the flow structures at various positions on the bifurcation diagram, Figure 6.2b. Figures 6.6a, c and e are representative snapshots of VNTSA, the intermediate branch and EIT respectively, at $Wi = 13$ i.e. near the loss of exis-

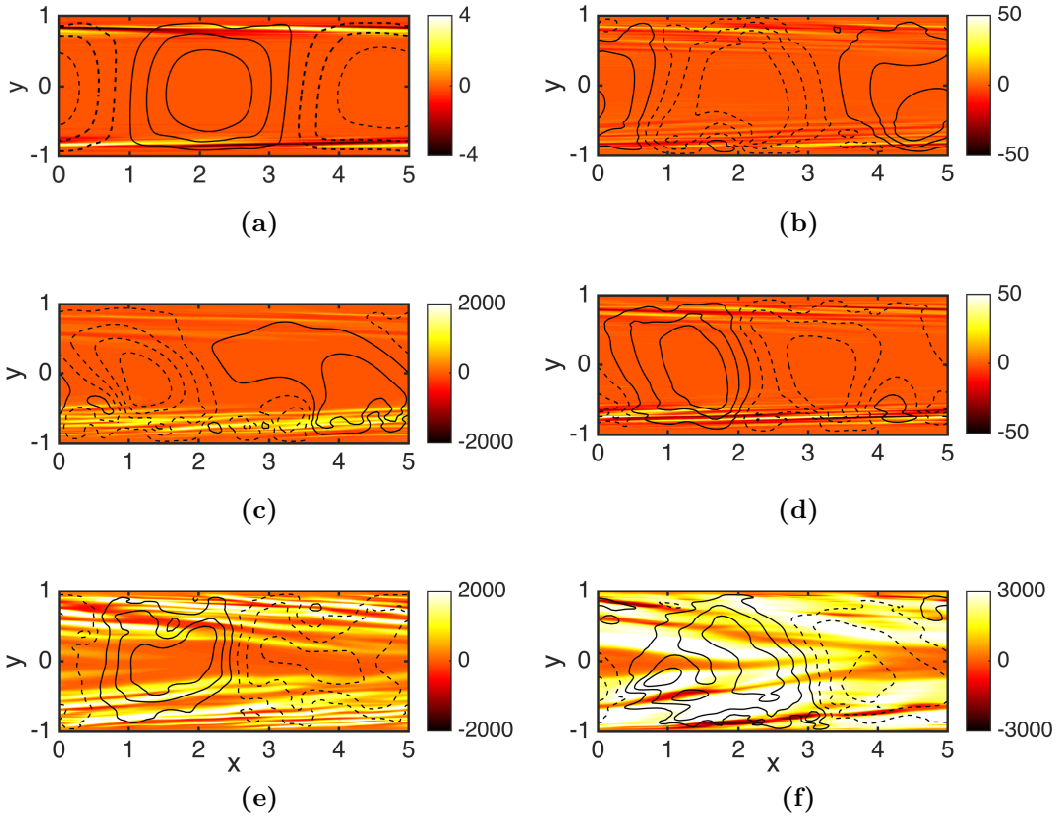

Figure 6.6: (a), (c) and (c): Snapshots of VNTSA, intermediate branch and EIT respectively at $Wi = 13$. (b), (d) and (f): Snapshots of the same solution branches at $Wi = 45$. Deviations from the laminar base state shown as earlier. Color scales are intentionally centered about 0 for comparison purposes.

tence of EIT. As detailed in the description of Figure 6.4 and shown again in Figure 6.6a, VNTSA exhibits a weak structure that strongly resembles the viscoelastic TS mode. At this low Wi, the intermediate branch (Figure 6.6c) displays a much stronger fluctuation structure, on the same order of magnitude as the structures seen at EIT (Figure 6.6e). Moreover, the intermediate branch exhibits overlapping sheets of polymer stretch(especially on the bottom side of the channel at the time instant shown) that strongly resemble those seen at EIT.

Figures 6.6b, d and f show the structures at $Wi = 45$, close to the point where the

intermediate branch seems to turns around to merge with VNTSA. The fluctuations on the intermediate branch (Figure 6.6d) decrease in magnitude on increasing Wi, and at $Wi = 45$ become comparable to those on VNTSA branch as shown in Figure 6.6b. Furthermore, structure on this branch goes from displaying overlapping sheets of polymer stretch at low Wi to localized striations at high Wi similar to those of VNTSA. In sharp contrast to the localized structures just described, EIT (Figure 6.6f) continues to display sheets of polymer stretch which get stronger on increasing Wi. All three solution branches continue to intermittently display wall normal velocity fluctuations that resemble the TS mode.

6.3.3 Linear analyses

In this section we elaborate on the linearized problem and its connection to the attractors described above using linear stability and resolvent analyses. The spectrum corresponding to disturbances with wavelengths equal to the DNS box size, i.e. $k = 2\pi/5$, has a least-stable eigenvalue at $c \approx 0.32 - 0.010i$, and the associated eigenfunction is the viscoelastic extension of the TS mode. For low values of Wi, the mode is less stable than its Newtonian counterpart, while for $Wi \gtrsim 2$, it becomes more stable with increasing elasticity; this non-monotonic behavior has been reported by Zhang *et al.* [2013], who attribute it to viscoelastic modification of the phase difference between u and v. Nevertheless, over the range of Wi considered here, the eigenvalue varies by less than 1% of the Newtonian value. The linear stability of the laminar state in this range of Wi, and the very weak dependence of c on Wi continues up to at least $Re = 6000$, confirming the observations in Section 6.3.2 that finite amplitude disturbances are required to trigger transition to EIT or the VNTSA. However, linear

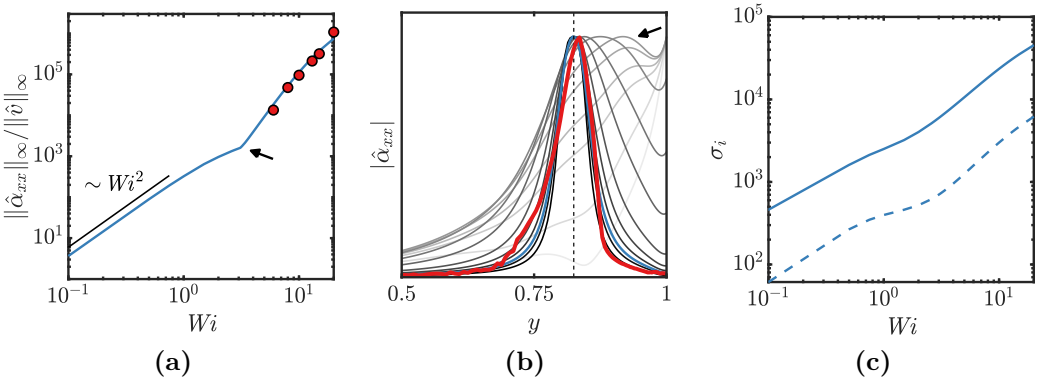

Figure 6.7: (a) Solid blue line: ratio of peak amplitudes of $\hat{\alpha}_{xx}$ and $\hat{v}$ for the linear TS mode as a function of Wi; circles: amplitude ratio for the VNTSA. (b) Magnitude of $\hat{\alpha}_{xx}$ for the linear TS mode for several values of Wi in the range [1, 20]. Darker lines indicate higher values of Wi. The thick red line shows the averaged magnitude of $\hat{\alpha}_{xx}$ from the VNTSA for $Wi = 13$. For comparison, the linear TS mode profile for the same Wi is shown in blue, and the vertical dashed line marks the critical layer location $y_c = 0.825$. The arrow indicates the value of Wi corresponding to the arrow in (a). (c) First two singular values of the resolvent operator for k and c corresponding to the linear TS mode.

instabilities not related to the TS mode have been found in other regions of parameter space [Garg *et al.*, 2018, Chaudhary *et al.*, 2019], implying the possibility of different attractor families in those regions.

A measure of the relative importance of the conformation tensor and velocity disturbances is the ratio of the peak amplitudes of $\hat{\alpha}_{xx}$, (the largest component of the conformation tensor), and $\hat{v}$. This ratio is shown in Figure 6.7a. Two distinct regimes are apparent, with the transition between the two occurring at $Wi \approx 3.1$. The low Wi regime scales as Wi^2, which is the same scaling as in linear shear flow. The amplitude ratio above the change in slope does not exhibit power law scaling. The change in slope at $Wi \approx 3.1$, can be understood by examining the $\hat{\alpha}_{xx}$ mode shapes, the magnitudes of which are plotted in Figure 6.7b for several values of Wi in the range shown in Figure 6.7a. For small Wi, the disturbance is largest at the wall and decays rapidly away from it. Therefore, the Wi^2 scaling in this regime can be explained by the fact that the leading-order approximation of the base flow

very near the wall is simple shear. As Wi increases, this value decreases, while a new local maximum emerges and grows, becoming the global maximum just above $Wi = 3$; the arrow in the figure indicates the profile where this occurs. Upon further increase in Wi, the maximum gradually shifts away from the wall, and the modes become increasingly localized around the location of the critical layer y_c, at which the real part of the wavespeed equals the base flow velocity. The critical layer for $Wi = 13$ is indicated by the vertical dashed line. This suggests that a critical layer mechanism is responsible for the change in scaling at large Wi, though at present we do not understand the specific origin of this result. Interestingly, the Wi at which the VNTSA comes into existence is only slightly larger than that at which the transition to critical layer scaling occurs.

Also shown in Figure 6.7a is the amplitude ratio computed from the VNTSA for several values of Wi. Excellent agreement between the linear and nonlinear results quantitatively reinforces the TS-mode-like nature of the VNTSA. Additionally, the profile of $|\hat{\alpha}_{xx}|$, averaged in the streamwise direction and over many snapshots, for the VNTSA at $Wi = 13$ is shown by the thick red line in Figure 6.7b, and the blue line highlights the linear mode for the same Wi. The VNTSA profile exhibits the same localization, and the location of the peak value is in close agreement with the critical layer location.

Figure 6.7c shows the first two singular values of the resolvent operator for k and c corresponding to the linear TS mode. Shekar *et al.* [2019] showed that such modes are the most-amplified 2D disturbances in this parameter regime and that the leading response mode is nearly identical to the TS eigenmode; for this reason the resolvent modes are not plotted separately. The substantial increase in the leading

singular value with Wi indicates that this amplification becomes much stronger with increasing elasticity, and consequently that considerably smaller disturbances may be sufficient to trigger self-sustaining nonlinear mechanisms. Further, the symmetry of the flow geometry about $y = 0$ means that resolvent modes typically come in pairs having similar amplification, with one mode having a symmetric $\hat{v}$ response and the other having an antisymmetric $\hat{v}$ response. However, the growing separation between the first and second singular values with increasing Wi indicates that this pairing is broken by elasticity, and that the symmetry exhibited by the TS mode is preferred in terms of linear amplification.

6.3.4 Broader context: flow geometry and dimensionality

The results described above are limited to two-dimensional channel flow. Here we describe how they may be viewed in the broader context of turbulent drag reduction, first with regard to how they may relate to the pipe flow geometry and then in the full context of three-dimensional turbulence.

As noted in the Introduction, elastoinertial turbulence with very similar features has been observed in both channel and pipe flows. A natural question, then, is to what extent the above channel flow results are relevant to the pipe flow case. While it is true of course that there is no linear instability of Newtonian pipe flow, the general structures of the linear stability problem for the pipe and channel are very similar. The A, P, and S (wall, center, strongly decaying) families of modes for the channel flow problem also arise in the pipe, as illustrated in Figs. 4.18 and 4.19 of Drazin and Reid [2004]. (In channel flow, one of the wall modes, the TS mode, goes unstable.) Additionally, critical layers are a strong source of linear amplification in pipe flow, as

they are in channel flow [McKeon and Sharma, 2010a].

Turning to nonlinear behavior in Newtonian pipe flow, an important difference from channel flow is the apparent absence of subcritical traveling wave solutions that are analogous to the nonlinear Tollmien-Schlichting waves [Patera and Orszag, 1981]. That is, in pipe flow there is no nonlinear solution branch that corresponds to the NNTSA described above. Given this observation, one might wonder whether the results presented here for viscoelastic channel flow are relevant for pipe flow.

To address this issue, we make the following remarks. The key observation of the present work is that the TS mode is nonlinearly excited *by viscoelasticity*. The resulting solution branch, the VNTSA, is not connected, at least in this part of parameter space under consideration, to the Newtonian branch, indicating that the nonlinear mechanism that sustains it is distinct from the nonlinear mechanisms sustaining the Newtonian branch. So the absence of a *Newtonian* mechanism for nonlinear sustainment of Tollmien-Schlichting-like traveling waves does not imply the absence of a *viscoelastic* mechanism. Furthermore, as noted in the Introduction, pipe flow simulations of EIT [Lopez *et al.*, 2019] display essentially two-dimensional velocity fluctuations localized near the wall that are similar to those reported in channel flow. These are precisely what would be expected in pipe flow based on the observations we report here for channel flow, i.e. a critical layer mechanism associated with excitation of a Tollmien-Schlichting-like mode. At the same time, in more strongly viscoelastic regimes, Garg *et al.* [2018] and Chaudhary *et al.* [2020] have found a center mode instability for pipe flow; for the Oldroyd-B model with $Re = 3500, \beta = 0.9$, instability occurs when $176.9 < Wi < 4783.6$. A related instability might be present in the channel flow problem. These results open up the possibility that other states unrelated to

the nonlinear excitation of a wall mode may also play a role at EIT in both channels and pipes, especially at high *Wi*.

We now turn to the topic how the present results are related to the fully three-dimensional context, beginning with a brief overview of Newtonian near-wall turbulence.

Newtonian turbulence is of course, strongly three-dimensional, with the dominant near-wall structure comprised of coherent wavy streamwise vortices. In all of the canonical wall-bounded shear flow geometries (pipe flow, channel flow, plane shear (Couette) flow), families of three-dimensional nonlinear traveling wave solutions to the Navier-Stokes equations (NSE) have been discovered [Waleffe, 1998, 2001, 2003, Wang *et al.*, 2007, Hof *et al.*, 2004, Eckhardt *et al.*, 2007, 2008, Duguet *et al.*, 2008b, Wedin and Kerswell, 2004]. These solutions are often denoted "exact coherent states" (ECS), and their predominant structure is very similar to that observed in wall turbulence: a mean shear and wavy streamwise vortices. (In particular, they bear no structural resemblance to Tollmien-Schlichting waves and do not arise from a linear instability of the laminar state.) Related, but more complex states have been found as well, that are not pure traveling waves but rather "relative periodic orbits" that are time-periodic modulo a phase shift in one of the translation-invariant spatial directions [Duguet *et al.*, 2008a]. In minimal domains at Reynolds numbers near transition, the turbulent dynamics have been found to be organized, at least in part, around these solutions (see, e.g. Gibson *et al.* [2008], Kawahara *et al.* [2012], Park and Graham [2015]).

It has long been known that one of the effects of viscoelasticity on wall turbulence is to weaken and broaden the near-wall streamwise vortices [Kim *et al.*, 2007, White

and Mungal, 2008]. A number of studies have addressed this observation by investigating the effect of viscoelasticity on ECS, which as noted, capture this streamwise vortex structure [Stone *et al.*, 2002, Stone and Graham, 2003, Stone *et al.*, 2004, Li *et al.*, 2005, 2006b, Li and Graham, 2007]. Indeed, the effect of viscoelasticity is to weaken these structures; the polymer stresses directly counteract the streamwise vortices.

In particular, Li and Graham [2007] studied the bifurcation scenario for a particular family of channel flow ECS (Waleffe [1998]) in a parameter regime very close to that considered here. At $Re = 1500$, this ECS family is sufficiently weakened by viscoelasticity to lose existence at $Wi \approx 16$, somewhat above the value $Wi \approx 10$ beyond which Newtonian turbulence cannot self-sustain in the DNS study of Shekar *et al.* [2019]. (This discrepancy is consistent with what we know about transition in the Newtonian case: channel flow turbulence is self-sustaining above $Re \approx 1000$, while ECS can exist in that case down to $Re \approx 660$ [Shekar and Graham, 2018].) Extrapolating slightly from the results of Li and Graham [2007], one can estimate that at $Re = 3000$, this ECS family loses existence at $Wi \approx 25$.

Given that, in the present 2D work with $Re = 3000$, EIT is found at $Wi \gtrsim 13$ and the VNTSA above at $Wi \gtrsim 6$, there would appear to be a regime $6 \lesssim Wi \lesssim 25$ in which both 2D and 3D structures may exist and interact. Furthermore, existing results on the effect of viscoelasticity on ECS are limited to one ECS family, and there certainly may be others that can persist to higher Wi. Consistent with this analysis, a number of studies have reported near-wall EIT-like spanwise oriented structures, with 3D quasistreamwise vortices further away from the wall [Dubief *et al.*, 2013, Choueiri *et al.*, 2018, Pereira *et al.*, 2019a,b]. How the 2D and 3D structures interact

is an important topic for future work.

6.4 Conclusion

This study focuses on two-dimensional plane channel flow of a very dilute polymer solution at $Re = 3000$. At sufficiently high Wi, elastoinertial turbulence is observed in this parameter regime, and the focus of the present work is to make progress toward understanding the structures and mechanisms underlying the dynamics in this regime. We report here the existence of a new attractor that is based on the viscoelastic linear Tollmien-Schlichting mode and is nonlinearly sustained by viscoelastic stresses. We denote this as the viscoelastic nonlinear Tollmien-Schlichting attractor (VNTSA). At the parameters considered here, this solution branch is not connected to the Newtonian branch of nonlinear self-sustained Tollmien-Schlichting waves; it would be interesting to learn whether they become connected at higher Re. In a domain of dimensionless length 5, this solution comes into existence at finite but very small amplitude when $Wi \gtrsim 6$, increasing in amplitude until $Wi \approx 49$ where it loses existence again. At higher Wi, initial conditions corresponding to this solution branch at lower Wi evolve into elastoinertial turbulence. In general, we do not find pure nonlinear traveling waves, but until Wi is large, the nonperiodic fluctuations are very small. The connection of the VNTSA to the linear TS mode is established via their strong structural similarities, including a quantitive agreement between the relative magnitudes of the velocity and stress fluctuations. The value of Wi at which the VNTSA comes into existence is close to where the relative amplitude of the stress and velocity fluctuations for the linear TS mode undergoes a change in scaling. Above

this transition the stress fluctuations become highly localized at the position of the critical layer.

Taken together, these results suggest that, at least in the parameter range considered here, the bypass transition leading to EIT is mediated by nonlinear amplification and self-sustenance of perturbations that excite the Tollmien-Schlichting mode. Gaining an understanding of the mechanism underlying this phenomenon will shed light on the origin of elastoinertial turbulence.

Chapter 7

Tollmien-Schlichting route to elastoinertial turbulence[a]

7.1 Introduction

In chapter 6, we studied the bifurcation scenario of 2D EIT at $Re = 3000$ and its ties to nonlinear self-sustaining TS waves. In that study, the domain length was chosen to be five channel half-heights, because at this length, self-sustaining nonlinear Tollmien-Schlichting waves exist in the Newtonian case for $Re \gtrsim 2800$ [Jiménez, 1990]. Some key results of this study that form the basis for the present work are described below and summarized in Figure 7.1. At this parameter set, 2D EIT (upper branch of the red curve on the bifurcation diagram of Figure 7.1a) comes into existence at $Wi \approx 13$. A snapshot of the xx-component of the polymer stretch, displaying tilted, *multilayered*

[a]This chapter includes content from: Shekar, A., McMullen, R. M., McKeon, B. J., and Graham, M. D. (2021). Tollmien-Schlichting route to elastoinertial turbulence. To be submitted to Journal of Fluid Mechanics.

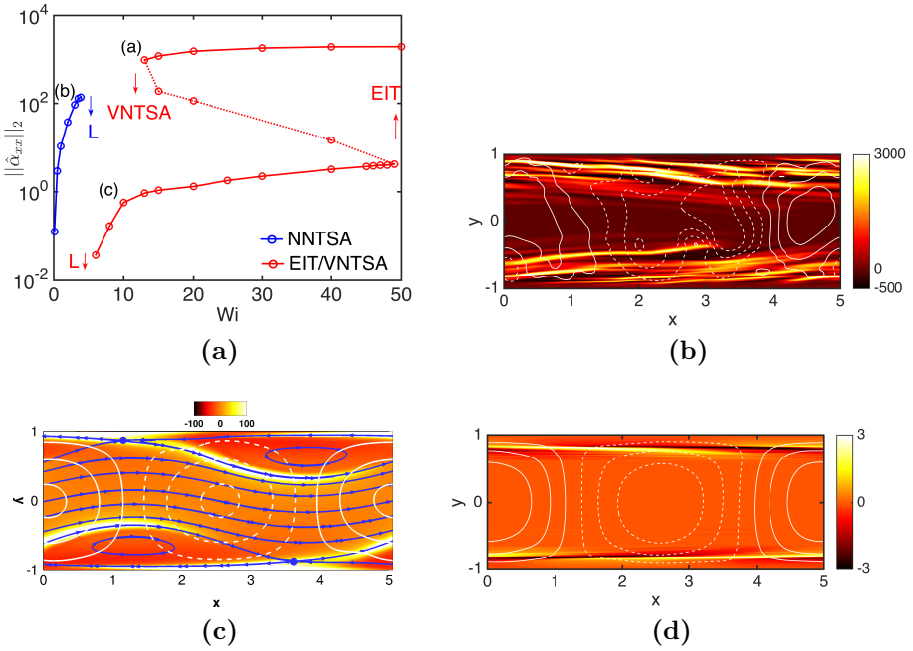

Figure 7.1: (a) Time-averaged L_2-norm of $\hat{\alpha}_{xx}$ vs Wi of the three solution branches identified in Shekar *et al.* [2020] at $Re = 3000, L_x = 5$. Snapshots corresponding to (b) 2D EIT at $Wi = 13$ (point a on the bifurcation diagram); (c) NNTSA at $Wi = 3$ (point b); and (d) VNTSA at $Wi = 10$ (point c). Shown are white contour lines of wall normal velocity, $\hat{v}$ superimposed on color contours of xx-component of polymer conformation tensor ($\hat{\alpha}_{xx}$). Here $\hat{}$ denotes deviations from laminar base state. For (b), we also show the streamlines (blue) in a reference frame moving at the wave speed and the hyperbolic stagnation points (blue dots).

sheets at EIT is shown in figure 7.1b. We identified two separate branches of attractors based on the TS mode. The first, (solid blue curve on Figure 7.1a), originates with the Newtonian nonlinear traveling wave solution and loses existence above $Wi \approx 4$. This solution branch is termed the Newtonian nonlinear Tollmien-Schlichting attractor (NNTSA)); it develops a *sheet* of high polymer stretch that starts out near the wall and arches away from it as shown in Figure 7.1c. This structure originates with the Kelvin cat's eye structure of TS waves, specifically its near-wall hyperbolic stagnation points (blue circles in Figure 7.1c). These observations demonstrate the capability of nonlinear TS critical layer mechanisms in generating sheets of polymer stretch.

The second solution branch (lower solid-red curve) with TS-like structure comes

into existence at finite amplitude when $Wi \approx 6$. This branch, denoted the viscoelastic nonlinear Tollmien-Schlichting attractor (VNTSA), was first found by starting with an initial condition at EIT, then lowering Wi below the threshold value $Wi \approx 13$ noted above. It has extremely weak fluctuations and seems likely to be related to the "pseudo-laminar" state observed by Pereira *et al.* [2019a]. This state displays *striations* of polymer stretch localized at the critical layer (figure 7.1d) and is structurally very similar to the linear TS mode at the same value of Wi, though it displays weakly chaotic rather than purely time-periodic (traveling wave) fluctuations. The existence of such a state indicates the presence of a nonlinear viscoelastic mechanism for self-sustenance of TS structure, an observations that has important implications in the broader context of other flow scenarios such as pipe flow, where no linear TS instability exists. On increasing Wi, the VNTSA develops multilayered striations of polymer stretch before joining up with 2D EIT through an unstable branch indicated by the red-dashed line in figure 7.1a.

In the present work, we elaborate on the relationship between nonlinear Tollmien-Schlichting structures and elastoinertial turbulence. In section 7.3.1, we describe the evolution of the VNTSA as Re increases from 3000 to 10000. We detail observations of a coil-stretch transition, with a jump in polymer stretching – almost two orders of magnitude – when the local Wi at the hyperbolic stagnation point crosses $\frac{1}{2}$. Accompanying this transition is a structural change from localized striations to extended sheets. These form the necessary ingredients for a process we coin the "sheet shedding process" responsible for generating multilayered sheets of polymer stretch, a key characteristic of EIT. We describe this process at $Re = 10000$ and trace its origins in section 7.3.2. At this Reynolds number, the Newtonian nonlinear

Tollmien-Schlichting solution is directly connected to EIT as Wi increases. Interesting intermittent dynamics occur along this branch, as described in Section 7.3.3. Finally, in Section 7.3.4, we show the robustness of these observations with respect to polymer extensibility and domain size.

7.2 Formulation

This study focuses on two-dimensional pressure-driven channel flow with constant mass flux. The x and y axes are aligned with the streamwise and wall-normal directions, respectively. Lengths are scaled by the half channel height l, so the dimensionless channel height $L_y = 2$. The domain is periodic in x with length L_x. Velocity $\boldsymbol{v}$ is scaled with the Newtonian laminar centerline velocity U; time t with l/U, and pressure p with ρU^2, where ρ is the fluid density. The polymer stress tensor $\boldsymbol{\tau}_p$ is related to the polymer conformation tensor $\boldsymbol{\alpha}$ through the FENE-P constitutive relation, which models each polymer molecule as a pair of beads connected by a nonlinear spring with maximum extensibility b.

We solve the momentum, continuity and FENE-P equations:

$$\frac{\partial \boldsymbol{v}}{\partial t} + \boldsymbol{v} \cdot \boldsymbol{\nabla} \boldsymbol{v} = -\boldsymbol{\nabla} p + \frac{\beta}{Re} \nabla^2 \boldsymbol{v} + \frac{(1-\beta)}{Re\, Wi} \left(\boldsymbol{\nabla} \cdot \boldsymbol{\tau}_{\mathrm{p}} \right), \tag{7.1}$$

$$\boldsymbol{\nabla} \cdot \boldsymbol{v} = 0, \tag{7.2}$$

$$\boldsymbol{\tau}_p = \frac{\boldsymbol{\alpha}}{1 - \frac{\mathrm{tr}(\boldsymbol{\alpha})}{b}} - \boldsymbol{I}, \tag{7.3}$$

$$\frac{\partial \boldsymbol{\alpha}}{\partial t} + \boldsymbol{v} \cdot \boldsymbol{\nabla} \boldsymbol{\alpha} - \boldsymbol{\alpha} \cdot \boldsymbol{\nabla} \boldsymbol{v} - (\boldsymbol{\alpha} \cdot \boldsymbol{\nabla} \boldsymbol{v})^{\mathrm{T}} = \frac{-1}{Wi} \boldsymbol{\tau}_p. \tag{7.4}$$

Here $Re = \rho U l/(\eta_{\rm s} + \eta_{\rm p})$, where η_s and η_p are the solvent and polymer contributions to the zero-shear rate viscosity. The viscosity ratio $\beta = \eta_{\rm s}/(\eta_{\rm s} + \eta_{\rm p})$. We fix $\beta = 0.97$ and $b = 6400$ for all results except in the last section where we use $b = 10^5$. Since $1-\beta$ is proportional to polymer concentration and b to the number of monomer units, these parameter sets corresponds to a dilute solution of a high molecular weight polymer. The Weissenberg number $Wi = \lambda U/l$, where λ is the polymer relaxation time.

For the nonlinear direct numerical simulations (DNS) described below, a finite difference scheme and a fractional time step method are adopted for integrating the Navier-Stokes equation. Second-order Adams-Bashforth and Crank-Nicolson methods are used for convection and diffusion terms, respectively. The FENE-P equation is discretized using a high resolution central difference scheme [Kurganov and Tadmor, 2000, Vaithianathan *et al.*, 2006, Dallas *et al.*, 2010]. No artificial diffusion is applied. Resolution tests were performed to ensure convergence of statistics. A typical resolution for the following results is $(N_x, N_y) = (131, 602)$. This resolution used was based on mesh convergence results at the highest Re and Wi (10000 and 13) considered here. When the resolution was increased to $(N_x, N_y) = (181, 702)$, the mean polymer stretch deviations from the laminar base state change by less than 1%. We also perform computations in the shift-reflect symmetric subspace innate to the TS family. These computations are done by simulating half the domain and applying the following symmetry to generate the fields in the other half:

$$\begin{bmatrix} u & v & \alpha_{xx} & \alpha_{yx} & \alpha_{yy} \end{bmatrix} (x + L_x/2, y, t) = \begin{bmatrix} u & -v & \alpha_{xx} & -\alpha_{yx} & \alpha_{yy} \end{bmatrix} (x, -y, t). \quad (7.5)$$

7.3 Results and discussion

7.3.1 Viscoelastic Tollmien-Schlichting attractor: from Re=3000 to 10000

The results presented in this section make the connection between the results of chapter 6 and the present work, which will focus on the attractor at $Re = 10000$. We begin our discussion by considering the evolution of the VNTSA as Re is increased from 3000 to 10000 at fixed $Wi = 10$, $L_x = 6.2$. We would like to note the difference in box size from the earlier results. There, L_x was chosen based on the lowest Re for existence of finite amplitude nonlinear TS waves. In contrast, in the present work, L_x was chosen to approximately correspond to the domain size at which the linear TS instability first appears (at $Re = 5772$) [Drazin and Reid, 1981]. This was done so that we could examine, as we do below, the behavior when the TS mode is linearly unstable to explore the relationship between the NNTSA, VNTSA and EIT. Indeed, at the value $L_x = 5$ chosen in the earlier work, the TS mode does not become linearly unstable at any Re.

The blue curve on Figure 7.2a quantifies the evolution of the VNTSA in Re using the time-averaged L_2-norm of $\hat{\alpha}_{xx}$ as a measure. Unless otherwise noted, all quantities reported here are time-averaged. With the attractor being weakly chaotic, at least 3000 time units (TU) of data, and in some cases up to 6000 TU, is used to get an accurate estimate of this quantity. The key observation is that in the range $6000 < Re < 8000$, $||\hat{\alpha}_{xx}||_2$ increases by several orders of magnitude. Note that to capture this large change, a log scale is used. Figures 7.2b and c are representative snapshots of the flow and polymer conformation fields, which illustrate the structural

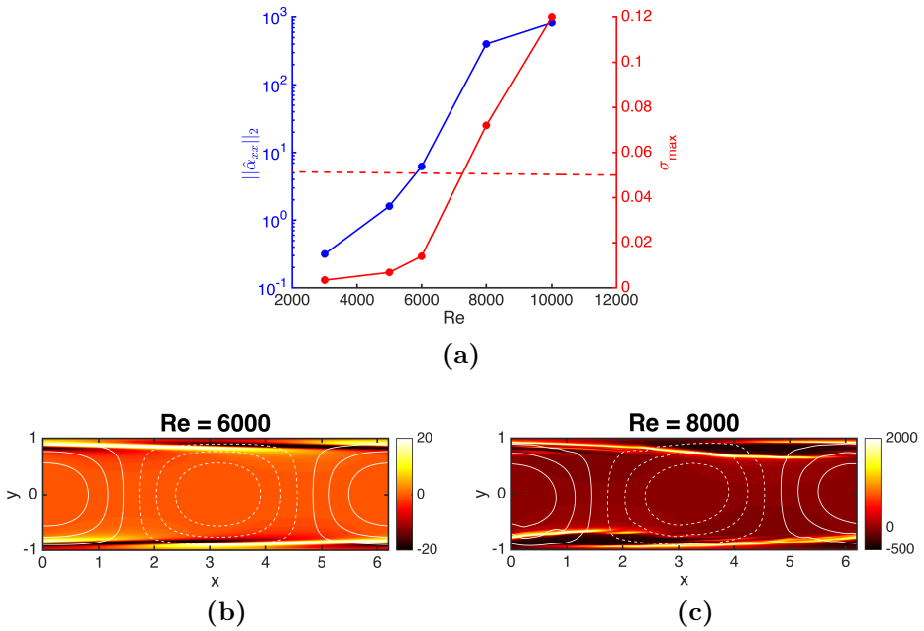

Figure 7.2: (a) L_2-norm of $\hat{\alpha}_{xx}$ (blue) and corresponding mean local stretch rate at the hyperbolic stagnation point (red) along VNTSA branch at $Wi = 10$. Red-dashed line corresponds to local Wi (Wi_{loc}) $= \lambda\sigma_{\max} = 1/2$. (b) and (c) are snapshots of the fluctuation structure of the solution branch at $Re = 6000$ and 8000 respectively. Shown are contour lines of $\hat{v}$ superimposed on color contours of $\hat{\alpha}_{xx}$. Here $\hat{}$ denotes deviations from laminar base state.

change accompanying this transition. Throughout this manuscript, we report the deviations from the laminar state, rather than the total. Otherwise, for cases where the TS structure is weak, especially in the case of $\boldsymbol{\alpha}$, it would not be discernible. Also, all snapshots shown are phase-aligned to focus the reader's attention on the structural evolution.

As at $Re = 3000$, the attractor at $Re = 6000$ (figure 7.2b) continues to display striations of weak polymer stretch fluctuations that are localized near the wall, and closely resembles the linear TS mode. Apart from the obvious quantitative differences, the attractor at 8000 (figure 7.2c) now displays a sheet of polymer stretch emanating from the near-wall stagnation point regions. Further, these structures display an asymmetry in polymer stretch relative to the laminar state unlike the

attractor at 6000. Having said this, the attractor continues to display wall normal velocity fluctuations that extend across the channel and are only slightly modified from $Re = 6000$.

To shed insights into the nature of this transition, we examine the flow kinematics more quantitatively. Aside from a very weak nonperiodic component, the flow is a traveling wave displaying the characteristic Kelvin cat's eye streamlines, and the corresponding hyperbolic stagnation points, in the traveling frame. Denoting the largest eigenvalue of the velocity gradient $\nabla \mathbf{v}$ at these points as $\sigma_{\max}$, polymers are strongly stretched in the vicinity of these points when $\lambda\sigma_{\max} > 1/2$ [De Gennes, 1974]. Defining a local Weissenberg number $Wi_{\text{loc}} = \lambda\sigma_{\max}$, this criterion becomes $Wi_{\text{loc}} > 1/2$. Figure 7.2a reports estimates (red) of $\sigma_{\max}$ vs. Re. Since the attractors are not pure traveling waves, these estimates are based on time-averaging over multiple snapshots sampled over the attractor. For each snapshot, the instantaneous wavespeed is estimated using adjacent snapshots spaced 1 time unit before and after. This wavespeed is then subtracted off of the streamwise velocity to yield the velocity field in the traveling frame, from which the stagnation point positions can be identified and $\sigma_{\max}$ estimated. The drastic change between $Re = 6000$ and 8000 coincides with Wi_{loc} crossing the coil-stretch threshold $Wi_{\text{loc}} = 1/2$. Accompanying this transition is the appearance of a new process responsible for generating multilayered sheets of polymer stretch from a single sheet of stretching. We coin this process the sheet shedding process and expand on this in the next section.

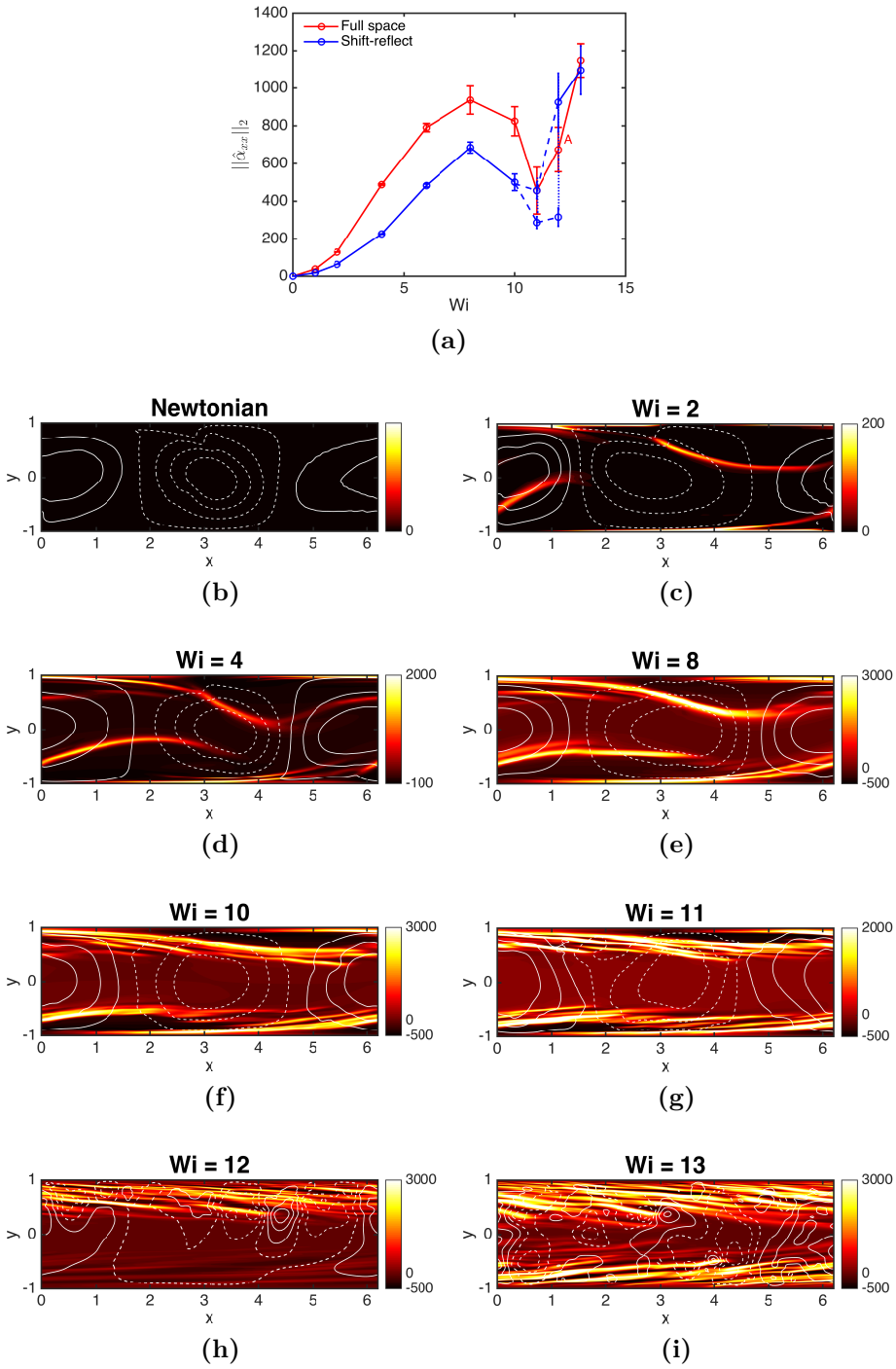

Figure 7.3: (a) $||\hat{\alpha}_{xx}||_2$ vs Wi at $Re = 10000$. Here, 'A' indicates assymetry in the attractor. (b) - (i) are snapshots of the fluctuation structure of the attractor at the indicated Wi.

7.3.2 Origins of sheet shedding process and elastoinertial turbulence

To shed light on the origin of the sheet shedding process, we now consider the evolution of this attractor with Wi at fixed $Re = 10000$. The attractor presented in the previous section at $Wi = 10$ can be traced back to the Newtonian attractor on decreasing Wi. The VNTSA branch thus becomes connected to the Newtonian branch at higher Re. Going forward, we do not distinguish between NNTSA and VNTSA and refer to the attractor as the TS attractor.

Figure 7.3a shows the evolution of this attractor with Wi using $||\hat{\alpha}_{xx}||_2$ as the measure. Also shown on this plot are the standard deviations of this statistic to give a sense of the temporal intermittency of the dynamics along the branch. Here, the results in full space (red) are shown along with the results in a shift-reflect (S-R) symmetric subspace (blue) innate to the TS wave obtained from symmetrized DNS. The full space attractor displays an increasing trend from Newtonian to $Wi = 8$ followed by a decrease up to $Wi = 11$ and an increase beyond that. The instantaneous dynamics of $||\hat{\alpha}_{xx}||_2$ go from 2-torus dynamics up to $Wi = 2$ to mild chaos at $Wi = 4$. This temporal modulation is initial indication of viscoelastic effects starting to play a role from $Wi = 4$. As the Wi increases beyond this, the dynamics get more complicated and reach a peak in intermittency around $Wi = 11$. Here, intermittent bursts characterized by a sharp temporary increase in the instantaneous $||\hat{\alpha}_{xx}||_2$ can be seen as a persistent phenomena.

Many of the observations described in the full space carry forward to the S-R subspace up to $Wi = 10$. The same non-monotonic trend in $||\hat{\alpha}_{xx}||_2$ accompanied by a temporal modulation around $Wi = 4$. In other words, the full space attractor can

be seen as a modification of the attractor in the S-R subspace. Beyond $Wi = 10$, the dynamics in the S-R space alternate between two metastable states (indicated by vertical dotted lines) before settling on the stable symmetric attractor at $Wi = 13$. We will expand on this observation in the next section.

To get a sense of what underlies the dynamics, we now turn to the flow structures at various positions along the branch in full space. The Newtonian attractor (figure 7.3b) displays the usual wall normal velocity contour lines across the channel height. At low $Wi = 2$ (figure 7.3c), the attractor develops a sheet of polymer stretch that starts near the wall and arches closer to the centerline. This is typical of the NNTSA structure described in the introduction and can be attributed to the Kevin cats eye critical layer kinematics of the attractor. Going from $Wi = 2$ to 4, the attractor starts to display near-wall multilayered sheets as seen between $x \approx 3$ and $x \approx 5$ in figure 7.3d. This effect gets more pronounced as we move along the branch with $Wi = 11$ intermittently displaying strong multilayered sheets (figure 7.3g) similar to those seen at EIT at $Wi = 13$ (figure 7.3i). Interestingly, $Wi = 12$ displays strong multilayered sheets on one half of the channel with no particular preference towards either half. By symmetry, for every state with fluctuations localized near the top, there is a dynamically equivalent state localized near the bottom. Asymmetric states similar to this have been observed in 2D Newtonian channel flow [Markeviciute and Kerswell, 2020] and could be playing a role here. The authors report such states over the range of $Re \in [2.1 \times 10^4, 7.2 \times 10^4)$. Further, these states transitioned to 2D turbulence on one side of the channel only. This marked structural transition beyond $Wi = 11$ coincides with an increasing trend in $||\hat{\alpha}_{xx}||_2$ in figure 7.3a and giving rise to the EIT branch beyond $Wi = 11$. Thus, one connected branch goes from the Newtonian TS

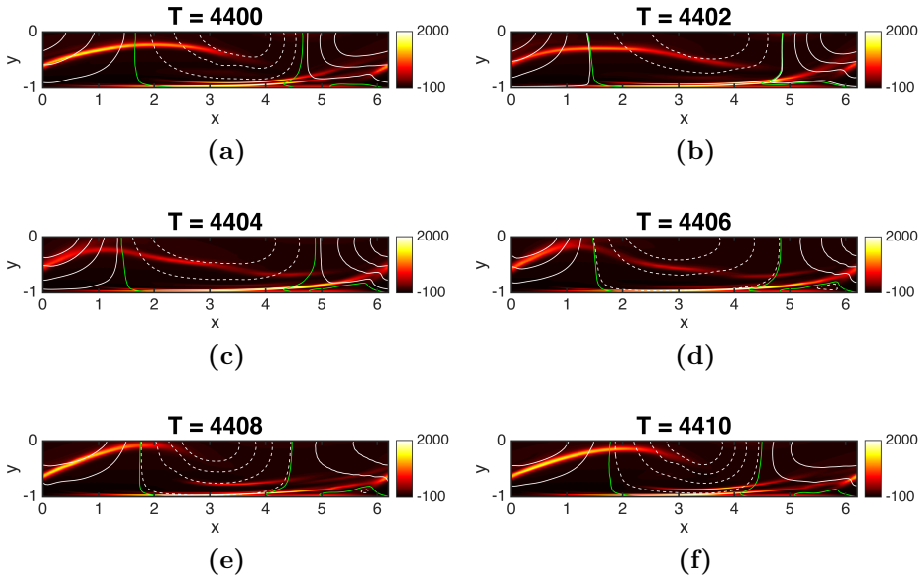

Figure 7.4: (a) - (f) are snapshots of the fluctuation structure of the attractor at $Re = 10000$, $Wi = 4$. Snapshots are taken from T = 4400 to 4410 every 2 time units respectively. Green lines correspond to $\hat{v} = 0$ i.e. where wall normal velocity changes sign. Bottom half of the domain shown.

attractor to EIT. We now describe the process through which this branch makes the structural transition from a single sheet at low Wi to the multilayered sheets seen at EIT. We coin this process as the *sheet shedding process*.

To elaborate on the sheet shedding process, we focus on the attractor at $Re = 10000$, $Wi = 4$ i.e. close to where this process first comes into existence. Figures 7.4a to f cover one cycle of the process and correspond to T = 4400 to 4410 taken every 2 time units respectively. The following description focusses on the bottom half of the channel with the same process taking place in the top half.

As the name suggests, this process involves the shedding of sheets of polymer stretch from the primary TS structure that gives rise to multilayered sheets. The onset of this process involves the arched portion of the TS structure seen between $x = 0$ and $x \approx 4$. At the instant shown in (a), this arched section goes from a region

of positive wall normal velocity to negative. The locations where the wall normal velocity changes sign is shown using green lines as seen near $x \approx 1.5$. This scenario gives rise to the described process. Going from instant (a) to (c), this arch gets weaker and stretches out due to the wall normal velocity pulling the arch towards the centerline for $x \lesssim 1.5$ and towards the wall beyond this region. Eventually, a piece of this arch breaks off i.e. shed as shown in (d) near the location where the wall normal velocity changes sign.

The next stage of the process has to do with these fragments that are shed which get convected downstream faster than the primary TS structure. This can be seen in (e). This difference has to do with the fact that the velocity of the primary TS structure is dictated by the mean velocity at the critical layer while these fragments are closer to the centerline, where the streamwise velocity is higher. As these fragments are convected, they are simultaneously sheared by the strong mean shear near the wall which gives rise to the near-wall multilayered sheet seen in (f) between $x \approx 3$ and $x \approx 6$. The instant (f) is similar to (a), thus restarting the process just described i.e. quasi-cyclical. The time scale of the process is dictated by the dominant time scale of the attractor with TS critical layer mechanisms at its core. This process gets more pronounced as we move along this branch and the statistical intermittency described earlier corresponds to a structural intermittency due to the sheet shedding process excited by viscoelasticity.

To show this, figure 7.5 depicts the structural intermittency observed at $Wi = 11$. Snapshots shown are taken every 10 TU - the time scale at which we described the sheet shedding process at $Wi = 4$. The attractor goes from displaying a single sheet of polymer stretch as seen in (a) to strong multilayered sheets at the instant (j) and back.

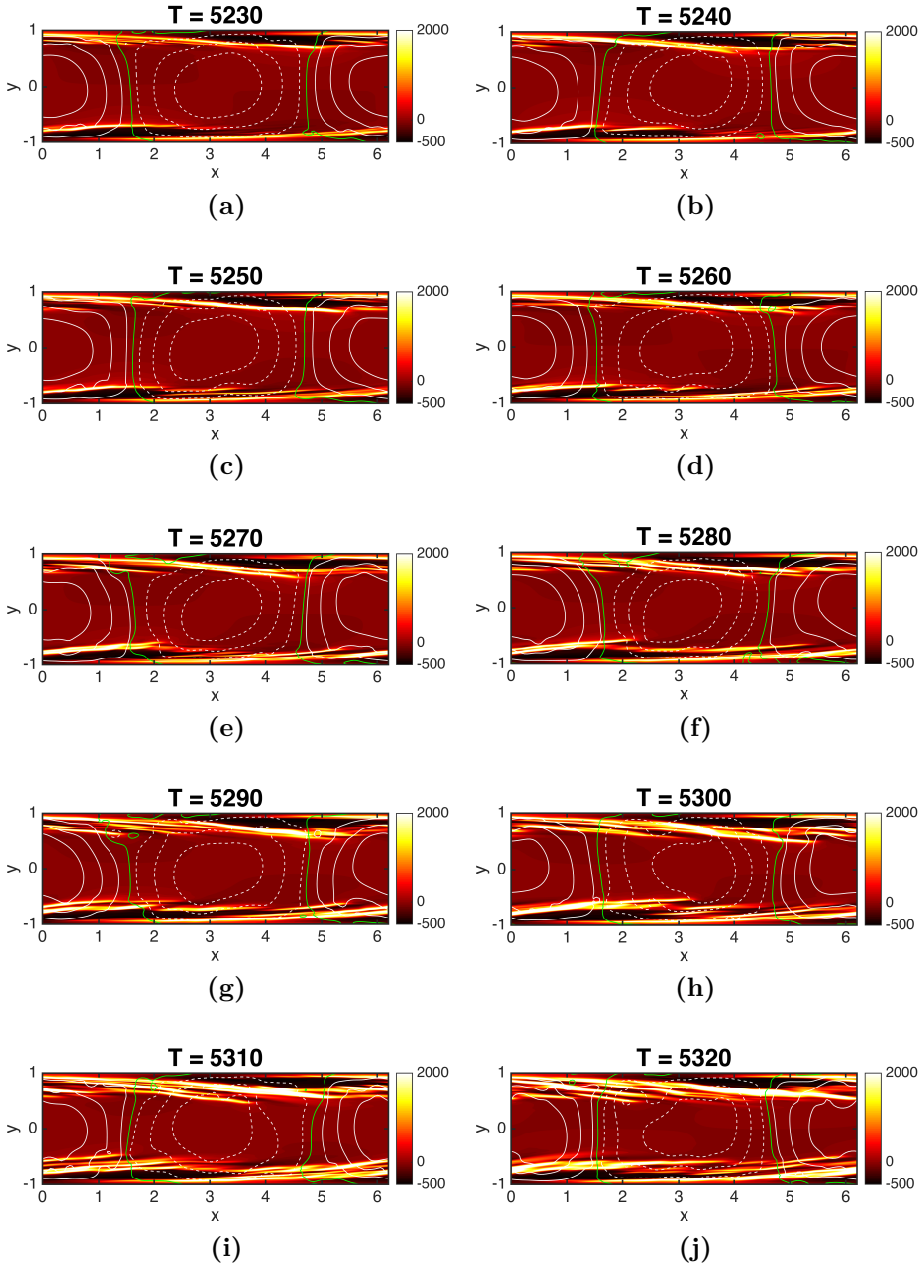

Figure 7.5: (a) - (j) are snapshots of the fluctuation structure of the attractor at $Wi = 11$. Snapshots are taken from T = 5230 to 5320 every 10 time units respectively. Same format as figure 7.4.

The observed steps of shedding - convecting - shearing now happens in a fashion that eventually gives rise to multilayered sheets. These near-wall sheets observed during

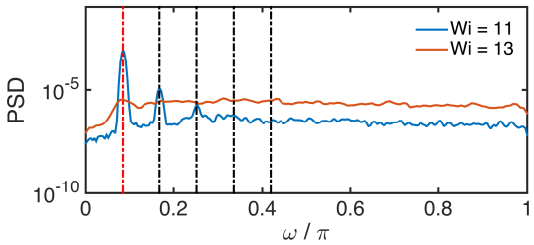

Figure 7.6: Power spectral density (PSD) of wall normal velocity at $y = \pm 0.8$ at the indicated Wi.

this intermittent process start to resemble those observed at EIT as described earlier. Beyond $Wi = 11$, these multilayered sheets take over the dynamics at $Wi = 12$ before turning into EIT at $Wi = 13$.

To build on this evidence linking the TS attractor (up to $Wi = 11$) and EIT (beyond 11), figure 7.6 shows the power spectral density of wall normal velocity at $y = \pm 0.8$ with the following observations holding true at other y locations. At $Wi = 11$ (blue), the spectrum is mainly composed of the fundamental TS frequency (red-dashed) and its two higher harmonics (black-dashed). This is slightly unsurprising as TS-like flow structures characterized by wall-normal velocity contour lines spanning the channel are a dominant feature of the attractor (evidenced by figure 7.5). Interestingly, the fundamental TS frequency (red-dashed) remains a prominent feature of the spectrum even at $Wi = 13$ (brown) in spite of the obvious structural differences with $Wi = 11$. This points at TS-like mechanisms dictating the intermittent processes even at EIT.

Looking at other statistics, figure 7.7 shows the evolution of mean profiles of streamwise velocity (figure 7.7a), Reynolds shear stress (figure 7.7b) and polymer shear stress (figure 7.7c) going from the Newtonian attractor to EIT. On increasing Wi, the mean velocity profiles get increasingly uplifted from Newtonian (red) to

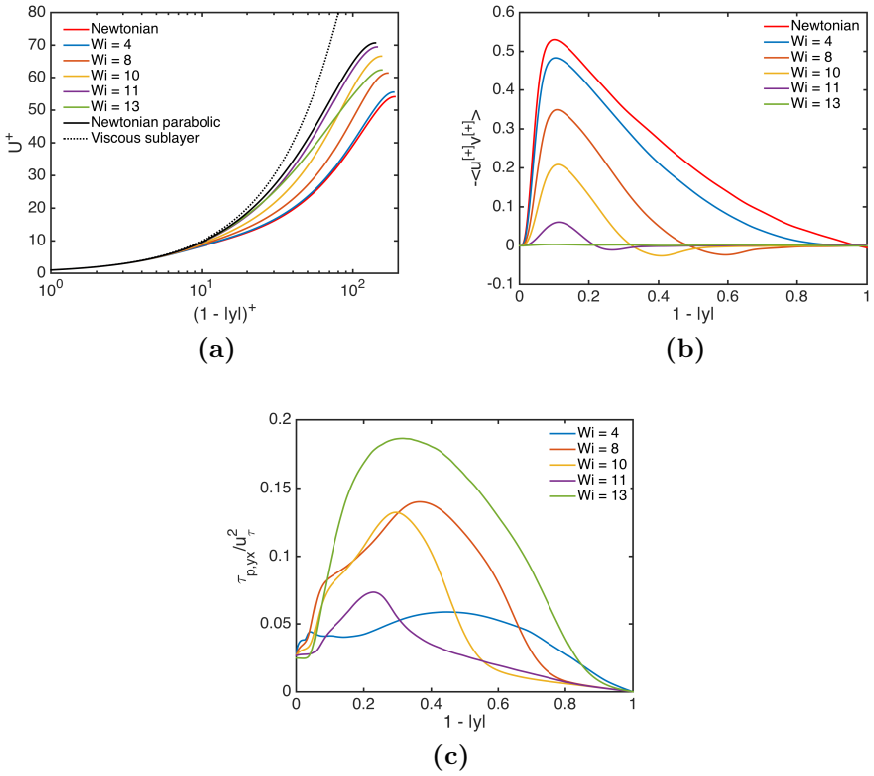

Figure 7.7: (a) Mean streamwise velocity profiles (b) Reynolds shear stress profiles and (c) polymer shear stress profiles of full space attractors. All profiles are shown as a function of distance from the wall $1 - |y|$.

$Wi = 11$ (purple) with the profile at $Wi = 4$ (blue) very similar to the Newtonian one. EIT at $Wi = 13$ (green) displays a profile in between Newtonian and $Wi = 11$. Turning to the Reynolds shear stress profiles, the Newtonian profile (red) displays a near-wall peak corresponding to the critical layer of the attractor. This points to a prominent role for critical layer kinematics in Reynolds shear stress production. Moving along the branch, the attractors continue to display this near-wall peak with a monotonic decrease in magnitude till $Wi = 13$ with negligible Reynolds shear stress. Past studies of EIT have also reported reported similar observations [Samanta *et al.*, 2013, Sid *et al.*, 2018, Shekar *et al.*, 2019]. While Reynolds shear stress dominates

over polymer shear stress at $Wi = 4$, the roles are completely reversed at EIT with polymer shear stress being the main source of turbulence generation. At $Wi = 11$, the above quantities are of similar magnitude thus indicating roles of equal importance in self-sustenance. Further, the peak polymer shear stress at EIT loosely aligns with the peaks at lower Wi. This hints at mechanisms originating from the TS attractor underlying the main source of turbulence production at EIT. Taken together, these results provide direct evidence of a connection between the TS attractor and EIT.

7.3.3 Relaxation oscillations to elastoinertial turbulence

The discussion so far has focussed on the attractor in full space. Here, we elaborate on the dynamical scenario underlying these observations by zooming in on the attractor in the shift-reflect (S-R) subspace. Any connection between the TS and EIT attractors ought to be most evident in this subspace. The origins of the EIT branch in full space coincides with the emergence of stable symmetric EIT at $Wi = 13$. This transition from the TS attractor to EIT happens over a narrow range of parameter space where the dynamics are most intermittent. Again, this is true in both the symmetric subspace and full space (further emphasizing that dynamics in the S-R space structure the full space dynamics; captures the bifurcation from TS to EIT). To further understand this, we now turn to the instantaneous $||\hat{\alpha}_{xx}||_2$ dynamics of the attractors in the symmetric subspace as shown in figure 7.8a.

$Wi = 12$ (purple) represents the intermediate case between TS and EIT where the attractor switches intermittently between two metastable states. For robustness sake, we have tried other initial conditions, all of which show the same behavior. The dynamics can spend O(1000) TU in each of these chaotic states before either bursting

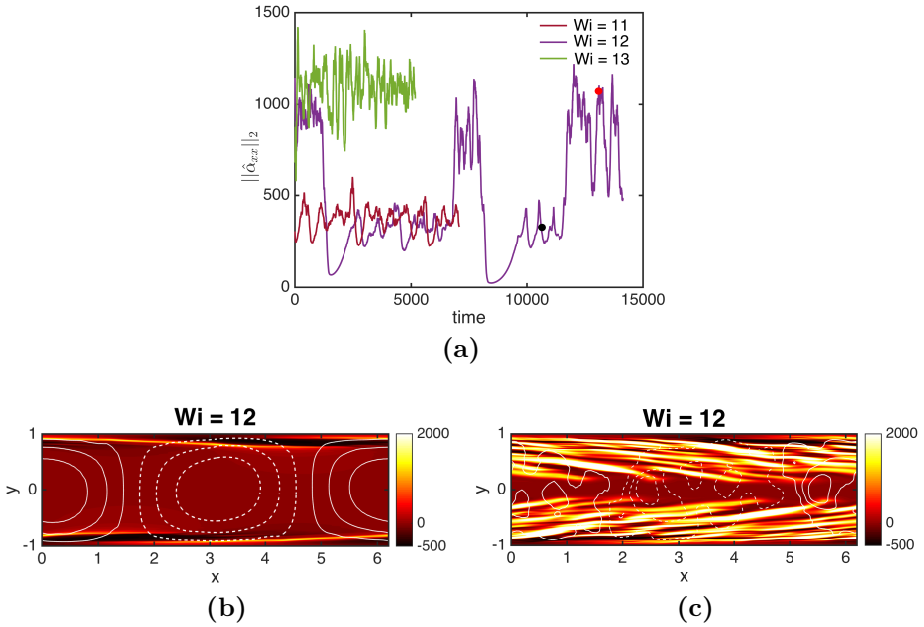

Figure 7.8: (a) Instantaneous $||\hat{\alpha}_{xx}||_2$ vs time at $Re = 10000$ in the TS shift-reflect symmetric subspace. (b) and (c) are snapshots of the fluctuation structure of the TS (instant indicated by the black circle) and EIT (red circle) metastable states respectively.

from or decaying onto the lower metastable state. The time scale characterizing these events are much faster than those seen on either metastable states. The lower metastable state displays values similar to the attractor at $Wi = 11$ (maroon) and the same can be said between the upper metastable state and EIT at $Wi = 13$ (green). Figures 7.8b and c are representative snapshots of the lower and upper metastable states respectively. It is clear to see that the lower metastable state corresponds to the extension of the TS attractor but is now unstable. This destabilization of the TS attractor coincides with the emergence of the upper metastable state which clearly resembles EIT and is a precursor to stable symmetric EIT at higher Wi. Such an intermittent destabilization of one attractor (TS here) in a narrow range of control parameter leading to a new attractor (EIT here) is typical of a dynamical system with multiple time scales with a pleated slow manifold and the possibility of rapid

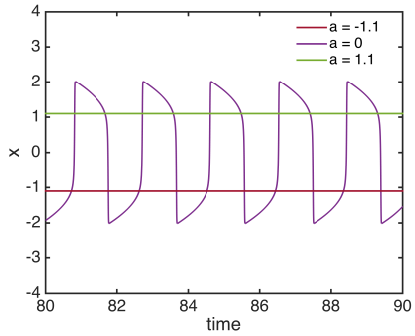

Figure 7.9: x-dynamics in van der-Pol-type system described by equations 7.6 and 7.7 for $\epsilon = 0.01$ at the indicated values of control parameter 'a'.

jumps between different, locally attracting, pleats [Guckenheimer, 2004].

In particular, we draw an analogy with the following van der-Pol-type system:

$$\dot{x} = \frac{1}{\epsilon}(y - (x^3/3 - x)), \tag{7.6}$$

$$\dot{y} = a - x \tag{7.7}$$

Here, 'a' is the control parameter of the system and ϵ determines the ratio of time scales between the x and y dynamics. At each value of a, there is a unique steady state $(x, y) = (a, a^3/3 - a)$. As $\epsilon \to 0$, this state is stable when $a < -1$ and $a > 1$, while in $-1 < a < 1$, there is a stable limit cycle – a relaxation oscillation that jumps rapidly between positive and negative values of x. Figure 7.9 shows the $x-$dynamics of the system for $\epsilon = 0.01$ at different values of a. For $a = -1.1$ (maroon) and $a = 1.1$ (green), initial conditions settle on the stable steady state $x = -1.1$ and $x = 1.1$, respectively. For $a = 0$ (purple), the system displays relaxation oscillations. The observations presented in this section taken in consideration with evidence of a link between TS and EIT are entirely consistent with a high-dimensional equivalent of such relaxation oscillations between TS and EIT metastable states at $Wi = 12$ which

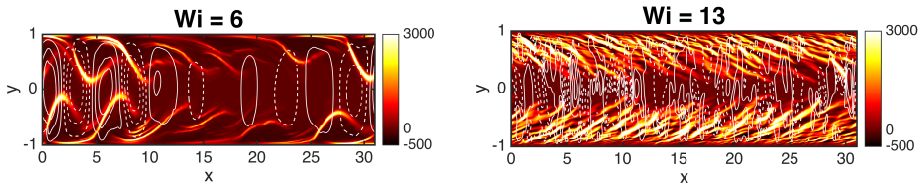

Figure 7.10: Snapshots of the attractor at $Re = 10000$ in a box of size $L_x = 31$ at the indicated Wi. Contour plots follow the same format as previous figures.

give rise to stable EIT at higher Wi.

7.3.4 Robustness in large spatial domains and very high polymer extensibility

Finally, we present results in other parameter regimes to portray the robustness of our observations in other parameter regimes. For each of the below scenarios, we look at snapshots of the attractor for different levels of viscoelasticity.

Large domain:

First, we consider results at $Re = 10000$ in a large domain of size $L_x = 31$ i.e. five times the domain size used in this manuscript. Snapshots of the attractor are shown in figure 7.10. At $Wi = 6$, the attractor displays a structure corresponding to five periods of the TS attractor in $L_x = 6.2$ with near-wall sheets and wall normal velocity across the channel. Further, we can see clear evidence of the sheet shedding process at play. Here, different parts of the domain can be at different stages of the process i.e. there is a spatio-temporal intermittency. For example, we see multilayered sheets near $x = 10$ and sheet shedding near $x = 25$. At $Wi = 13$, we see EIT with strong multilayered sheets of polymer stretch as we did for $L_x = 6.2$.

Very high extensibility:

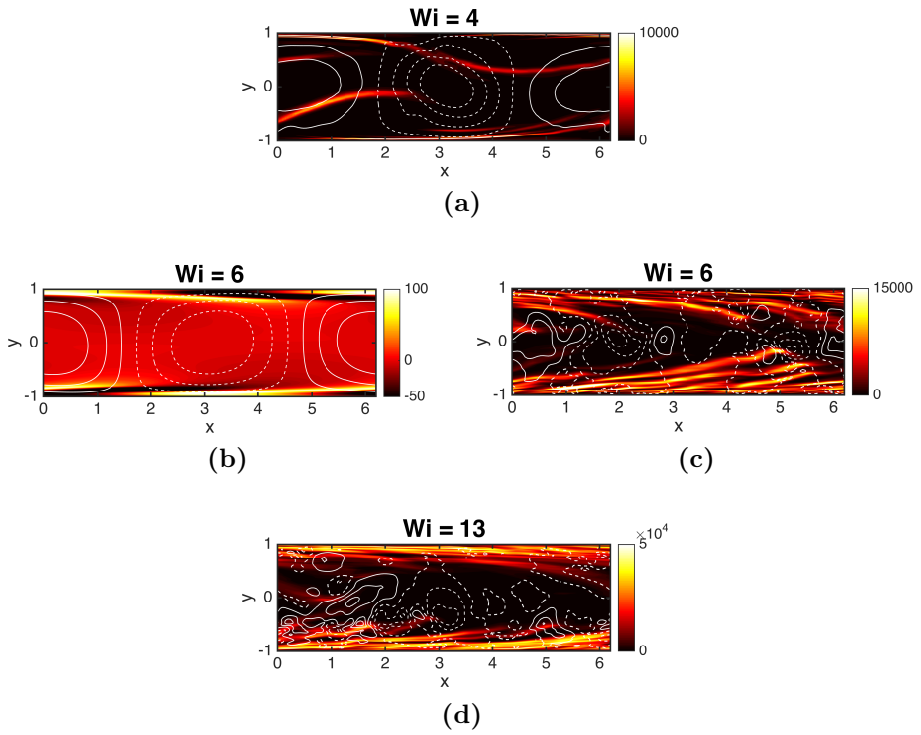

Figure 7.11: Snapshots of the attractor at $Re = 10000$ with $b = 100,000$. Same format as previous plots.

Now we consider the scenario at very high extensibility with $b = 100,000$ with other parameters remaining the same. This value of b corresponds better to high molecular-weight drag reducing polymers. Figure 7.11 depicts snapshots of the attractor for this case.

At $Wi = 4$, the attractor corresponds to the TS attractor in this parameter regime and displays the same characteristics as the attractor at lower extensibility. Further, the attractor continues to exhibit the sheet shedding process that leads to multilayered sheets of polymer stretch. This can be seen near $x = 4$ in the above snapshot. On increasing Wi, the TS attractor loses stability before giving rise to stable EIT. At $Wi = 6$, the dynamics alternate between TS and EIT metastable states as shown in figures 7.11b and c, respectively. This EIT metastable state can sometimes be

asymmetric and thus in agreement with the observations at $Wi = 12$, $b = 6400$. These results are consistent with relaxation oscillations from TS to EIT with the bifurcation happening around $Wi \approx 6$ at this value of extensibility. At $Wi = 13$, we observe EIT which continues to display near-wall sheets of polymer stretch as opposed to the centerline structures observed by Dubief *et al.* [2020]. At the same value of $b = 100,000$ considered here, they report centerline-symmetric "arrowhead" structures in the first normal stress difference at very high levels of viscoelasticity. For $Re \sim O(1000)$, they observe such structures either intermittently or as steady traveling waves at $Wi \sim O(100)$.

7.4 Conclusion

This study describes the evolution of the Tollmien-Schlichting (TS) attractor in $Re - Wi$ parameter space and its relationship to elastoinertial turbulence (EIT) using simulations of 2D channel flow of a very dilute polymer solution. On increasing Re from 3000 to 10000, the viscoelastic branch of the TS attractor (VNTSA) joins up with the Newtonian branch (NNTSA) through a coil-stretch transition when the local Wi at the hyperbolic stagnation point exceeds $\frac{1}{2}$. The structure evolves from localized striations of polymer stretch to extended sheets almost two orders of magnitude stronger. Accompanying this transition is the appearance of a new process coined the sheet shedding process. We identify the different stages of this process namely shedding, convecting and shearing that can generate multilayered sheets of polymer stretch. At $Re = 10000$, we describe how viscoelasticity excites the sheet shedding process which gets more pronounced with Wi eventually destabilizing the TS branch

and giving rise to EIT. Using computations in a shift-reflect symmetric subspace, we present evidence of relaxations oscillations underlying the transition from the TS attractor to EIT. Finally, we saw the persistence of these results in large domains and very high extensibility. Taken together, we identify a path to EIT originating from Newtonian TS critical layer mechanisms. Similar processes could potentially govern the dynamics of EIT in the very dilute regime.

Chapter 8

Elastoinertial turbulence in other parameter regimes

In this chapter, we expand on the structure of EIT in other parameter regimes and further elucidate mechanisms playing a role using analysis techniques presented in chapters 5 - 7.

8.1 Low Reynolds number

Experiments of viscoelastic transition in pipes and channels highlighted in chapter 2 report observations of early transition to a chaotic flow state at Re O(500) - much lower than the value where Newtonian turbulence can be sustained. Simulations by Samanta *et al.* [2013] pin down these observations to the appearance of EIT.

Results covered so far focus on Re from 1500-10000 and establish a role for Tollmien-Schlichting mechanisms at EIT. In this section, we present results at very low Re and expand on mechanisms in this region of parameter space. Starting from

$Re = 3000$, $Wi = 13$, we trace the evolution of 2D EIT on decreasing Re using DNS as detailed in chapter 3. We fix $\beta = 0.97$, $b = 6400$, $L_x = 5$. A resolution of $N_x = 131$, $N_y = 602$ is used for these computations.

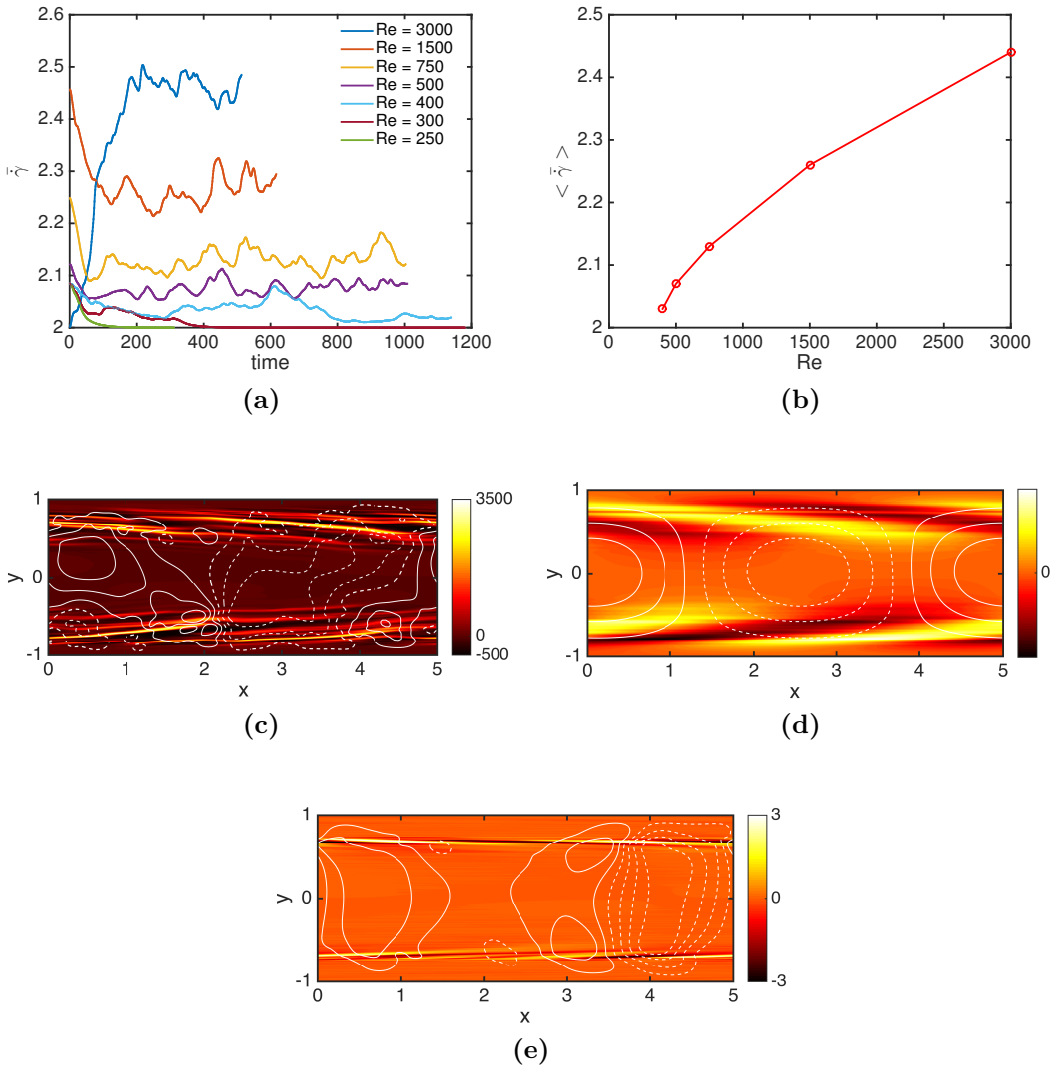

Figure 8.1: a - Mean wall shear rate vs time for different Reynolds numbers. b- Bifurcation diagram of time-averaged mean wall shear rate vs Re obtained from a. c - Snapshot of the fluctuation structure of EIT at $Re = 500$. d - Phase-aligned and averaged fluctuation structure of EIT at $Re = 500$ when projected onto the peak spectral content ($N_x = 1$). e - Snapshot of the LBA at $Re = 250$.

Figure 8.1a shows the mean wall shear rate dynamics of the attractor. Chaotic

EIT dynamics can be sustained down to $Re \approx 400$ (light blue) below which initial conditions decay to a weak chaotic flow with dynamics about the laminar value - 2 (maroon, light green). We refer to this week chaotic flow state as the lower branch attractor (LBA) and draws a parallel to the observations of the VNTSA in chapter 6.

A bifurcation diagram for 2D EIT is shown in figure 8.1b using the time-averaged mean wall shear rate as the measure. The EIT branch displays a monotonic decrease in this measure before losing existence at finite amplitude at $Re = 400$. This is typical of a saddle-node bifurcation. Evidence of this can be in figure 8.1a - $Re = 300$ (maroon) displays transient EIT dynamics from T = 150-350 before eventual decay.

We now turn to the structure of EIT and LBA to shed insights into the underlying mechanisms at very low Re. Figure 8.1c is a representative snapshot of EIT at $Re = 500$. We can see that EIT at very low Re continues to display sheets of polymer stretch localized near wall with wall-normal velocity fluctuations that span the channel. To build on this, figure 8.1d shows the average phase-matched structure projected onto $N_x = 1$ which clearly resembles the TS mode. This is evidence of TS-like critical layer mechanisms playing a role even in this parameter regime. This is reflected in the structure of the LBA as shown in 8.1d at $Re = 250$ - striations of polymer stretch localized near wall with wall-normal velocity across the channel being a prominent feature.

8.2 Minimal flow unit of EIT

The concept of a minimal flow unit (MFU) was first introduced by Jiménez and Moin [1991] to isolate the basic self-sustaining structures of wall-bounded Newtonian turbulence. They did so by minimizing the size of the computational domain down to smallest size that could sustain turbulence. The statistics of MFU turbulence were in good agreement with experiments and captured the basic near-wall coherent structures of Newtonian turbulence i.e quasistreamwise vortices and streamwise velocity streaks. Further, they were able to identify the fundamental regeneration cycle of turbulence. In this section, we carry forward this this idea to identify the MFU of 2D EIT at $Re = 3000$, $Wi = 13$ by varying the streamwise box size (L_x). As with our other results, we fix $\beta = 0.97$, $b = 6400$. For DNS, the number of grid points in the wall-normal direction (N_y) is fixed at 302 and N_x is varied based on L_x - 79 at $L_x = 5$ to 31 at $L_x = 1.25$. Resolution tests on doubling this resolution yielded similar results.

Figure 8.2a shows the mean wall shear rate dynamics of 2D EIT as L_x is reduced. Sustained chaos can be maintained down to $L_x = 1.25$ (red) below which we observe transient chaos and eventual decay at $L_x = 1.15$ (dark blue). The dynamics of EIT at these lower box sizes display similar values to $L_x = 5$ (light blue) albeit with stronger fluctuations. $L_x = 1.25$ thus represents the MFU of 2D EIT in this parameter regime and thus contains the basic ingredients necessary to sustain EIT. Figures 8.2b and c are representative of the structures observed at $L_x = 5$ and 1.25 respectively. EIT in the MFU domain continues to display strong sheets of polymer stretch that start out from near the wall with wall normal velocity structures that can extend across the channel height. Thus, at first glance, the mechanisms identified in previous chapters

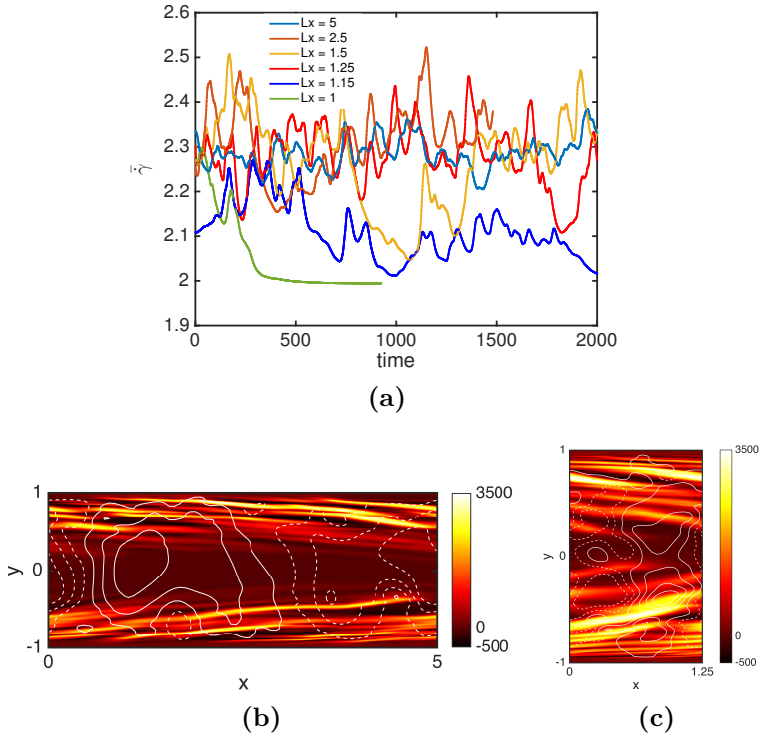

Figure 8.2: a - Mean wall shear rate dynamics vs streamwise box size (L_x). b and c are snapshots of the fluctuation structure of EIT at $L_x = 5$ and 1.25 respectively.

seem to be relevant even in the MFU domain.

To quantify the relevance of the MFU results, figure 8.3 compares the statistics of the MFU attractor with $L_x = 5$. Keeping with the observations of Jiménez and Moin [1991], MFU EIT displays very similar first order statistics with EIT in larger domains.

At $L_x = 5$, when EIT at $Wi = 13$ was used as an initial condition for a run at $Wi = 12$, the dynamics eventually landed on the VNTSA - a baby version of EIT (chapter 6). Understanding the mechanisms sustaining the VNTSA provided a promising route to understand the mechanisms at EIT. We detail a similar experiment here, now starting from MFU EIT at $Wi = 13$. Figure 8.4a shows the temporal

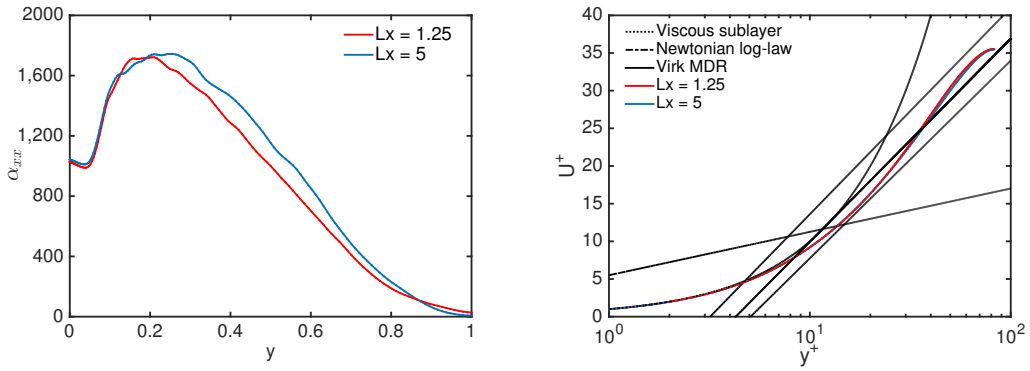

Figure 8.3: a, b - Profiles of mean α_{xx} and U^+, respectively as a function of distance from the wall. Here, y = 0 is at the wall and y = 1 corresponds to the centerline.

evolution of mean wall shear rate at $Wi = 12$ starting from initial conditions taken from EIT at $Wi = 13$. All three runs display transient chaos before eventually decaying to the lower branch attractor (LBA) with weak chaotic fluctuations about the laminar value (2). A snapshot of the structure of the LBA in the MFU domain is shown in figure 8.4b. The LBA displays highly localized striations of polymer stretch near the wall and a mixture of near-wall localized and extended wall-normal velocity structures. This points to critical layer mechanisms rooted at these near-wall modes sustaining the dynamics of the LBA.

Finally, we turn to linear analyses for potential candidates that could underlie the LBA in the MFU domain. Figures 8.4c and d show the results of linear stability and resolvent analysis, respectively for this parameter set. From the eigenspectrum (figure 8.4c), it is clear to see that all modes have $c_i < 0$ i.e the laminar state is linearly stable. Not just that, the slowest decaying mode belongs to the continuous spectrum and no clear candidate sticks out from spectrum. This is reflected in figure 8.4d - the resolvent norm remains pretty flat on varying the wavespeed of forcing

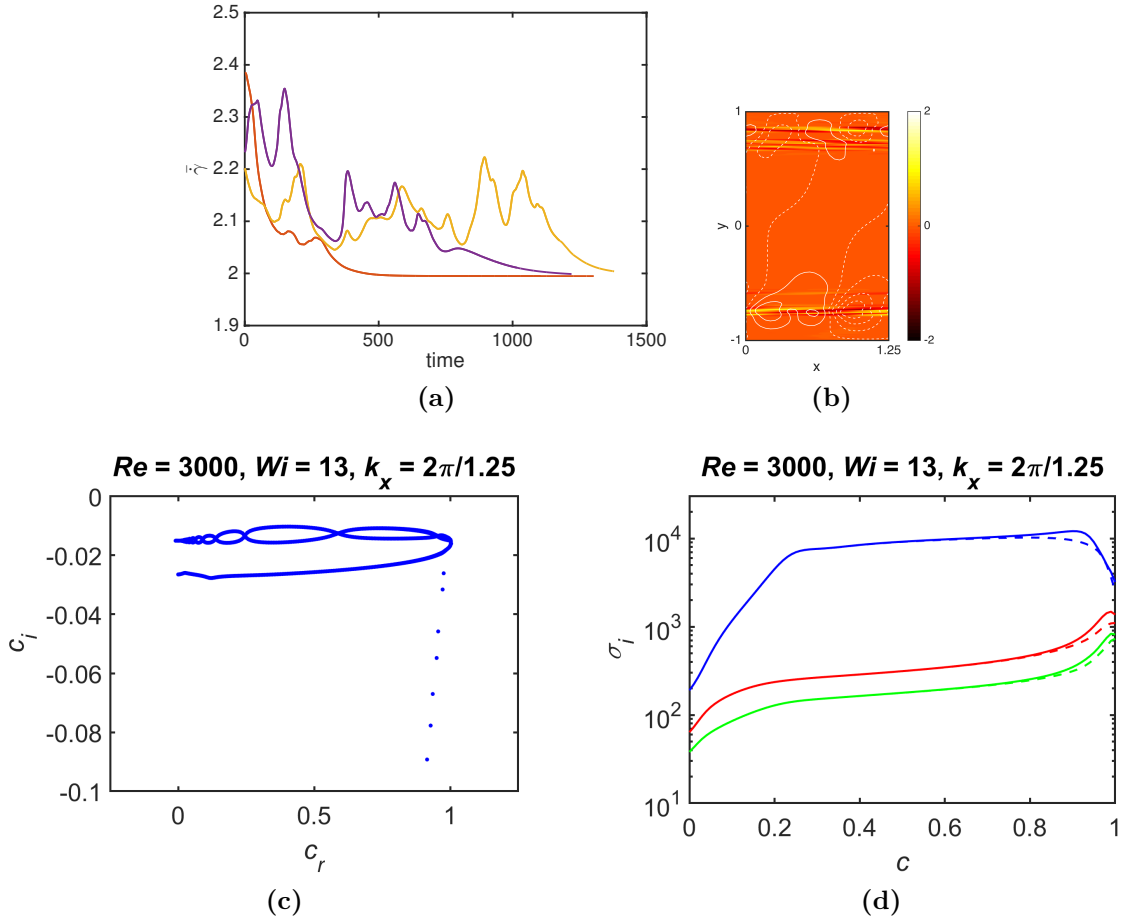

Figure 8.4: a - Mean wall shear rate vs time for three different initial conditions taken from EIT at $Wi = 13$. b - Fluctuation structure of the LBA. c - Eigenspectrum from linear stability analysis for this parameter set. d - Resolvent norm (σ) as a function of wavespeed of forcing (c). Here, blue corresponds to the fundamental period; red and green correspond to higher spatial harmonics.

(c) with no clear candidate being strongly amplified over the others. These results point to nonlinear mechanisms coming into existence at finite amplitude to make up the LBA as opposed to a subcritical bifurcation off the laminar state that forms the nonlinear TS branch in larger domains. Such solution branches could go on to join up with EIT as seen in chapters 6 and 7.

8.3 3D EIT at higher Reynolds number

In chapter 5, we described a path to 3D EIT at $Re = 1500$ that involves the relaminarization of Newtonian turbulence followed by a reentrant transition to EIT on increasing Wi. Mechanisms at EIT were thus disconnected from Newtonian mechanisms for this parameter set. In this section, we detail a continuous path to EIT at $Re = 3000$ on increasing Wi starting from Newtonian turbulence. We further probe into mechanisms using an extended version of Karhunen-Loève (KL) decomposition as described in Wang *et al.* [2014a] to extract the most energy containing structures underlying the dynamics. In particular, we are interested in probing the question of whether any mechanisms of Newtonian origins persist at high viscoelasticity as we move towards higher Re.

We fix $\beta = 0.97$, $b = 6400$. The computational domain has dimensions $L_x = 10$, $L_y = 2$ and $L_z = 5$. A resolution of $N_x = 109$, $N_y = 106$ and $N_z = 109$ is used for results shown below with mesh convergence tests at $N_x = 157$, $N_y = 150$ and $N_z = 157$ yielding similar results.

Figure 8.5a summarizes the evolution of the normalized friction factor as a function of Wi. Starting from Newtonian turbulence, a steep decrease in the friction factor can be seen till $Wi = 15$. Beyond that, the friction factor displays a plateau between $Wi = 15$ and 25 before eventually landing on EIT at $Wi = 50$ accompanied by a saturating friction factor. A similar continuous path to EIT was observed in pipes by Choueiri *et al.* [2018] on increasing polymer concentration at $Re = 5200$.

In this intermediate regime between $Wi = 15$ and 25, an interesting mixture of structures can be seen. Snapshots of the structures seen at $Wi = 20$ are shown in figures 8.5b to e. The snapshot for b and d are from an instant of low turbulence

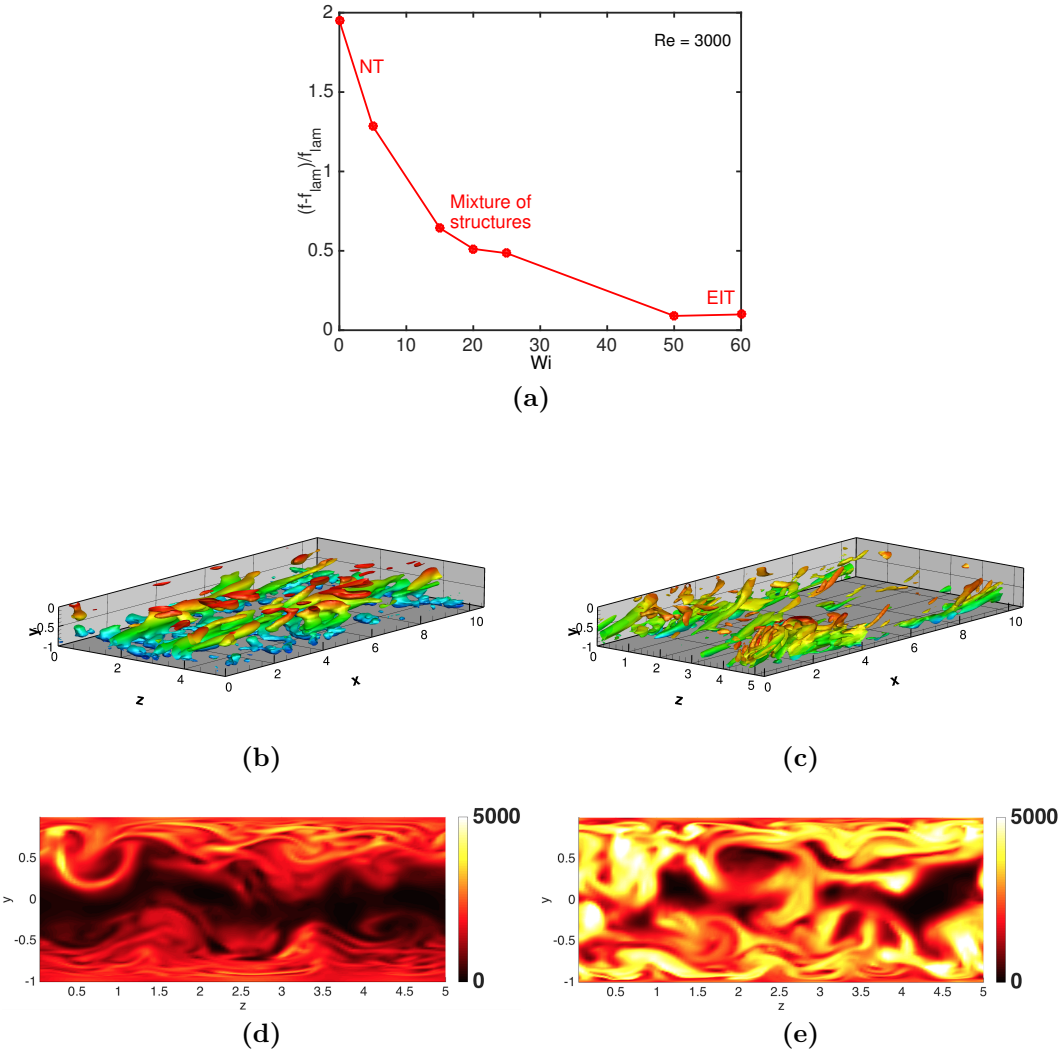

Figure 8.5: a - Normalized friction factor as a function of Wi at $Re = 3000$. b and c are isosurface of vortex strength Q color coded based on distance from the wall - blue near the wall and red near the centerline. For b, $Q = 0.0033$ and c, $Q = 0.07$. d and e are contours of polymer stretch $tr(\boldsymbol{\alpha})$ on a $y - z$ plane.

activity ("hibernation"); c and e are taken from an instant of high turbulence activity ("active"). During hibernation (8.5b), the near-wall region of the flow is dominated by spanwise oriented structures (blue) characteristic of EIT. Further from the wall, streamwise vortices are the prominent feature which extend close to the centerline. A reflection of the described structure can be seen in the polymer stretch contour (8.5d)

- near-wall sheets with plumes closer to the centerline. The active flow structure (8.5c) is mainly comprised of streamwise vortices which give rise strong plumes of polymer stretch (8.5e).

Together, we get a sense of the fundamental cycle of intermittency for turbulence regeneration in this regime which seemingly involves a coupling between EIT-like structures and Newtonian-like quasistreamwise vortices. Very recent computations by Zhu *et al.* [2021] also observe an intermittent process in drag-reduced turbulence involving quasi-2D structures with critical layer characteristics and 3D quasistreamwise structures. Similar mixtures of structures have also been reported in Sid *et al.* [2018], Choueiri *et al.* [2018] but have not been analyzed in this context.

Figure 8.6 shows the evolution of mean statistics as Wi is increased. The velocity profile (8.6a) goes from the Newtonian log-law profile for Newtonian turbulence (pink) to a profile within the 95% confidence interval of Virk MDR at $Wi = 50$ (EIT, green). At low $Wi = 5$ (yellow), the velocity profile remains parallel to the Newtonian profile but slightly uplifted. For the intermediate cases at $Wi = 20$ and 25 (blue and purple), the profiles no longer display the Newtonian log-law and start to tilt towards the MDR profile.

Turning to the Reynolds shear stress in figure 8.6b, we see a monotonic drop in the profile from Newtonian (pink) to $Wi = 25$ (purple). Further, the peak value moves away from the wall which is indicative of a thickened buffer layer. This ties back to the mixture of structures observed in this intermediate regime. Interestingly, there is a complete collapse of the profile at EIT at $Wi = 50$ (green). This is strong evidence of disappearing Newtonian self-sustenance mechanisms between $Wi = 25$ and 50 as viscoelastic mechanisms start to take over.

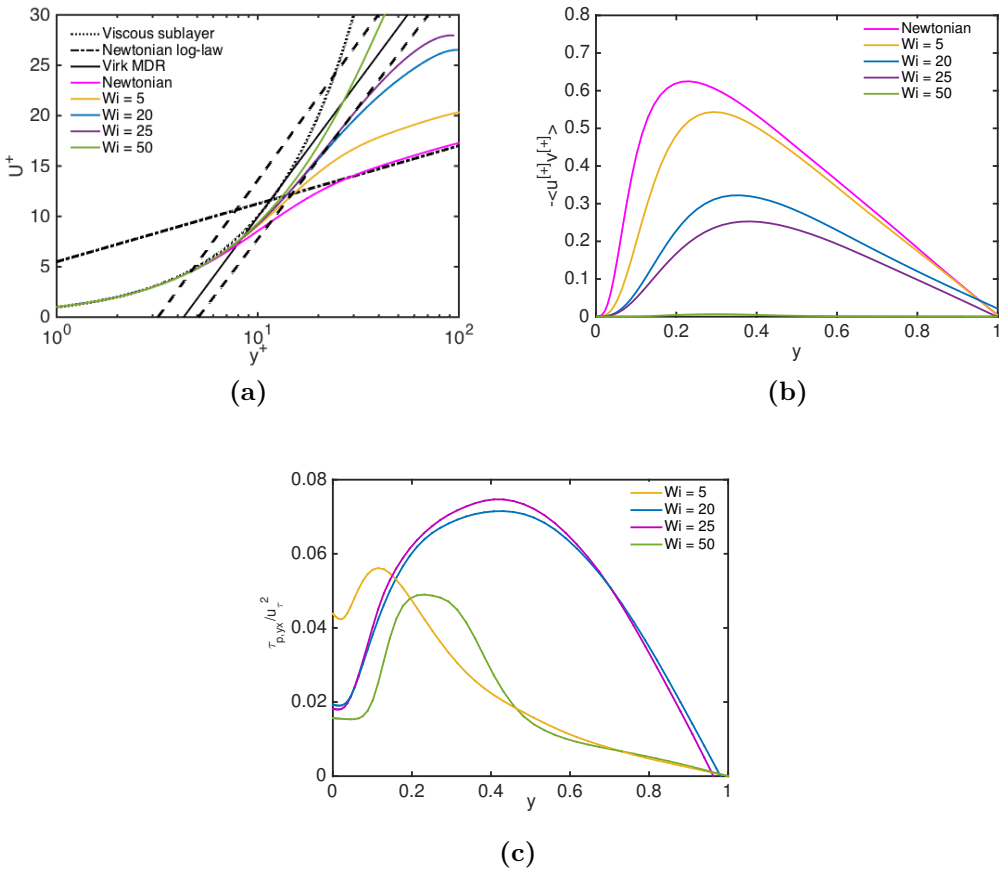

Figure 8.6: Mean profiles of streamwise velocity (a), Reynolds shear stress (b) and polymer shear stress (c) as a function of distance from the wall (y).

A similar storyline is reflected in the polymer stress profiles in figure 8.6c. At low $Wi = 5$ (yellow), we see a peak near the wall due the quasistreamwise vortices. This gets moved away from the wall as EIT-like structures take over the near-wall region for the intermediate cases (blue, purple). This gives rise to a profiles spread across the domain comprising of near-wall contributions due to EIT-like structures. Beyond $Wi = 25$, the quasistreamwise vortices disappear thus leaving behind the EIT structures that make up the near-wall region giving rise a profile that peaks near the wall (green).

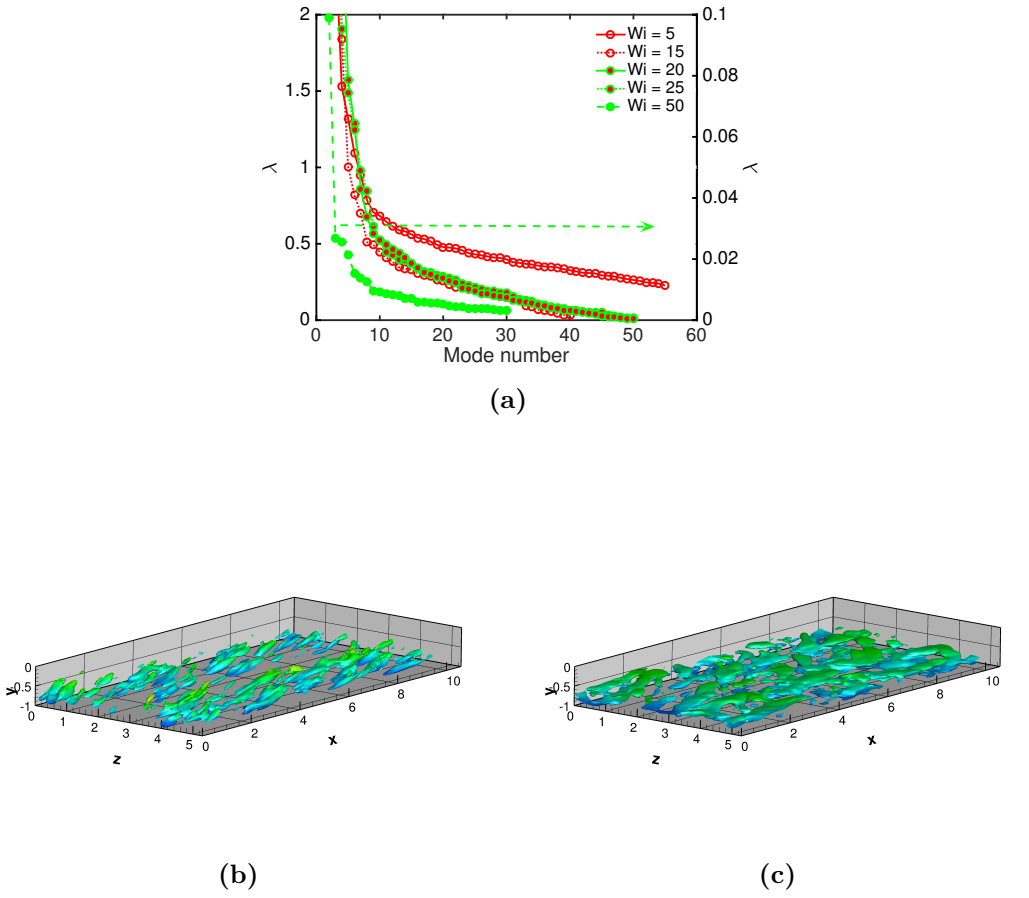

Figure 8.7: a - Eigenspectrum from Karhunen-Loève (KL) decomposition for different Wi. b and c are isosurfaces of vortex strength Q for $Wi = 5$ and 50 respectively.

Finally, we turn to a data-driven approach - the Karhunen-Loève (KL) decomposition to uncover the most energetic structures that govern the dynamics with increasing Wi. The result of this analysis is a set of eigenmodes and their corresponding eigenvalues which signify the energy content in the modes. A time series of 50 snapshots spread across 1000 TU is used for the results shown in figure 8.7.

Figure 8.7a shows the leading eigenvalues going from $Wi = 5$ to 50. A sharp drop in the eigenvalues is observed from $Wi = 5$ to $Wi = 15$. Between 15 and 25 the leading eigenvalues display very similar values, perhaps due to the mixture of

structures observed in this regime. At EIT ($Wi = 50$), the eigenvalues are an order of magnitude lower and thus shown using a separate axis.

This marked difference between $Wi = 5$ and $Wi = 50$ is reflected in the structure of the dominant modes. The leading modes at $Wi = 5$ display streamwise rolls that are commonly referred to as "roll modes" in the literature. The vortex structure of the leading roll mode at $Wi = 5$ is shown in figure 8.7b. Figure 8.7c shows the structure of the leading mode for EIT which displays a sheet-like structure. These "sheet modes" make up the leading modes at EIT and are thus indicative of different self-sustenance mechanisms underlying EIT in this parameter regime. At intermediate Wi, the leading modes are either roll modes or "mixture modes" with a mixture of structures.

8.4 Conclusions

In this chapter, we extend our understanding of mechanisms sustaining EIT in different parts of parameter space. At very low Re, EIT continues to display sheets of polymer that are localized near the wall. The phase-aligned structured bears strong resemblance to the TS mode and is indicative of TS-like mechanisms underlying the dynamics. In section 8.2, we identified the MFU of EIT which displayed very similar structures and first order statistics to EIT in extended domains. We also saw evidence of a lower branch attractor (LBA) with a critical layer structure and no obvious ties to linear modes. This is indicative of nonlinear mechanisms coming into existence at finite amplitude to make up the LBA. Finally, in section 8.3, we describe a continuous path to EIT on increasing Wi from Newtonian turbulence. At intermediate

Wi, the attractor displayed a mixture of structures with EIT-like near wall structures and streamwise vortices closer to the centerline. Using the Karhunen-Loève (KL) decomposition, we identified the most energetic structures governing the dynamics - roll modes at low *Wi* and sheet modes at EIT. This taken in consideration with statistical evidence points to mechanisms unrelated to Newtonian underlying the dynamics of 3D EIT even at this higher *Re*.

Chapter 9

Conclusions and future work

The addition of minute quantities of long chain polymer molecules can lead to a substantial reduction of friction drag in turbulent flows, thereby yielding a much higher flow rate for a given pressure drop [Toms, 1949, 1977, Virk *et al.*, 1970]. Up to 80% reduction in friction losses has been achieved in applications that involve the transportation of fluids through closed geometries like pipes or channels. Despite its widespread applications, a complete fundamental understanding of polymer drag reduction remains an outstanding challenge - one that has motivated decades of research. Perhaps the biggest mystery on the forefront of researchers minds is the upper limit on the degree of drag reduction, called the Maximum Drag Reduction (MDR) asymptote [Virk *et al.*, 1970]. Fundamental answers to this mystery can potentially unlock flow control schemes that achieve complete relaminarization and also motivate the design of additive-free control schemes that imitate the effects of polymer molecules.

Recent experiments and simulations [Samanta *et al.*, 2013, Dubief *et al.*, 2013,

Sid *et al.*, 2018, Choueiri *et al.*, 2018] strongly suggest that turbulence at MDR has structure very different from Newtonian, denoting it as elastoinertial turbulence (EIT). Studies have shown that EIT displayed tilted sheets of polymer stretch with weak spanwise-oriented flow structures perpendicular to the flow direction - a sharp contrast to the flow-oriented quasistreamwise vortex structure that makes up inertia-driven Newtonian turbulence. Remarkably, EIT was shown to display a friction factor scaling that approached the MDR scaling and negligible Reynolds shear stress - a common trait of past MDR studies [Warholic *et al.*, 1999, Ptasinski *et al.*, 2001]. This pointed to the possibility that MDR was a characteristic of EIT rather than a modified version of Newtonian turbulence. This has ignited a new thrust in the field to uncover the underlying mechanisms sustaining EIT - a direction that can potentially unearth new answers into polymer-flow interactions that underpin the mystery of MDR. We use direct numerical simulations of flowing dilute polymer solutions modeled using the FENE-P model to shed fundamental insights into the inner workings of EIT.

In chapter 4, we introduce the notion of a coherent structure in the context of Newtonian turbulence. We further used ideas from dynamical systems theory to understand the behavior of one such coherent motion - a hairpin vortex - by finding nonlinear self-sustained exact coherent states (ECS).

We translate this idea to uncover a prominent coherent motion in EIT in chapter 5. We show that EIT at low Re has strongly localized stress fluctuations, suggesting the importance of critical layer mechanisms in its origin. These fluctuations strongly resemble the most slowly decaying structures from linear stability analysis, as well as the most strongly amplified disturbances as determined by resolvent analysis of the linearized equations. Furthermore, the Kelvin cat's-eye kinematics found in the

critical layer region of self-sustained nonlinear TS waves generate sheetlike structures in the stress field that resemble those observed in EIT.

Building on these observations, in chapter 6 we detail the bifurcation scenario of nonlinear self-sustaining TS waves and their ties to 2D EIT. We report the existence of a new attractor that is based on the viscoelastic linear Tollmien–Schlichting (TS) mode and is nonlinearly sustained by viscoelastic stresses. We denote this as the viscoelastic nonlinear Tollmien–Schlichting attractor (VNTSA). At the parameters considered here, this solution branch is not connected to the Newtonian branch of nonlinear self-sustained TS waves. In a domain of dimensionless length 5, this solution comes into existence at finite but very small amplitude when Wi $\geq$ 6, increasing in amplitude until Wi $\approx$ 49, where it loses existence again. At higher Wi, initial conditions corresponding to this solution branch at lower Wi evolve into EIT and joins up with EIT through an unstable branch found using edge-tracking. Taken together, these results suggest that, at least in the parameter range considered here, the bypass transition leading to EIT is mediated by nonlinear amplification and self-sustenance of perturbations that excite the TS mode.

In chapter 7, we describe the evolution of the Tollmien-Schlichting (TS) attractor in $Re - Wi$ parameter space and its relationship to elastoinertial turbulence (EIT). On increasing Re from 3000 to 10000, the viscoelastic branch of the TS attractor (VNTSA) joins up with the Newtonian branch (NNTSA) through a coil-stretch transition when the local Wi at the hyperbolic stagnation point exceeds $\frac{1}{2}$. The structure evolves from localized striations of polymer stretch to extended sheets almost three orders of magnitude stronger. Accompanying this transition is the appearance of a new process coined the sheet shedding process. We identify the different stages of

this process namely shedding, convecting and shearing that can generate multilayered sheets of polymer stretch. At $Re = 10000$, we describe how viscoelasticity excites the sheet shedding process which gets more pronounced with Wi eventually destabilizing the TS branch and giving rise to EIT. Using computations in a shift-reflect symmetric subspace, we present evidence of a Shilinikov homoclinic bifurcation underlying the transition from the TS attractor to EIT. Finally, we saw the persistence of these results in large domains and very high extensibility. Taken together, we identify a path to EIT originating from Newtonian TS critical layer mechanisms and provide strong evidence for a role for such mechanisms at EIT.

Finally, in chapter 8, we extend our understanding of mechanisms sustaining EIT in different parts of parameter space. At very low Re, EIT continues to display sheets of polymer that are localized near the wall. The phase-aligned structured bears strong resemblance to the TS mode and is indicative of TS-like mechanisms underlying the dynamics. In section 8.2, we identified the minimal flow unit (MFU) of EIT which displayed very similar structures and first order statistics to EIT in extended domains. We also saw evidence of a lower branch attractor (LBA) with a critical layer structure and no obvious ties to linear modes. This is indicative of nonlinear mechanisms coming into existence at finite amplitude to make up the LBA. Finally, in section 8.3, we describe a continuous path to EIT on increasing Wi from Newtonian turbulence. At intermediate Wi, the attractor displayed a mixture of structures with EIT-like near wall structures and streamwise vortices closer to the centerline. Using the Karhunen-Loève (KL) decomposition, we identified the most energetic structures governing the dynamics - roll modes at low Wi and sheet modes at EIT. This taken in consideration with statistical evidence points to mechanisms

unrelated to Newtonian ones underlying the dynamics of 3D EIT at this higher Re.

Taken together, we have worked our way towards a mechanistic picture of the polymer-flow interactions that govern EIT. Having said this, additional questions need answering before we can bridge the gap between our current results and a complete understanding of MDR. Detailed below are some avenues of future efforts.

Effect of three-dimensionality: Real world turbulent drag reduction experiments are three-dimensional (3D) so an important extension of the above results is studying the effect of three-dimensionality. A recent study, Xi [2019], bring out some important differences between 2D and 3D EIT at high Wi. While 3D EIT displays a saturating friction factor with Wi, 2D EIT displayed a monotonic increase. Adding to this statistical difference, the authors also note the appearance of weak streamwise vortex structures at very high Wi (~ 400) for 3D EIT. These observations hint at new mechanisms coming into existence with 3-dimensionality and could be key to the saturating friction factor at MDR. It is well known that Newtonian Tollmien-Schlichting waves are unstable to 3D perturbations. Understanding the effect of viscoelasticity on this 3D breakdown could be the starting point of mechanisms at MDR. Lee and Zaki [2017] look into this problem at low Wi (up to 10). Carrying forward a similar analysis to higher Wi could be a starting point moving forward.

Mechanisms at high *Re*: One of the well known effects of polymer additives is the suppression of quasistreamwise vortices found in the near-wall region of turbulent flows. This effect has been well studied over the years and has been attributed to being the reason behind drag reduction. These vortices are the main flow structures that dominate the flow at transitional Re ($\mathrm{O}(10^3 - 10^4)$). As we move to higher, more industrially relevant Re ($\mathrm{O}(10^6 - 10^7)$), it is well known that the turbulent

boundary layer develops multi-scale features ranging from near-wall structures to structures on the scale of the boundary layer. The effect of polymer across these different scales is still an open question. While performing direct simulations at these Re may be computationally out of reach, perhaps a good starting point would be to study the effect of viscoelasticity on exact solutions that capture this multi-scale structure. Stone *et al.* [2002], Li *et al.* [2006b] sketch the bifurcation behavior with viscoelasticity of a solution branch with a quasistreamwise structure and carrying forward a similar analysis to more complicated solutions could potentially unearth new mechanisms that are important at MDR.

Bibliography

[1] Adrian, R. J. (2007). Hairpin vortex organization in wall turbulence. *Phys. Fluids*, 19(4):041301.

[2] Batchelor, G. K. (1970). The stress system in a suspension of force-free particles. *J. Fluid Mech.*, 41(3):545–570.

[3] Bird, R. B., Curtiss, C. F., Armstrong, R. C., and Hassager, O. (1987). *Dynamics of Polymeric Liquids: Volume 2. Kinetic Theory*, volume 2. Kinetic Theory. Wiley-Interscience, New York, 2 edition.

[4] Brand, E. and Gibson, J. F. (2014). A doubly-localized equilibrium solution of plane Couette flow. *J. Fluid Mech.*, 750:R3.

[5] Chandra, B., Shankar, V., and Das, D. (2018). Onset of transition in the flow of polymer solutions through microtubes. *J. Fluid Mech.*, 844:1052–1083.

[6] Chantry, M., Willis, A. P., and Kerswell, R. R. (2014). Genesis of Streamwise-Localized Solutions from Globally Periodic Traveling Waves in Pipe Flow. *Phys. Rev. Lett.*, 112(16):164501.

[7] Chaudhary, I., Garg, P., Shankar, V., and Subramanian, G. (2019). Elasto-inertial wall mode instabilities in viscoelastic plane Poiseuille flow. *Journal of Fluid Mechanics*, 881:119–163.

[8] Chaudhary, I., Garg, P., Subramanian, G., and Shankar, V. (2020). Linear instability of viscoelastic pipe flow. *ArXiv*.

[9] Cherubini, S., Palma, P. D., Robinet, J. C., and Bottaro, A. (2011). Edge states in a boundary layer. *Phys. Fluids*, 23(5):051705.

[10] Choueiri, G. H., Lopez, J. M., and Hof, B. (2018). Exceeding the Asymptotic Limit of Polymer Drag Reduction. *Phys. Rev. Lett.*, 120(12):124501.

[11] Dallas, V., Vassilicos, J., and Hewitt, G. (2010). Strong polymer-turbulence interactions in viscoelastic turbulent channel flow. *Phys. Rev. E*, 82(6):066303.

[12] De Gennes, P. (1974). Coil-stretch transition of dilute flexible polymers under ultrahigh velocity gradients. *The Journal of Chemical Physics*, 60(12):5030–5042.

[13] de Gennes, P. G. (1979). *Scaling Concepts in Polymer Physics*. Cornell University Press, Ithaca, NY.

[14] Doi, M. and Edwards, S. F. (1986). *The Theory of Polymer Dynamics*. Oxford University Press, New York.

[15] Drazin, P. G. and Reid, W. H. (1981). *Hydrodynamic Stability*. Cambridge Monographs on Mechanics and Applied Mathematics. Cambridge University Press, Cambridge.

[16] Drazin, P. G. and Reid, W. H. (2004). *Hydrodynamic Stability*. Cambridge Mathematical Libraries. Cambridge University Press, second edition.

[17] Dubief, Y., Page, J., Kerswell, R. R., Terrapon, V. E., and Steinberg, V. (2020). A first coherent structure in elasto-inertial turbulence. *arXiv preprint arXiv:2006.06770*.

[18] Dubief, Y., Terrapon, V. E., and Soria, J. (2013). On the mechanism of elasto-inertial turbulence. *Phys. Fluids*, 25(11):110817.

[19] Dubief, Y., Terrapon, V. E., White, C. M., Shaqfeh, E. S. G., Moin, P., and Lele, S. K. (2005). New Answers on the Interaction Between Polymers and Vortices in Turbulent Flows. *Flow Turbulence Combust*, 74(4):311–329.

[20] Duguet, Y., Pringle, C. C. T., and Kerswell, R. R. (2008a). Relative periodic orbits in transitional pipe flow. *Phys. Fluids*, 20(11):114102.

[21] Duguet, Y., Schlatter, P., Henningson, D. S., and Eckhardt, B. (2012). Self-sustained localized structures in a boundary-layer flow. *Phys. Rev. Lett.*, 108.

[22] Duguet, Y., Willis, A. P., and Kerswell, R. R. (2008b). Transition in pipe flow: the saddle structure on the boundary of turbulence. *J. Fluid Mech.*, 613:255–274.

[23] Eckhardt, B., Faisst, H., Schmiegel, A., and Schneider, T. M. (2008). Dynamical systems and the transition to turbulence in linearly stable shear flows. *Philosophical Transactions Of The Royal Society A-Mathematical Physical And Engineering Sciences*, 366(1868):1297–1315.

[24] Eckhardt, B., Schneider, T. M., Hof, B., and Westerweel, J. (2007). Turbulence transition in pipe flow. *Annu Rev Fluid Mech*, 39:447–468.

[25] Eitel-Amor, G., Örlü, R., Schlatter, P., and Flores, O. (2015). Hairpin vortices in turbulent boundary layers. *Phys. Fluids*, 27(2):025108–18.

[26] Escudier, M. P., Nickson, A. K., and Poole, R. J. (2009). Turbulent flow of viscoelastic shear-thinning liquids through a rectangular duct: Quantification of turbulence anisotropy. *Journal of Non-Newton. Fluid Mech.*, 160(1):2–10.

[27] Fink, J. (2015). *Petroleum engineer's guide to oil field chemicals and fluids*. Gulf Professional Publishing.

[28] Forame, P. C., Hansen, R. J., and Little, R. C. (1972). Observations of early turbulence in the pipe flow of drag reducing polymer solutions. *AIChE Journal*, 18(1):213–217.

[29] Garg, P., Chaudhary, I., Khalid, M., Shankar, V., and Subramanian, G. (2018). Viscoelastic pipe flow is linearly unstable. *Phys. Rev. Lett.*, 121(2):024502.

[30] Gibson, J. F. (2012). ChannelFlow: a spectral Navier-Stokes simulator in C++. Technical report, University of New Hampshire.

[31] Gibson, J. F. and Brand, E. (2014). Spanwise-localized solutions of planar shear flows. *J. Fluid Mech.*, 745:25–61.

[32] Gibson, J. F., Halcrow, J., and Cvitanović, P. (2008). Visualizing the geometry of state space in plane Couette flow. *J. Fluid Mech.*, 611:24.

[33] Gibson, J. F., Halcrow, J., and Cvitanovic, P. (2009). Equilibrium and travelling-wave solutions of plane Couette flow. *J. Fluid Mech.*, 638:243–266.

[34] Graham, M. D. (2014). Drag reduction and the dynamics of turbulence in simple and complex fluids. *Phys. Fluids*, 26:101301.

[35] Graham, M. D. (2018a). *Microhydrodynamics, Brownian motion, and complex fluids*, volume 58. Cambridge University Press.

[36] Graham, M. D. (2018b). *Microhydrodynamics, Brownian Motion and Complex Fluids*. Cambridge University Press, Cambridge, to appear edition.

[37] Guckenheimer, J. (2004). Bifurcations of relaxation oscillations. *Normal Forms, Bifurcations and Finiteness Problems in Differential Equations*, 137:295–316.

[38] Hameduddin, I., Gayme, D. F., and Zaki, T. A. (2019). Perturbative expansions of the conformation tensor in viscoelastic flows. *J. Fluid Mech.*, 858:377–406.

[39] Haward, S. J., Page, J., Zaki, T. A., and Shen, A. Q. (2018). Inertioelastic Poiseuille flow over a wavy surface. *Phys. Rev. Fluids*, 3(9):091302.

[40] Herbert, T. (1979). Periodic secondary motions in a plane channel. In *Proceedings of the Fifth International Conference on Numerical Methods in Fluid Dynamics June 28–July 2, 1976 Twente University, Enschede*, pages 235–240. Springer.

[41] Hof, B., van Doorne, C. W., Westerweel, J., Nieuwstadt, F. T., Faisst, H., Eckhardt, B., Wedin, H., Kerswell, R. R., and Waleffe, F. (2004). Experimental observation of nonlinear traveling waves in turbulent pipe flow. *Science*, 305(5690):1594–1598.

[42] Hou, Y. X., Somandepalli, V. S. R., and Mungal, M. G. (2008). Streamwise development of turbulent boundary-layer drag reduction with polymer injection. *J. Fluid Mech.*, 597:31–66.

[43] Hoyt, J. W. (1977). Laminar-turbulent transition in polymer solutions. *Nature*, 270:508–509.

[44] Itano, T. and Generalis, S. (2009). Hairpin Vortex Solution in Planar Couette Flow: A Tapestry of Knotted Vortices. *Phys. Rev. Lett.*, 102(11).

[45] Jiménez, J. (1990). Transition to turbulence in two-dimensional Poiseuille flow. *J. Fluid Mech.*, 218:265–297.

[46] Jiménez, J. (2013). Near-wall turbulence. *Physics of Fluids*, 25(10):101302.

[47] Jiménez, J. (2018). Coherent structures in wall-bounded turbulence. *Journal of Fluid Mechanics*, 842.

[48] Jiménez, J. and Moin, P. (1991). The minimal flow unit in near-wall turbulence. *Journal of Fluid Mechanics*, 225:213–240.

[49] Kawahara, G., Uhlmann, M., and van Veen, L. (2012). The Significance of Simple Invariant Solutions in Turbulent Flows. *Annu Rev Fluid Mech*, 44:203–225.

[50] Khapko, T., Kreilos, T., Schlatter, P., Duguet, Y., Eckhardt, B., and Henningson, D. S. (2013). Localized edge states in the asymptotic suction boundary layer. *J. Fluid Mech.*, 717:R6.

[51] Kim, K., Li, C.-F., Sureshkumar, R., Balachandar, S., and Adrian, R. J. (2007). Effects of polymer stresses on eddy structures in drag-reduced turbulent channel flow. *J. Fluid Mech.*, 584:281–299.

[52] King, G. E. *et al.* (2012). Hydraulic fracturing 101: What every representative, environmentalist, regulator, reporter, investor, university researcher, neighbor and engineer should know about estimating frac risk and improving frac performance in unconventional gas and oil wells. In *SPE hydraulic fracturing technology conference*. Society of Petroleum Engineers.

[53] Kurganov, A. and Tadmor, E. (2000). New high-resolution central schemes for nonlinear conservation laws and convection–diffusion equations. *J. Comput. Phys.*, 160(1):241–282.

[54] Larson, R. G. (1999). *The Structure and Rheology of Complex Fluids*. Oxford University Press, New York.

[55] Lee, S. J. and Zaki, T. A. (2017). Simulations of natural transition in viscoelastic channel flow. *J. Fluid Mech.*, 820:232–262.

[56] Li, C. F., Gupta, V. K., Sureshkumar, R., and Khomami, B. (2006a). Turbulent channel flow of dilute polymeric solutions: Drag reduction scaling and an eddy viscosity model. *Journal of Non-Newton. Fluid Mech.*, 139(3):177–189.

[57] Li, W. and Graham, M. D. (2007). Polymer induced drag reduction in exact coherent structures of plane Poiseuille flow. *Phys. Fluids*, 19(8):083101.

[58] Li, W., Stone, P. A., and Graham, M. D. (2005). Viscoelastic nonlinear traveling waves and drag reduction in plane Poiseuille flow. *Fluid Mechanics and its Applications: Proceedings of the IUTAM Symposium on Laminar-Turbulent Transition and Finite Amplitute Solutions*, 77:285–308.

[59] Li, W., Xi, L., and Graham, M. D. (2006b). Nonlinear travelling waves as a framework for understanding turbulent drag reduction. *J. Fluid Mech.*, 565:353–362.

[60] Lopez, J. M., Choueiri, G. H., and Hof, B. (2019). Dynamics of viscoelastic pipe flow at low reynolds numbers in the maximum drag reduction limit. *Journal of Fluid Mechanics*, 874:699–719.

[61] Markeviciute, V. and Kerswell, R. (2020). Degeneracy of turbulent states in 2d channel flow. *Bulletin of the American Physical Society*.

[62] McKeon, B. J. and Sharma, A. S. (2010a). A critical-layer framework for turbulent pipe flow. *J. Fluid Mech.*, 658:336–382.

[63] McKeon, B. J. and Sharma, A. S. (2010b). A critical-layer framework for turbulent pipe flow. *J. Fluid Mech.*, 658:336–382.

[64] Mellibovsky, F. and Meseguer, A. (2015). A mechanism for streamwise localisation of nonlinear waves in shear flows. *J. Fluid Mech.*, 779:R1.

[65] Min, T., Choi, H., and Yoo, J. Y. (2003). Maximum drag reduction in a turbulent channel flow by polymer additives. *J. Fluid Mech.*, 492:91–100.

[66] Nagata, M. and Deguchi, K. (2013). Mirror-symmetric exact coherent states in plane Poiseuille flow. *J. Fluid Mech.*, 735:R4.

[67] Neelavara, S. A., Duguet, Y., and Lusseyran, F. (2017). State space analysis of minimal channel flow. *Fluid Dynamics Research*, 49(3):035511–16.

[68] Öttinger, H. C. (1996). *Stochastic Processes in Polymeric Fluids*. Springer, Berlin.

[69] Page, J. and Zaki, T. A. (2015). The dynamics of spanwise vorticity perturbations in homogeneous viscoelastic shear flow. *J. Fluid Mech.*, 777:327–363.

[70] Park, J. S. and Graham, M. D. (2015). Exact coherent states and connections to turbulent dynamics in minimal channel flow. *J. Fluid Mech.*, 782:430–454.

[71] Patera, A. T. and Orszag, S. A. (1981). Finite-amplitude stability of axisymmetric pipe flow. *J. Fluid Mech.*, 112:467–474.

[72] Pereira, A., Thompson, R. L., and Mompean, G. (2019a). Beyond the maximum drag reduction asymptote: the pseudo-laminar state. *arXiv preprint arXiv:1911.00439*.

[73] Pereira, A. S., Thompson, R. L., and Mompean, G. (2019b). Common features between the newtonian laminar–turbulent transition and the viscoelastic drag-reducing turbulence. *Journal of Fluid Mechanics*, 877:405–428.

[74] Perry, A. E. and Chong, M. S. (1982). On the mechanism of wall turbulence. *J. Fluid Mech.*, 119(173):106–121.

[75] Ptasinski, P., Nieuwstadt, F., van den Brule, B., and Hulsen, M. (2001). Experiments in turbulent pipe flow with polymer additives at maximum drag reduction. *Flow Turbul Combust*, 66(2):159–182.

[76] Ptasinski, P. K., Boersma, B. J., Nieuwstadt, F. T. M., Hulsen, M. A., van den Brule, B. H. A. A., and Hunt, J. C. R. (2003). Turbulent channel flow near maximum drag reduction: simulations, experiments and mechanisms. *J. Fluid Mech.*, 490:251–291.

[77] Rawat, S., Cossu, C., and Rincon, F. (2016). Travelling-wave solutions bifurcating from relative periodic orbits in plane Poiseuille flow. *Comptes Rendus Mécanique*, 344(6):448–455.

[78] Robinson, S. K. (1991). Coherent Motions in the Turbulent Boundary-Layer. *Annu Rev Fluid Mech*, 23(1):601–639.

[79] Rubinstein, M. and Colby, R. H. (2003). *Polymer Physics*. Oxford University Press, Oxford.

[80] Samanta, D., Dubief, Y., Holzner, M., Schäfer, C., Morozov, A. N., Wagner, C., and Hof, B. (2013). Elasto-inertial turbulence. *Proc. Nat. Acad. Sci.*, 110(26):10557–10562.

[81] Schlatter, P., Li, Q., Örlü, R., Hussain, F., and Henningson, D. S. (2014). On the near-wall vortical structures at moderate reynolds numbers. *European Journal of Mechanics-B/Fluids*, 48:75–93.

[82] Schmid, P. J. (2007). Nonmodal stability theory. *Annu. Rev. Fluid Mech.*, 39:129–162.

[83] Shekar, A. and Graham, M. D. (2018). Exact coherent states with hairpin-like vortex structure in channel flow. *J. Fluid Mech.*, 849:76–89.

[84] Shekar, A., McMullen, R. M., McKeon, B. J., and Graham, M. D. (2020). Self-sustained elastoinertial tollmien–schlichting waves. *Journal of Fluid Mechanics*, 897:A3.

[85] Shekar, A., McMullen, R. M., Wang, S.-N., McKeon, B. J., and Graham, M. D. (2019). Critical-Layer Structures and Mechanisms in Elastoinertial Turbulence. *Phys. Rev. Lett.*, 122(12):124503.

[86] Sid, S., Terrapon, V. E., and Dubief, Y. (2018). Two-dimensional dynamics of elasto-inertial turbulence and its role in polymer drag reduction. *Phys. Rev. Fluids*, 3(1):011301.

[87] Skufca, J. D., Yorke, J. A., and Eckhardt, B. (2006). Edge of chaos in a parallel shear flow. *Phys. Rev. Lett.*, 96(17):174101.

[88] Smits, A. J., McKeon, B. J., and Marusic, I. (2011). High–Reynolds Number Wall Turbulence. *Annu Rev Fluid Mech*, 43(1):353–375.

[89] Srinivas, S. and Kumaran, V. (2017). Effect of viscoelasticity on the soft-wall transition and turbulence in a microchannel. *Journal of Fluid Mechanics*, 812:1076.

[90] Stone, P. and Graham, M. D. (2003). Polymer dynamics in a model of the turbulent buffer layer. *Phys. Fluids*, 15(5):1247–1256.

[91] Stone, P., Waleffe, F., and Graham, M. D. (2002). Toward a structural understanding of turbulent drag reduction: Nonlinear coherent states in viscoelastic shear flows. *Phys. Rev. Lett.*, 89(20):208301.

[92] Stone, P. A., Roy, A., Larson, R. G., Waleffe, F., and Graham, M. D. (2004). Polymer drag reduction in exact coherent structures of plane shear flow. *Phys. Fluids*, 16(9):3470–3482.

[93] Strobl, G. (1996). *The Physics of Polymers*. Springer, Berlin.

[94] Tamano, S., Graham, M. D., and Morinishi, Y. (2011). Streamwise variations in turbulence statistics in drag-reducing turbulent boundary layer of viscoelastic fluids. *Proceedings of ASME-JSME-KSME Joint Fluids Engineering Conference 2011*.

[95] Theodorsen, T. (1952). Mechanism of Turbulence. In *Second International Midwest Conference on Fluid Mechanics*, pages 1–19, Columbus. Ohio State University.

[96] Toh, S. and Itano, T. (2003). A periodic-like solution in channel flow. *J. Fluid Mech.*, 481:67–76.

[97] Toms, B. (1949). Proceedings of the 1st international congress on rheology. *Vol. II, North Holland, Amsterdam*, page 135.

[98] Toms, B. (1977). On the early experiments on drag reduction by polymers. *The Physics of Fluids*, 20(10):S3–S5.

[99] Townsend, A. A. (1961). Equilibrium layers and wall turbulence. *J. Fluid Mech.*, 11(1):97–120.

[100] Vaithianathan, T., Robert, A., Brasseur, J. G., and Collins, L. R. (2006). An improved algorithm for simulating three-dimensional, viscoelastic turbulence. *J. Non-Newtonian Fluid Mech.*, 140(1-3):3–22.

[101] Virk, P. S., Mickley, H. S., and Smith, K. A. (1970). The ultimate asymptote and mean flow structure in Toms' phenomenon. *J. Appl. Mech.*, 37(2):488–493.

[102] Waleffe, F. (1997). On a self-sustaining process in shear flows. *Phys. Fluids*, 9(4):883–900.

[103] Waleffe, F. (1998). Three-dimensional coherent states in plane shear flows. *Phys. Rev. Lett.*, 81(19):4140–4143.

[104] Waleffe, F. (2001). Exact coherent structures in channel flow. *J. Fluid Mech.*, 435:93–102.

[105] Waleffe, F. (2003). Homotopy of exact coherent structures in plane shear flows. *Phys. Fluids*, 15(6):1517–1534.

[106] Wall, D. P. and Nagata, M. (2016). Exact coherent states in channel flow. *J. Fluid Mech.*, 788:444–468.

[107] Wang, J., Gibson, J., and Waleffe, F. (2007). Lower branch coherent states in shear flows: Transition and control. *Phys. Rev. Lett.*, 98(20):204501.

[108] Wang, S.-N. (2017). *Nonlinear Dynamics of Viscoelastic Turbulence in Transitional Channel Flow*. The University of Wisconsin-Madison.

[109] Wang, S.-N., Graham, M. D., Hahn, F. J., and Xi, L. (2014a). Time-series and extended karhunen–loève analysis of turbulent drag reduction in polymer solutions. *AIChE Journal*, 60(4):1460–1475.

[110] Wang, S.-N., Graham, M. D., Hahn, F. J., and Xi, L. (2014b). Time-series and extended Karhunen-Loève analysis of turbulent drag reduction in polymer solutions. *AIChE Journal*, 60(4):1460–1475.

[111] Warholic, M., Massah, H., and Hanratty, T. (1999). Influence of drag-reducing polymers on turbulence: effects of Reynolds number, concentration and mixing. 27(5):461–472.

[112] Wedin, H. and Kerswell, R. R. (2004). Exact coherent structures in pipe flow: travelling wave solutions. *J. Fluid Mech.*, 508:333–371.

[113] White, C. M. and Mungal, M. G. (2008). Mechanics and prediction of turbulent drag reduction with polymer additives. *Annu Rev Fluid Mech*, 40:235–256.

[114] Woodcock, J. D. and Marusic, I. (2015). The statistical behaviour of attached eddies. *Phys. Fluids*, 27(1):015104–25.

[115] Wu, X. and Moin, P. (2009). Direct numerical simulation of turbulence in a nominally zero-pressure-gradient flat-plate boundary layer. *J. Fluid Mech.*, 630:5–41.

[116] Xi, L. (2019). Turbulent drag reduction by polymer additives: Fundamentals and recent advances. *Physics of Fluids*, 31(12):121302.

[117] Zakin, J. L., Ni, C. C., Hansen, R. J., and Reischman, M. M. (1977). Laser Doppler velocimetry studies of early turbulence. *Phys. Fluids*, 20(10):S85.

[118] Zammert, S. and Eckhardt, B. (2014). Streamwise and doubly-localised periodic orbits in plane Poiseuille flow. *J. Fluid Mech.*, 761:348–359.

[119] Zammert, S. and Eckhardt, B. (2016). Harbingers and latecomers – the order of appearance of exact coherent structures in plane Poiseuille flow. *J Turbul*, 18(2):103–114.

[120] Zhang, M., Lashgari, I., Zaki, T. A., and Brandt, L. (2013). Linear stability analysis of channel flow of viscoelastic Oldroyd-B and FENE-P fluids. *J. Fluid Mech.*, 737:249–279.

[121] Zhu, L., Xi, L., *et al.* (2021). Nonasymptotic elastoinertial turbulence for asymptotic drag reduction. *Physical Review Fluids*, 6(1):014601.